Electron Correlations and Spin in Asymmetric GaAs Quantum Point Contacts and Signatures of Structural Transitions in Hall Effect of FeSe

by

Phillip M Wu

Department of Physics
Duke University

Date: ____________________

Approved:

____
Albert Chang, Advisor

____
Harold Baranger

____
Haiyan Gao

____
Stefan Bass

____
Gleb Finkelstein

Dissertation submitted in partial fulfillment of the requirements for the degree of
Doctor of Philosophy in the Department of Physics
in the Graduate School of Duke University
2010

ABSTRACT

(Condensed Matter)

Electron Correlations and Spin in Asymmetric GaAs Quantum Point Contacts and Signatures of Structural Transitions in Hall Effect of FeSe

by

Phillip M Wu

Department of Physics
Duke University

Date: ______________________

Approved:

____
Albert Chang, Advisor

____
Harold Baranger

____
Haiyan Gao

____
Stefan Bass

____
Gleb Finkelstein

An abstract of a dissertation submitted in partial fulfillment of the requirements for
the degree of Doctor of Philosophy in the Department of Physics
in the Graduate School of Duke University
2010

Abstract

The 1D Wigner crystal is a long sought after strongly correlated quantum state. Here we present electronic transport data of asymmetric quantum point contacts (QPC) tuned to the spin-incoherent regime, which provides evidence for achieving the 1D Wigner state. Our result can be distinguished in several particularly noticeable ways. First, we utilize an asymmetric point contact geometry that is simple to fabricate and has not been studied previously. We are able to tune to the conductance anomalies simply by asymmetrically applying voltages to the gates. Second, we observe clear suppression of the first plateau and direct jumps to the second in these asymmetric QPCs at liquid helium temperatures (4.2 K). Such conductance behavior is indicative of Wigner crystal row formation.

This thesis suggests that the asymmetric geometry and gating scheme allows for a novel way to search for strongly correlated electronic behavior in quasi-1D quantum wires. A key finding is the importance of asymmetric QPCs for observation of anomalous transport characteristics. We have observed a strongly developed e^2/h feature under asymmetric voltage gating and zero applied magnetic field. Such a feature is attributed to enhanced spin energies in the system. We believe the asymmetric design allows for a relaxing of the 1D confinement so that a quasi-1D electron conformation develops, which in turn allows for various possible magnetic states. In addition, by optimally tuning the confinement potential, we observe an unexpected suppression of the $2e^2/h$ plateau. This provides further evidence for unusual electron

arrangements in the asymmetric quantum point contact.

I also discuss transport studies on the new FeSe superconductor. Our collaboration discovered the superconducting β-FeSe compound [46] with a Tc approximately 8 K. The crystal lattice structure of β-FeSe is by far the simplest of the Fe superconductors. One of the most interesting observations regarding FeSe is that the crystal structure undergoes a structural transition at ~ 105 K from tetragonal to orthorhombic (or triclinic) symmetry. We believe this structural transition to be closely related to the origin of superconductivity in this class of materials.

Transport studies also seem to support this claim. From Hall effect measurements of bulk FeSe, we find that FeSe is likely a two band (electron and hole) superconductor, which suggests it is quite different from the cuprates, and that very unconventional superconducting mechanisms are at play. The temperature dependence of the Hall coefficient is measured, and found to rapidly increase below 105 K. This suggests the scattering time related to hole bands dominate the transport at low temperature. As there is no magnetic ordering observed at low temperature, we do not expect the scattering from random Fe magnetic impurities to play a significant role in the enhanced hole scattering times. Thus, we speculate that this change is related to the structural transition observed.

To my loving and supportive family: Mom, Dad, Al and Debby

Contents

List of Tables

List of Figures

List of Abbreviations and Symbols

Symbols

m	Effective mass
g_s	Spin degeneracy
g_v	Valley degeneracy
ϵ	Dielectric constant
$\rho(E)$	Density of states
n_s	Sheet density
k_F	Fermi wave vector
v_F	Fermi velocity
E_F	Fermi energy
μ_e	Mobility
τ	Scattering time
D	diffusion constant
ρ	Resistivity
λ_F	Fermi wavelength
l_{mfp}	Mean free path
l_ϕ	Phase coherence length
l_T	Thermal length
l_{cyc}	Cyclotron radius
l_m	Magnetic length

ω_c	Cyclotron frequency

Abbreviations

2DES(or 2DEG)	Two dimensional electron systems (gas).
PMMA	Poly(methyl methacrylate)
ebeam	Electron beam
MIBK:IPA	Methyl isobutyl ketone: isopropanol
SEM	Scanning electron microscope
SNS	Superconducting-Normal-Superconducting
SET	Single electron transistor
MBE	Molecular Beam Epitaxy

Acknowledgements

First and foremost, I would like to thank my advisor, Prof. Albert Chang, for giving me the opportunity to study with him. The last few years have been an extremely rewarding experience. I appreciate the deep insight Prof. Chang has for many physics problems, which he often shares quite freely. I also appreciate the considerable time he has spent working and teaching me the art of low temperature cryogenics and low noise measurements. He has also shown me the importance of quick back of the envelope estimates to obtain a better grasp of what the data means. I greatly appreciate how after some initial discussions, Prof. Chang always takes a step back and gives me the freedom to explore on my own. This has allowed me to explore and develop my own interests and abilities. I have gained confidence and independence under his guidance, and feel prepared for the road ahead in academia.

I would also like to thank my thesis committee members for their support and guidance. I want to thank Prof. Baranger for teaching the Advanced Solid State course, which certainly helped to strengthen my fundamentals in condensed matter. I also appreciate his spending time to talk to me about much of my work, and offering valuable comments and feedback. I want to thank Prof. Bass for a good course in Statistical mechanics. I want to thank Prof. Finkelstein for his generosity in lending experimental equipment and for also taking the time to give me advice and comments. I also benefitted greatly from Prof. Gao's course on Nuclear and Particle Physics, where I learned much about energy production in stars. I also want to thank her for providing encouragement and guidance over the years.

I want to thank Peng Li for the last few years. Together we have learned a lot and obtained our Ph.D.s!! I wish Peng, Zheng, and Will great future success.

I have enjoyed interactions with our current and former group members: Limin Cao, Zaili Fang, Fabio Altomare, Angelo Bove, Nathan Kundtz, and Linjun Wang. The members of the Finkelstein group have also been great to work and discuss with: Matthew Prior, Alex Makarovski, Sungha Park, Ulas Coskun, Ivan Borzenets, and Henok Mebrahtu. I particularly wish to thank Yuriy Bomze, for sharing many of his great ideas! I have also had the pleasure to discuss problems with members of the Baranger group: Ribhu Kaul, Devrim Guclu, Jose Hoyos Neto, Eduardo Novais, Abhijit Mehta, and Dong Liu. I also want to thank my many friends in the department, particularly members of my first year crew: James Joseph, Arya Roy, Xing Xong, Qian Xin, Ken McKenzie, Annerose Helmer, Friedemann Quiesser, and Erik Plauschinn, and officemates in French (from Prof. Gao's group) Wei Chen, Min Huang, Georgios Laskaris, and Qiujian Ye.

I am indebted to Richard Nappi for his help and vast expertise in machining, and thank him for the many wonderful conversations. I also want to express my thanks to several Physics department staff who have made me feel right at home these last few years, Peggy and David Hall, Donna Ruger, Donna Elliott, and Florin and Manuela Damian. I also want to thank Prof. Stephen Teitsworth for lending me his dewar to fit our triaxial magnet.

I want to particularly thank Prof. Horst Meyer, whose office is down the hall from our Physics laboratory. Prof. Meyer is always cheerful and full of life, and certainly an inspiration. It is my hope that I will be able to, just as Horst does everyday, enjoy doing what I do for as long as possible. I am also thankful for his introducing me to the chamber arts program at Duke.

Finally, this section would not be complete without acknowledging my brother, Albert Wu, my wife, Debby Chang and my parents, Maw-kuen and Huichin Wu. It is with their enduring love and support that made me who I am today.

Introduction

Advances in nanofabrication techniques over the last two decades have allowed researchers tremendous creativity in designing novel nanometer sized devices. Reducing the device size to the nanometer scale is interesting and important as it allows for the ability to better probe behavior near the quantum limit. These studies could have profound implications for both applications, for example, in quantum computation and spintronics, and in our fundamental understanding of low dimensional electron and spin transport properties.

One of the simplest devices that can be fabricated is a quantum point contact (QPC), which is a nanometer sized constriction separating two larger electronic systems. These constrictions have typically been formed by applying a voltage to a pair of mirror-image metallic gates deposited on top of a high mobility two dimensional electron gas (2DEG). The potential that develops from the applied voltage depletes the underlying 2DEG, in a process similar to gating a field effect transistor. Quite strikingly, as the point contact constriction width is gradually reduced by applying more negative gate voltage equally to the pair of gates, a series of quantized staircase steps results in the measured conductance [110, 104]. This is a clear manifestation of quantum ballistic transport, which occurs only when the device dimensions are shorter than the mean length between electron scattering events.

The observation of the quantized conductance is a striking example of how properly designed device structure can give rise to unusual transport behavior. This thesis seeks to exploit the available fabrication tools and techniques to further play with this theme. In contrast to typical QPC design, I will deliberately introduce asymmetries into the device pattern. These asymmetric QPCs are found to display very different transport behavior from the symmetric ones. In particular, conductance traces where the first quantization plateau is greatly suppressed have been observed.

We suggest that the observed transport behavior can be attributed to a long sought after one-dimensional (1D) quantum state, the 1D Wigner crystal [90, 74]. The 1D Wigner crystal only occurs in a precise low density regime. The asymmetric gating of the QPC makes it possible to sweep through to the proper density for Wigner crystal behavior. Coulomb interactions greatly exceed the electron kinetic energy in this density regime, and the localization of electrons exponentially suppresses spin exchange processes. This regime is also termed the spin-incoherent Luttinger liquid.

In a change of topic, I also discuss transport studies on the new Fe-based superconductor, β-FeSe. The layered FeAs based superconductors, the first of which was discovered by Hosono in 2008 [52], have superconducting transition temperature Tc as high as 55 K [125], making them the only non-cuprate high temperature superconductors known to date. Our collaboration discovered the superconducting β-FeSe compound with a Tc approximately 8 K [46]. The crystal lattice structure of β-FeSe is by far the simplest of the Fe superconductors, as it consists of only Fe and Se arranged in a layered tetrahedral conformation. This simple structure in principle would allow researchers to most easily discern the crucial mechanisms giving rise to superconductivity. Selenium also has much less stringent safety requirements in the laboratory compared to the highly toxic As.

One of the most interesting observations regarding FeSe is that the crystal structure undergoes a structural transition at ~ 105 K from tetragonal to orthorhombic (or triclinic) symmetry. We believe this structural transition to be closely related to the origin of superconductivity in this class of materials.

Transport studies also seem to support this claim. From Hall effect measurements of bulk FeSe, we find that FeSe is likely a two band (electron and hole) superconductor, which suggests it is quite different from the cuprates, and that very unconventional superconducting mechanisms are at play. At high temperature, the Hall coefficient is positive (hole). At around 100 K, the coefficient dips negative, indicative of electrons as the major carriers. However, at lower temperatures, the Hall coefficient rapidly turns positive again. This suggests the scattering time related to hole bands dominate the transport at low temperature. As there is no magnetic ordering observed at low temperature, we do not expect the scattering from random Fe magnetic impurities to play a significant role in the enhanced hole scattering times. Thus, we speculate that this change is related to the structural transition observed.

The organization of this thesis is as follows: Chapter 1 briefly reviews the current understanding of transport properties of quantum point contacts from the noninteracting electron picture. A brief discussion of how device shape may affect the conductance is also included. Chapter 2 introduces the Tomonaga-Luttinger liquid, which describes interacting electrons in 1D channels. We will then see how the 1D Wigner crystal is related to the spin-incoherent Luttinger liquid picture, and the theoretical predictions for suppressed transport of a Wigner crystal state. These two chapters present the framework for the studies presented in this thesis.

Chapter 3 details the experimental device parameters and fabrication techniques. The low-temperature measurement setup will also be discussed. Chapter 4 takes a more in depth view of how the asymmetric QPC design can give rise to novel transport behavior. Measurements that led us to optimizing the geometry to observe the spin-incoherent transport are presented.

Chapter 5 presents the experimental data. The measured results show the asymmetric QPC geometry to be a wonderful test system for observing novel transport behavior. In particular, traces with signatures of the 1D Wigner crystal and spin-incoherent transport are shown.

In a change of subject, I include in Chapter 6 Hall Effect measurements done on β-FeSe superconductors. The anomalous Hall behavior observed could be a signature of structural transitions in the system. Finally, Chapter 7 concludes this thesis and briefly explores the interesting possibilities for future research.

1

Quantum Point Contacts

1.1 Quantized Conductance

The electronic transport properties through ultrasmall structures has been of increased interest in recent years. Semiconductor nanostructures are of particular interest due to the availability of clean, low density and high electron mobility systems, such as those formed in the two dimensional electron gas (2DEG) at the AlGaAs-GaAs heterojunction. These 2DEGs have several desirable features compared to other systems, such as thin metal films. First, the low densities achievable mean that the Fermi wavelengths, λ_F are relatively large, typically on the order of 40-60 nm. Second, the large screening lengths allow for the density to be readily varied by electric fields. Finally, these structures can be designed to have high mobilities and large electron mean free paths, l_{mfp}, often exceeding several microns. These features imply that the 2DEGs can be patterned into interesting structures with length L smaller than the mean free path, but width W comparable to the Fermi wavelength, with commercially available lithography techniques. This in turn allows for the study of unusual quantum ballistic transport mechanisms, see Fig. 1.1, where the geometry

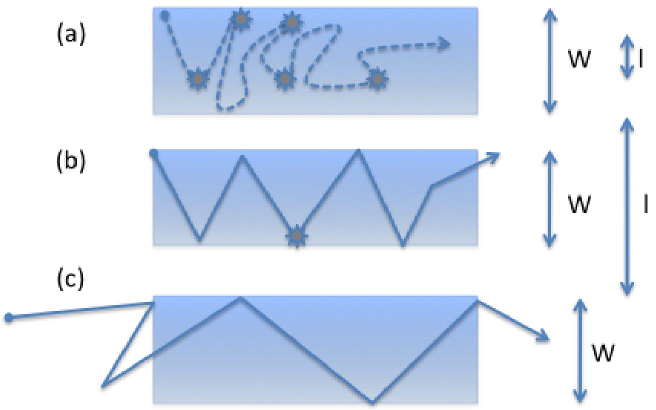

FIGURE 1.1: (a) Diffusive regime where system width W, $L \gg l_{mfp}$ (b) Quasi-ballistic regime where $W \leq l_{mfp} \leq L$ (c) Ballistic transport occurs in systems with W, $L \ll l_{mfp}$. (Figure from [11])

of the structure determines the transport properties.

1.1.1 Initial Discovery

One of the simplest devices that can be created for study is a quantum point contact, as shown in Fig. 1.2. These devices can be tuned so that the its width, W is comparable to $\lambda_F \sim 50$ nm, which make them ideal for probing the ballistic transport regime. The width can be controlled by changing the applied voltage on the metallic gates, in a process similar to that in field effect transistors. Essentially, a negative gate voltage creates a potential that depletes the 2DEG. The conductance through AlGaAs-GaAs split-gate quantum point contacts was found to be quantized in multiples of $2e^2/h$ as a function of gate voltage, as shown in Fig. 1.3 [110, 118]. Here, the negative voltage was applied equally to the two gates, V1 and V2, so that there was no potential drop across the gate electrodes. These studies were made possible by earlier work showing that electrostatic confinement of the 2DEG did not dramatically degrade electron mobilities [124, 104]. It has been harder to observe quantization in ballistic metal point contacts as the $\lambda_F \sim 0.5$ nm in metals is quite

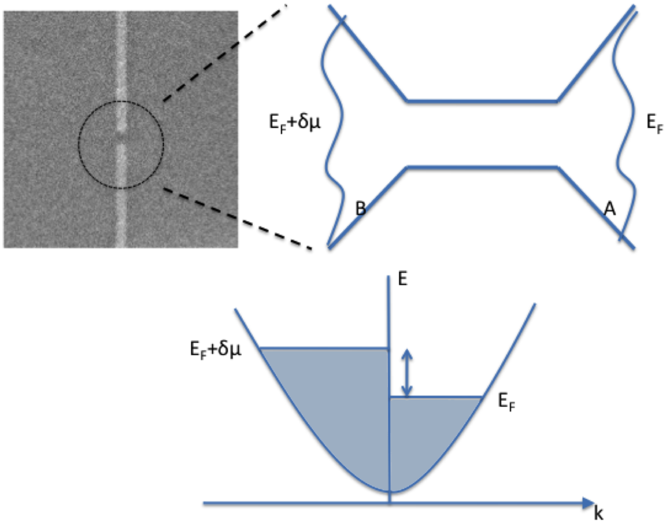

FIGURE 1.2: Micrograph of a quantum point contact which forms a small channel 150 nm wide connecting two large electron reservoirs (top). Schematic of dispersion relation in the narrow channel (bottom). Reservoir A and B differ by the chemical potential, $\delta\mu$. Right moving states are filled to E_F, while left moving states are filled to $E_F + \delta\mu$.

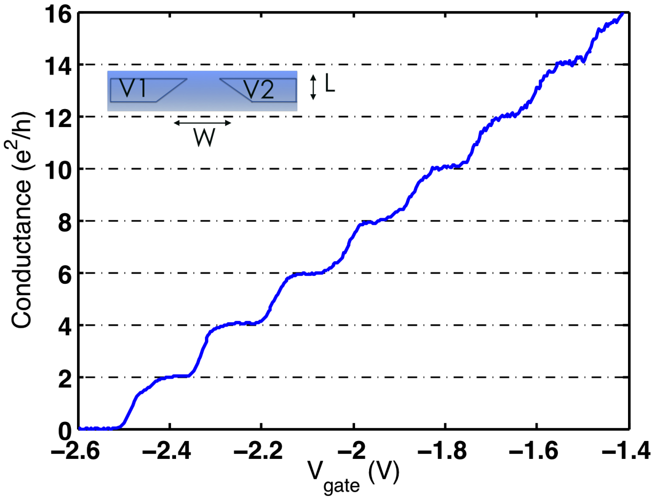

FIGURE 1.3: Quantized conductance plateaus as a function of gate voltage. Measurement was taken in our He3 refrigerator with base temperature 300 mK. The upper inset shows the original device geometry of [110, 118].

small, however there are reports of signatures of conductance quantization in metallic break-junctions and pulled nano-contacts [91, 92, 83, 59].

A simple empirical explanation for the observed result is that since the number N of subbands is an integer, the conductance goes as

$$G = \frac{2e^2}{h} N. \tag{1.1}$$

Applying more negative gate voltage effectively reduced the width and density in the point contact, and thus led to stepwise depopulation of the subband. To fully understand the behavior, we need to develop a proper description of the conductance in terms of the Fermi level properties of the system.

1.1.2 Theory

Let us recall that in an unbounded 2DEG, the energy of conduction electrons in a single subband relative to the band bottom is a function of the momentum, $\hbar k$, given by

$$E(k) = \hbar^2 k^2 / 2m, \tag{1.2}$$

where $m = m^* m_e$ is the effective mass. For GaAs, $m^* = 0.067$. The number of electronic states, $n(E)$ is found by considering the number of distinct states $g_s g_v A/(2\pi)^2$ in a circle in k-space of area $A = 2m\pi E/\hbar^2$. Here $g_s = 2$, $g_v = 1$ are the spin and valley degeneracies, respectively. This results is $n(E) = g_s g_v m E / 2\pi\hbar^2$. Thus, the density of states, $\rho(E) = dn(E)/dE$, of a 2DEG is given by

$$\rho(E) = g_s g_v m / 2\pi\hbar^2, \tag{1.3}$$

which surprisingly is independent of energy! This is quite different from the 3D result, where the density of states has $\sqrt{E}$ dependence. A sequence of subbands is

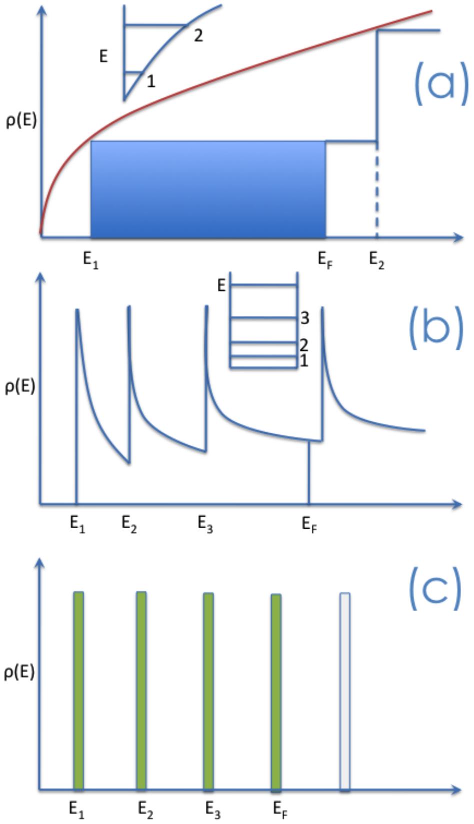

FIGURE 1.4: Energy density of states. (a) 3D (red curve) and 2D (blue) density of states with triangular well potential. (b) Quasi-1D density of states, considering a square well potential. (c) 0D subbands or Landau levels. Broadening of the levels leads to nonzero density of states between peaks.

associated with the finite energy levels in a quantum well, as shown in Fig. 1.4. Higher level subbands only begin to fill after the E_F exceeds the level band bottom.

Forming a quantum point contact further reduces the dimensions by constricting the width. The lateral confinement splits the 2D subbands into a series of 1D subbands, with band bottoms at E_n, where $n = 1, 2, ...$ Thus the total energy of an electron in the nth 1D subband is

$$E_n(k) = E_n + \hbar^2 k^2/2m. \tag{1.4}$$

The confinement levels, E_n, are determined by which model is used to describe the potential well. Two popular and well known models are the square well, with $E_n = (n\pi\hbar)^2/2mW^2$, or the parabolic potential ($V(x) = \frac{1}{2}m\omega_0^2 x^2$) with $E_n = (n - \frac{1}{2})\hbar\omega_0$. Based on this energy function, the 1D density of states can be calculated and is given by

$$\rho(E) = \sum_n 2g_s g_v \left(2\pi \frac{dE_n(k)}{dk}\right)^{-1} = \sum_n g_s g_v \frac{m}{\pi\hbar^2}\left(\frac{\hbar^2}{2m(E - E_n)}\right)^{1/2}, \tag{1.5}$$

which is now a function of $1/\sqrt{E}$, and the summation is over all n for which $E_n < E$. It is often useful to divide the 1D density of states into two equal parts, $\rho_n^{\pm}(E) = g_s g_v \frac{m}{2\pi\hbar^2}\left(\frac{\hbar^2}{2m(E-E_n)}\right)^{1/2}$, where the plus (minus) denotes the right (left) moving states with $k > 0$ ($k < 0$). The evolution of the energy density of states as dimensions are reduced is clearly shown in Fig. 1.4. As the dimensions are reduced, the available energy states become quantized.

We note here that quantization of the available energy states can also be achieved by applying an external magnetic field perpendicular to the plane of the 2DEG. This problem was dealt by Landau, who introduced the gauge transformation $\vec{A} = (0, Bx, 0)$ for magnetic field $\vec{B} = \nabla \times \vec{A}$ in the perpendicular z-direction. The Hamiltonian is then adjusted to

$$H = \frac{(\vec{p} + e\vec{A})^2}{2m} = \frac{p_x^2}{2m} + \frac{m\omega_c^2}{2}(x - x_0)^2, \tag{1.6}$$

Where $\omega_c = eB/m$ is the cyclotron frequency, and $x_0 = -p_y/eB$. The available energies in Eq. 1.4 have $E_n = (n - 1/2)\hbar\omega_c$, where $n = 1, 2, 3\ldots$ are integers. The quantum number n labels the Landau levels, which each carrying a single state per flux quantum h/e through the sample. The density of states can be approximated by a delta function,

$$\rho(E) = g_s g_v \frac{eB}{h} \sum_{n=1}^{\infty} \delta(E - E_n), \tag{1.7}$$

and resemble 0D states. Here the spin states are degenerate, and can be resolved by Zeeman splitting, $E_Z = g\mu_B B$, where $\mu_B = e\hbar/2m_e$ is the Bohr magneton, $g = -0.44$ is the electron Lande g-factor of GaAs and B the applied magnetic field.

Charge transport mechanisms in a 2DEG take place when the electrons are subjected to either an electric or magnetic field. A current $ej = \sigma E$ arises when an external field is applied. In order to determine the conductivity, we note that electrons in the electric field drift between scattering events with velocity $v_{drift} = -eE\Delta t/m$. The mobility is defined from the time average over all scattering events, $\mu_e = e\tau/m$, with τ the scattering time. Mobile electrons in a 2D sheet then have current density $j = n_s v_{drift}$, n_s is the sheet density, which allows to determine the Drude conductivity,

$$\sigma = e n_s \mu_e = \frac{e^2 n_s \tau}{m} = g_s g_v \frac{e^2}{h} \frac{k_F l_{mfp}}{2}. \tag{1.8}$$

Here we have utilized the relation $n_s = g_s g_v k_F^2/4\pi$, and defined the $l_{mfp} = v_F \tau$. We note that already we see the combination of the quantum unit e^2/h in the conductivity. Equation 1.8 describes contributions from all the conduction electrons, but it is often sufficient to consider only the conductivity of electrons near the Fermi level, as weak electric fields only perturb the Fermi-Dirac distribution of electronic states near E_F. The lower lying energy states are too filled to be affected. The well known Einstein relation is one such description of the conductivity in terms of the density, $\rho(E_F)$ and diffusion constant, $D = \frac{1}{2} v_F l_{mfp}$, evaluated at E_F.

$$\sigma = e^2 \rho(E_F) D. \tag{1.9}$$

This description works well when the system dimensions are larger than l_{mfp}, but becomes inadequate in the ballistic transport regime of most quantum point contacts as the conductivity does not exist as a local quantity. Ballistic transport is better described by the Landauer formula, $G = I/V = (e^2/h)T$, which relates the contact conductance through the channel to the transmission probabilities at the Fermi levels on the two sides.

1.1.3 Landauer-Buttiker Formula

We imagine two wide electron reservoirs, A and B, with slight difference in density δn that are brought into contact through a narrow channel, Fig. 1.2. This slight density difference gives rise to a chemical potential difference $\delta\mu = \delta n/\rho(E_F)$, where $\rho(E_F)$ is the density of states in the reservoir, so that on the two sides, A has energy E_F while B has energy $E_F + \delta\mu$. A diffusion current $J = \tilde{D}\delta n$ with diffusion constant $\tilde{D}$ will flow due to the difference in chemical potential. This current can be related to the conductance as $GV/e = \tilde{D}\delta n$, where the bias voltage $eV = \delta\mu$. This results in

$$G = e^2 \rho(E_F)\tilde{D}, \tag{1.10}$$

which is a generalized form of the Einstein relation, Eq. 1.9 [7]. The diffusion constant is found by considering an ideal channel or waveguide with no reflection as the electron travels from B to A. The total current is then the product of the density of $k < 0$ states moving rightwards, Eq. 1.5, times the group velocity, $v_n = dE_n(k)/\hbar dk$, over an energy interval from E_F to $E_F + \delta\mu$.

$$J_n = \int_{E_F}^{E_F+\delta\mu} g_s g_v \left(\frac{2\pi dk}{dE_n(k)}\right) \frac{dE_n(k)}{\hbar dk} = \frac{g_s g_v}{h}\delta\mu. \tag{1.11}$$

Quite importantly, we notice that the group velocity exactly cancels the density,

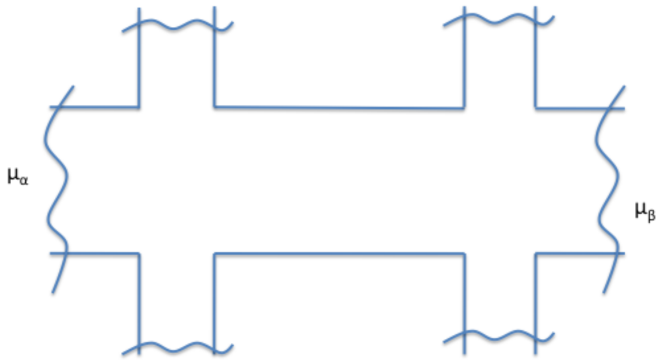

FIGURE 1.5: System with multiple reservoirs, each having chemical potential μ_α or μ_β.

so that J_n is independent of n and E_F. This indicates that the current is shared equally by the N total modes in the channel. If a fraction T_n of the transmitted J_n are reflected due to boundary scattering (not impurity scattering), then we have $J = (g_s g_v/h)\delta\mu \sum_{n=1}^{N} T_n$, which can be modified to

$$G = \frac{2e^2}{h}\sum_{n=1}^{N} T_n, \tag{1.12}$$

where we now apply $g_s = 2$ and $g_v = 1$ for GaAs. The fraction T_n can be expressed in terms of the transmission probability amplitudes from mode n to m, $T_n = \sum_{m=1}^{N} |t_{mn}|^2$. Equation 1.12 is the two terminal Landauer formula. The generalization of the formula to four terminal resistance measurements was done by Buttiker [14]. He considered a system with multiple reservoirs as in Fig. 1.5, α and β, with each reservoir carrying in general a distinct number of propagating modes or leads, N_α and N_β. The transmission from α to β can be described by the probability amplitudes from mode n in α to m in β,

$$T_{\alpha\to\beta} = \sum_{n=1}^{N_\alpha}\sum_{m=1}^{N_\beta} |t_{\beta\alpha,mn}|^2. \tag{1.13}$$

As in the two terminal case, the leads are modeled as ideal, so that reservoir α with chemical potential μ_α above E_F gives rise to current of $(2e/h)N_\alpha\mu_\alpha$ in the lead, a fraction $T_{\alpha\to\beta}/N_\alpha$ which is transmitted to reservoir β, and a fraction $T_{\alpha\to\alpha}/N_\alpha \equiv R_\alpha/N_\alpha$ which is reflected back to reservoir α. The net current in N_α channels is then

$$I_\alpha = \frac{2e}{h}\left((N_\alpha - R_\alpha)\mu_\alpha - \sum_{\beta(\beta\neq\alpha)} T_{\rho\to\alpha}\mu_\beta\right). \tag{1.14}$$

Equation 1.14 can be used to provide a solid theoretical underpinning for a variety of transport measurements in the quantum ballistic regime.

We saw earlier in Eq. 1.11 that the net current is the product of the density of states and the group velocity integrated over the energy spectrum. As the width of the point contact is decreased, the number of subbands is reduced, and as a result the group velocity in each remaining subband increases (think Bernoulli's principle). However, associated with the rise in group velocity is an equal drop in the 1D density of states. *These two effects cancel one another*, so that the current is always composed of equal contributions of $2e^2/h$ from each 1D subband. This equipartition rule arises fundamentally from the cancellation of the density of states with the group velocity in the net current, and is a general result regardless of the confinement potential. It is this amazing behavior that is directly responsible for the observed conductance quantization.

1.1.4 Temperature Dependence

The quantization plateaus are quite robust as long as the temperature is low enough. As the temperature is raised, the plateaus become rounder until they are completely smeared out by the increased thermal energy. This is directly due to the thermal smearing of the Fermi-Dirac distribution. At finite temperatures, we would expect the conductance to be

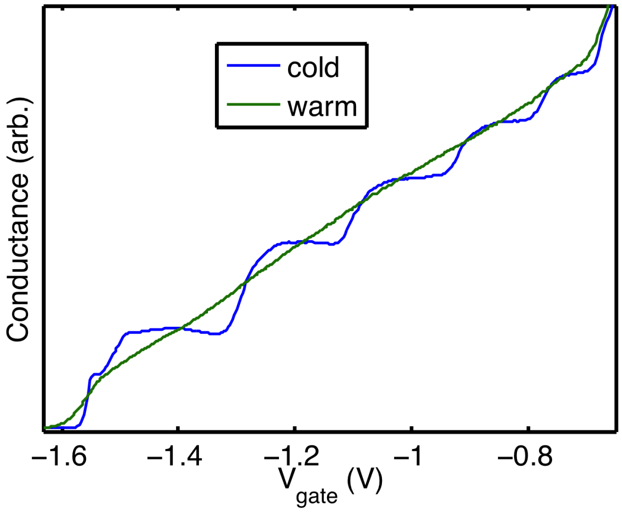

FIGURE 1.6: Conductance traces at low and high temperatures. The cold trace is taken at He3 base temperature, 300 mK. The temperature of the warm trace was not accurately measured, though it is estimated to be around 6-10 K.

$$G(E_F, T) = \int_0^\infty G(E, 0) \frac{df}{dE_F} dE = \frac{2e^2}{h} \sum_{n=1}^{\infty} f(E_n - E_F), \tag{1.15}$$

where we have assumed G to have a step function dependence on E_F at $T = 0$. In typical experiments, the quantized plateaus are completely smeared out around and above 4-6 K, see Fig. 1.6. As the width of df/dE_F is $\sim 4k_BT$, we can roughly estimate the subband splitting to be $\Delta E \sim 2$ meV [10]. A finite DC bias drop across the point contact has a qualitatively similar effect to that of a finite temperature.

1.1.5 Magnetoelectric subbands

We would like to understand the effects of an applied magnetic field on the system. As mentioned earlier, applying a perpendicular magnetic field also gives rise to quantization of the density of states, which leads to the well known Integer (and Fractional) Quantum Hall Effects (I- or F-QHE) [112, 105, 65]. In the IQHE, an increase in a single flux quantum h/e results in a net transfer of N electrons so that

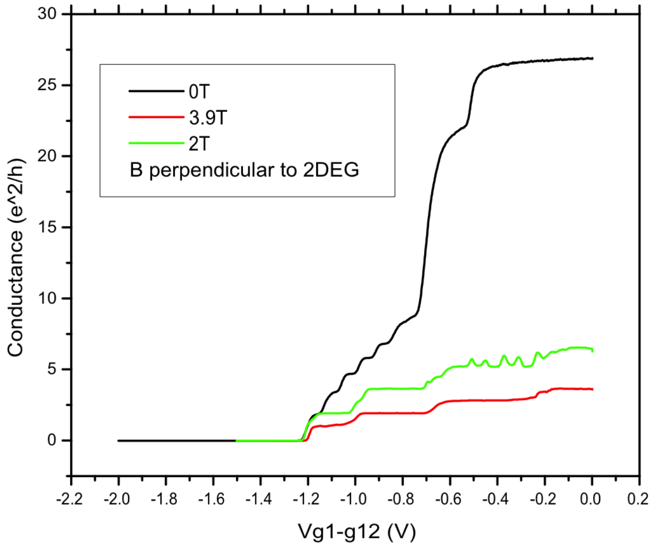

Figure 1.7: Dependence of conductance on magnetic field perpendicular to 2DEG plane.

the conductance also follows Eq. 1.1, but with N now denoting the number of Landau levels. This equivalence implies that the quantum point contact should preserve conductance quantization and undergoes a smooth transition from zero field electrostatic confinement quantization to QHE as a magnetic field is applied. As seen in Fig. 1.7, this is indeed the experimental observation. The number of plateaus is reduced as a larger field is applied, and counting the number of plateaus allows for an estimate of the depopulation of magnetoelectric subbands [12, 108, 110, 117].

Such a measurement allows for a way to determine the width of the 1D channel and corresponding subband energy at that width. We recall the subband energy Eq. 1.4 and Hamiltonian Eq. 1.6, with $E_n = (n - \frac{1}{2})\hbar\omega_c$. The number of Landau levels below energy E is counted by truncating to integers the following,

$$N = \mathrm{Int}\left[1/2 + E/\hbar\omega_c\right]. \tag{1.16}$$

For a narrow 1D channel with magnetic field, we consider first the easier to solve

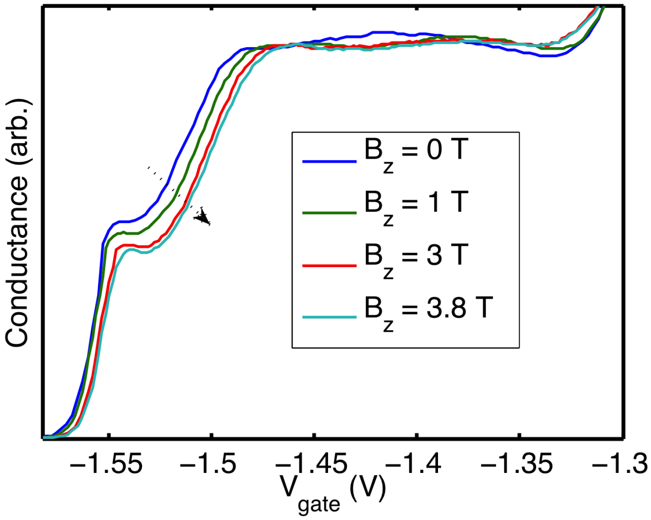

Figure 1.8: Dependence of conductance on magnetic field parallel to 2DEG plane. Traces were taken at 300 mK. Unfortunately, the maximum z-field in our He3 system is 3.8 T. When the spins are completely spin polarized at high fields, a fully developed e^2/h plateau results. The kink at zero field observed is due to interaction effects, which will be discussed in Ch. 2.

parabolic confinement potential $V(x) = \frac{1}{2}m\omega_0^2 x^2$, which is added to Eq. 1.6,

$$H = \frac{p_x^2}{2m} + \frac{m\omega^2}{2}(x - \bar{x}_0)^2 + \frac{\hbar^2 k^2}{2M}. \tag{1.17}$$

Here $\omega = \sqrt{\omega_c^2 + \omega_0^2}$, $\bar{x}_0 = x_0\omega_c/\omega$, and $M = m\omega^2/\omega_0^2$. In this case, Eq. 1.4 for the energy and Eq. 1.16 for the number of subbands are modified by replacing $m \to M$ and $\omega_c \to \omega$. To determine the width of the 1D channel, we define for a parabolic potential the width as $W_{para} \equiv 2\hbar k_F/m\omega_0$ at the Fermi energy. This modifies Eq. 1.16 to

$$N = \mathrm{Int}\left[\frac{1}{2} + \frac{1}{4}k_F W_{para}\sqrt{1 + (W_{para}/2l_{cyc})^2}\right]. \tag{1.18}$$

The number of subbands is determined by a competition between the width due to parabolic confinement and localization length from cyclotron motion, which has cyclotron radius $l_{cyc} = \hbar k_F / eB$. As a comparison, we show the result for a square well confinement potential with width W_{sq} below[110].

$$N \approx \begin{cases} \mathrm{Int}\left[\frac{2}{\pi}\frac{E_F}{\hbar\omega_c}(\arcsin\frac{W_{sq}}{2l_{cyc}} + \frac{W}{2l_{cyc}}\sqrt{1-(\frac{W}{2l_{cyc}})^2})\right] & \text{if } l_{cyc} > \frac{W}{2}, \\ \mathrm{Int}\left[\frac{1}{2} + \frac{E_F}{\hbar\omega_c}\right] & \text{if } l_{cyc} < \frac{W}{2}. \end{cases} \qquad (1.19)$$

The above Eqs. 1.18 and 1.19 spell out a simple procedure for determining W and confinement barrier height E_c, if we assume that E_F does not vary much in a B field, and replace E_F by $E_F - E_c$. For both parabolic and square well, at strong fields, $N \approx (E_F - E_c)/\hbar\omega_c$ is just the number of Landau levels. Counting the number of plateaus allows for the determination of E_c. Then, we utilize the zero field trace to estimate the width, for example, $N \approx (2m(E_F - E_c)/h^2)^{-1/2} W/\pi$ for the square well case. Weisz and Berggren have shown that there is little difference in estimates of the energy and density between the parabolic and square well case [117]. However, the parabolic potential provides a better estimate of the width when the constriction is extremely narrow.

Applying a magnetic field also introduces a Zeeman energy, E_Z. However, a field parallel to the 2DEG plane allows for coupling only to the spin degree of freedom without giving rise to cyclotron motion. Measurements with a field applied parallel to the 2DEG plane introduce a Zeeman splitting $E_Z = g\mu_B B_z$ which lifts the spin degeneracy, resulting in well defined plateaus at odd integer values of e^2/h, see Fig. 1.8. These plateaus are now understood to be due to transmission of fully spin polarized electrons.

1.1.6 Gate Shape Dependence

Finally, we would like to understand how the lithographic shape of the point contacts affect the quality of the observed quantization. The original devices had lengths typically $L \sim 100$ nm and $W \sim 250$ nm, see Fig. 1.3. Early studies on channels longer than 1 μm did not observe any quantization [111], despite the fact that in principle conductance quantization should occur for $L < l_{mfp}$ and $W \sim \lambda_F$. This discrepancy was attributed to enhanced impurity backscattering [26] or backscattering from channel wall irregularities. Naturally, fabricating higher mobility devices with lower disorder should help, and recent studies have shown that the quantization could persist in quantum wires longer than 1 μm, but the conductance value was more strongly temperature dependent in the longer wires [99, 122]. A rather overlooked but also important indication is that the potential well shape and thus, lithographic gate design, could be important for observing higher quality quantization.

So what kind of shape gives rise to quantized conductance? A key observation is that the confinement is achieved by electrostatic potentials when applying voltage to gates, which must give rise to smooth potentials. Thus, Buttiker argued that the potential well formed by the gates must be a saddle point potential [15], with the following form,

$$V(x,y) = V_0 - \frac{1}{2}m\omega_x^2 x^2 + \frac{1}{2}m\omega_y^2 y^2. \tag{1.20}$$

Here y is the direction along the width and x is along the length of the wire. Taking this potential into account, the x and y motion of the Hamiltonian can be separated, so that the effective potential describing motion along the x direction can be viewed as the band bottom of the nth subband at the saddle point. The transmission probabilities are then given by

$$T_{mn} = \delta_{mn}\frac{1}{1+\exp -\pi\epsilon_n}, \tag{1.21}$$

$$\epsilon_n = \frac{2[E - \hbar\omega_y(n+\frac{1}{2}) - V_0]}{\hbar\omega_x}. \tag{1.22}$$

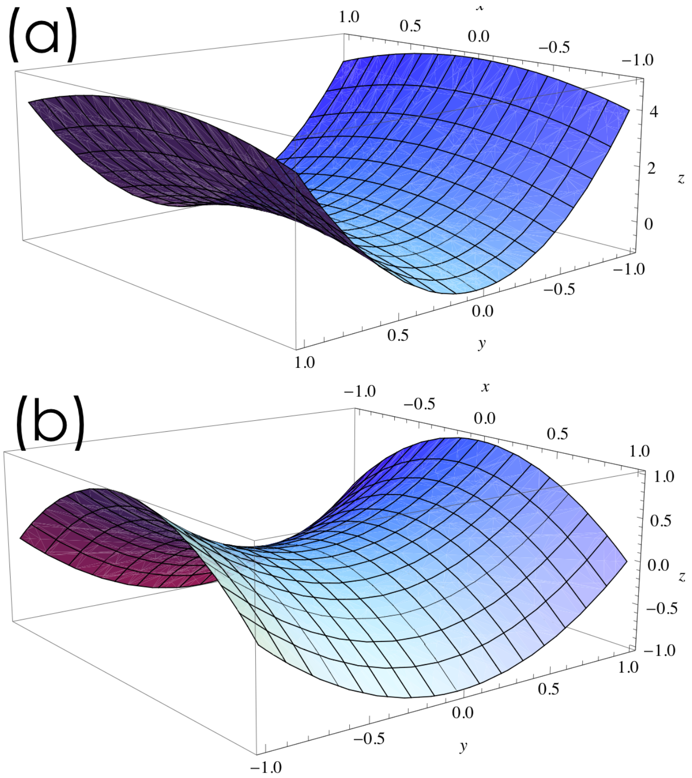

FIGURE 1.9: Shape of saddle-point potential from Mathematica output. (a) $\omega_y/\omega_x = 5$ (b) $\omega_y/\omega_x = 1$.

Here n denotes the incident channel while m refers to the outgoing channels. Transmission probabilities are zero except for the case $n = m$. To observe high quality quantization, the shape of the well along the channel separation W, determined by $\hbar\omega_y$, must be better defined than the transition region for the opening of the quantum channel. More precisely, $\omega_y \geq \omega_x$, as shown in Fig. 1.9. Buttiker showed that as this ratio increases larger than 1, wider and better developed quantized plateaus result. Following along some of these arguments, shallow-etched quantum point contacts with varying shapes were developed with resulting quantization observable up to 30 K [61, 60]. Here, the channel is initially defined by removing unwanted material to create a shape. Then a metallic top gate is deposited on top. The quantization is observed as a function of the top gate placed over the entire constriction region.

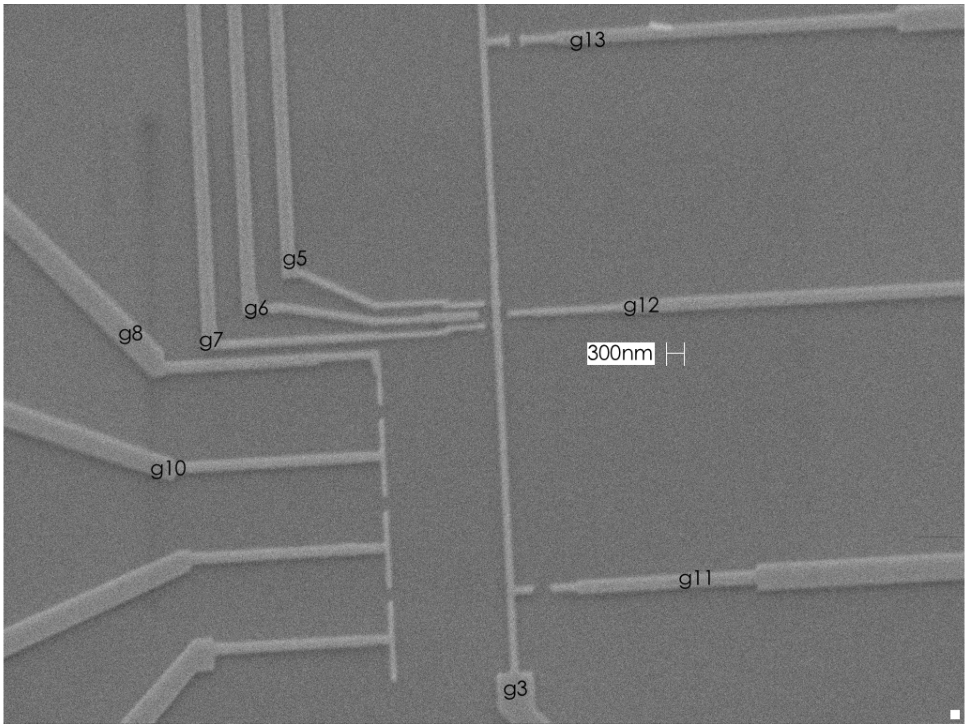

Figure 1.10: SEM image of various QPC shapes.

The subband spacings in these devices reached as high as 10-20 meV, which is much higher than possible for the usual split-gate designs (see Fig. 1.3). However, the width of etched point contacts cannot be tuned laterally as in the split gate case, which is a major drawback.

How then, does one optimize the device dimensions to achieve more perfect quantization and allow for more channels to be measured in field effect confinement QPCs? This will depend on the exact crystal parameters, such as how far below the surface the 2DEG resides. We show in Fig. 1.10 several various QPC shapes patterned on a crystal with 2DEG roughly 80 nm below the surface. The lithographic dimensions (W, L) in nm for the QPCs formed by the pair of gates are: g8-g10 (100,60), g3-g5 (100,60-∞), g3-g11 (200,200), g3-g12 (100,60), g3-g13 (200,100).

Empirically we observe that having $W/L < 1$ seems to allow for more subbands to be observed, and for gates g8-g10 and g3-g11, which have the same lithographic

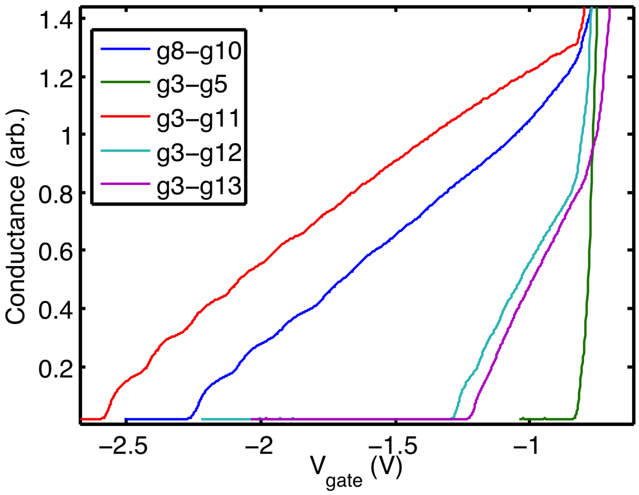

FIGURE 1.11: Conductance traces corresponding to the QPC shapes shown in Fig. 1.10. Measurements were done by dipping the sample in liquid Helium ($T = 4.2$ K). The conductance values here have not been corrected for the series resistance due to the leads.

design, a smaller ratio is better. However, W cannot be arbitrarily small. As we can see in Fig. 1.11, the depletion point is more or less the same for all geometries. This denotes the voltage at which the electron gas beneath the gates are depleted of electrons. Then we enter the regime where we can start to observe conductance quantization. Eventually, as the gate voltage is made more negative, the channel between the point contacts is also fully depleted, and conduction is pinched-off. The pinchoff voltage is quite different for the geometries presented, and in particular, we cannot have W too small so that the pinchoff voltage is very close to the depletion voltage, as for designs g3-g5. In such a situation, the channel is shut just as it becomes well defined.

These studies present a general experimental guideline for designing quantum point contacts. However, a real understanding is best achieved by performing self-consistent potential calculations.

An interesting question to pose is what happens if asymmetries in the potential are introduced? Another way to put it is how do asymmetries in the lithographic design and gating that affect the conductance? We will defer discussion of this important question to Ch. 4.

2

Wigner Crystal in One Dimension

In this chapter, I will introduce the theoretical background for understanding interaction effects in the quantum point contacts. Interacting electrons in 1D are very well described by the Tomonaga-Luttinger liquid (TLL). The TLL theory predicts that spin and charge degrees of freedom will be independent of each other for an interacting 1D system. This spin-charge separation is a hallmark of a 1D system with uniform density. We will see that at low and non-uniform densities, the spin-charge separation is violated in the QPC due to strong Coulomb repulsive energy. This gives rise to spin-incoherent behavior, where the spin degree of freedom depends explicitly on the charge motion. This will have consequences for the observed conductance.

2.1 Interacting Electrons

In the previous chapter, I discussed the conductance quantization through a ballistic semiconducting quantum point contact. In the single channel limit, the conductance was found to be exactly $2e^2/h$, with the factor 2 accounting for two spin degenerate modes. The quantization was understood to arise from the canceling of the density of states with the group velocity in the net current, the theory of which was built up in the framework of a single electron. Quite surprisingly, Thomas et al. noticed a "kink" in the conductance just below the first quantized plateau at $G = 2e^2/h$, see Fig. 1.3 [103, 111]. This feature at approximately $0.7 \times 2e^2/h$ stabilizes with increasing temperature, up to a sample dependent critical value, and is clearly not a result of transmission resonances or impurity scattering [101, 62]. The 0.7 effect cannot be explained in the non-interacting picture, and must arise from electron and spin interactions in the 1D channel.

Possible alternative explanations for the 0.7 feature have been spontaneous spin polarization [103], Kondo-like mechanisms [23], and a phenomenological description of density dependent spin gap that opens in the 1D channel [87, 86]. The primary issue with interpreting the 0.7 effect as a constant spin polarization is the proof by Lieb and Mattis that in 1D, the unpolarized state always has a lower energy than the polarized one. Thus, a ferromagnetic ground state is not possible in 1D [68], though it can be argued that quantum point contacts may not be strictly 1D, but quasi-1D as the confinement is provided by electric potentials. Although the exact mechanism responsible for the 0.7 is still under intense debate, what is clear is that interaction effects from charge and spin motion are critical.

When interactions are present in 1D, the usual Fermi liquid (FL) picture is no longer adequate. Instead, the Tomonaga-Luttinger liquid (TLL) theory is a more appropriate description of the elementary excitations of a 1D conductor with many-body interactions taken into account [50, 70, 38, 53, 54]. In TLLs, low energy short-range interactions give rise to decoupled spin and charge degrees of freedom. The applied bias or current only couples to the charge motion, which contributes $K_\rho e^2/h$, where K_ρ is an interaction dependent parameter. For noninteracting systems, $K_\rho = 1$, while for repulsive interactions, $0 < K_\rho < 1$. Thus, one would expect the conductance at the first plateau to deviate below $2e^2/h$ in the interacting quantum point contacts. The discrepancy with experimental observation was initially explained to be the result of TLL quantum wires connected to FL leads. The quantum wire still has interactions, but the interactions are gradually reduced to zero as the electrons move from the wire into the leads. In the low frequency (DC) limit, the conductance is dominated by the leads and has value restored to $2e^2/h$ [71, 85, 88]. Thus, one expects that interaction effects can not be discerned from transport measurements of interacting wires connected to noninteracting leads.

The observation of the 0.7 effect, which exists in addition to the usual $2e^2/h$ plateau, threw this theoretical framework into disarray. In particular, it suggests that a different framework that considers strong interactions in the channel is needed to describe the transport behavior. The interactions in the point contact may be quite strong due to the low densities $n \ll (a_{Bohr})^{-1}$ near the single channel limit. Here the Coulomb interaction of order $e^2 n/\epsilon$, where $\epsilon = \epsilon_{GaAs} * \epsilon_0 = 13.1 * \epsilon_0$ is the dielectric constant, is much larger than $E_F = (\pi\hbar n)^2/8m$, and so the Coulomb energy dominates the electron kinetic energy. Therefore, the electrons space out equidistantly to minimize the Coulomb repulsion and form an incipient lattice. Such a configuration is termed a Wigner crystal [119, 90, 73]. This regime has not been as widely studied in 1D, and is our primary focus.

Interestingly, Matveev found that depending on the density configuration (with lowest density in the middle of the wire) and thus, energy configuration, of the 1D Wigner crystal, spin and charge can be intricately intertwined [73]. To properly describe the behavior, the spin exchange J had to be considered. At low density, J is exponentially suppressed in the channel as the large Coulomb energy makes spin exchange tunneling processes harder. In this regime, $J \ll T \ll E_F$, and the spin excitations were found to depend explicitly on the charge motion. This implies that spin will affect the conductance, and indeed the single channel conductance is suppressed from $2e^2/h$ to e^2/h in the 1D quantum wire connected to leads [73]. The wire behaves very much like a Tomonaga-Luttinger liquid (TLL) with bosonized charge and spin density waves, but the spin waves are reflected and do not travel through the channel, while the charge waves pass unaltered. At higher densities, where interactions are weaker so that $J \sim E_F$, and thus, $T \leq J$, we expect to return to the TLL picture with fully decoupled spin and charge, and recover conductance of $2e^2/h$. The regime $J \ll T \ll E_F$ has been termed the spin-incoherent Luttinger liquid.

Furthermore, Klironomos, Meyer and Matveev have pointed out that the quasi-1D confinement of quantum point contacts can actually allow for ferromagnetic spin ground states, without violating the Lieb-Mattis rule. Thus, it is possible that this framework may eventually provide a clearer interpretation for the 0.7 effect [56, 55, 75]. To develop a deeper understanding, we now discuss how spin-charge separation arises in 1D.

2.2 Spin-charge Separation in Tomonaga-Luttinger Liquids

The elementary excitations of TLLs are bosonic waves of charge and spin densities propagating at different velocities. In other words, the spin and charge degrees of freedom are decoupled in the 1D channel. Spin and charge remain separated as long as the interaction strengths are less than the respective bandwidths, D, which typically is $\sim E_F$. Thus, the TLL considers 1D regimes with relatively weak interactions, and $T < E_F$. We now briefly summarize the theoretical framework (following Schulz [90] and Matveev [73]).

The concept of spin charge separation results from a bosonization technique [38, 90], which linearizes the spectrum of electrons near the Fermi level, so that the quadratic dispersion is replaced with a linear one. Thus, the electrons are separated into left and right movers with energies $\epsilon_{L,R}(k) = \hbar v_F(\mp k - k_F)$, and the Hamiltonian considered is

$$H = \sum_{k,s} v_F[(k-k_F)a_{k,s}^\dagger a_{k,s} + (-k-k_F)b_{k,s}^\dagger b_{k,s}] + \frac{1}{2L}\sum_q V(q)\rho_q\rho_{-q} + H_{backscatter}, \tag{2.1}$$

where $a_{k,s}^\dagger$ ($b_{k,s}^\dagger$) creates a right (left) moving electron with momentum k and spin projection s. The interaction potential $V(r) = e^2/\sqrt{r^2+d^2}$ is relatively long range, and takes into account small transverse dimension, d, so as to overcome divergences in the Fourier transform at $r \to 0$ for a simple $1/r$ potential. The term $\rho_q = \rho_{a,q} + \rho_{b,q}$ is the Fourier component of the total particle density. Finally, $H_{backscatter}$ describes events where left movers scatter into right movers and vice versa. This contribution comes from $2k_F$ events and will later appear as a $g_{1\perp}$ term. The scattering mechanism is from interaction effects where the spin is flipped, rather than from impurities in the channel.

The Hamiltonian can be solved by introducing Fermionic field operators $\psi_{L,\lambda}$ and $\psi_{R,\lambda}$ for the right and left moving fermions. The operators can be written in terms of fields ϕ_λ and θ_λ, which satisfy bosonic commutation rules $[\phi_\lambda(x), \partial_y\theta_{\lambda'}(y) = i\pi\delta(x-y)\delta_{\lambda\lambda'}]$:

$$\psi_{L,\lambda}(x) = \frac{\eta_{L,\lambda}}{\sqrt{2\pi\alpha}} e^{-ik_F x} e^{i\phi_\lambda(x) - i\theta_\lambda(x)}, \tag{2.2}$$

$$\psi_{R,\lambda}(x) = \frac{\eta_{R,\lambda}}{\sqrt{2\pi\alpha}} e^{ik_F x} e^{-i\phi_\lambda(x) - i\theta_\lambda(x)}. \tag{2.3}$$

Here $\lambda = \uparrow, \downarrow$ is the spin index, α is a short distance cutoff, and $\eta_{L(R),\lambda}$ are Majorana Fermion operators. The Hamiltonian of the interacting 1D system can then be written with these bosonic variables as the sum of two terms, one from charge and one from spin.

$$H = H_\rho + H_\sigma, \tag{2.4}$$

$$H_\rho = \int \frac{\hbar u_\rho}{2\pi} \left[\pi^2 K_\rho \Pi_\rho^2 + K_\rho^{-1}(\partial_x \phi_\rho)^2\right] dx, \tag{2.5}$$

$$H_\sigma = \int \frac{\hbar u_\sigma}{2\pi} \left[\pi^2 K_\sigma \Pi_\sigma^2 + K_\sigma^{-1}(\partial_x \phi_\sigma)^2\right] dx + \frac{2g1_\perp}{(2\pi\alpha)^2} \int \cos[\sqrt{8}\phi_\sigma(x)]dx. \tag{2.6}$$

The new fields, $\phi_{\rho,\sigma} = (\phi_\uparrow \pm \phi_\downarrow)/\sqrt{2}$ and $\Pi_{\rho,\sigma} = \partial_x(\theta_\uparrow \pm \theta_\downarrow)/\pi\sqrt{2}$, satisfy standard commutation relations and represent excitations of the charge and spin degrees of freedom. The Hamiltonian depends on the following parameters: the velocities $u_{\rho,\sigma}$ of charge and spin excitations, dimensionless parameters $K_{\rho,\sigma}^{\pm 1} = 1 \pm g_{1\perp}/2\pi u_{\rho,\sigma}$, and matrix element $g_{1\perp}$ of spin-flip scattering of left moving electrons into right moving ones and vice versa (i.e. back scattering events). For a system with no interactions, $u_\rho = u_\sigma = v_F$, $K_\rho = K_\sigma = 1$, and $g_{1\perp} = 0$. The above framework describes spin charge separation at energies below $D_{\rho,\sigma} \sim \hbar n u_{\rho,\sigma}$.

The interesting quantity to compute is the charge-charge correlation function, with the result shown [90]:

$$\begin{aligned} \langle \rho(x)\rho(0) \rangle =& A_1 \cos(2k_F x) exp(-c_2\sqrt{lnx})/x \\ &+ A_2 \cos(4k_F x) exp(-4c_2\sqrt{lnx}) + \ldots . \end{aligned} \tag{2.7}$$

Only the most slowly decaying Fourier terms are shown, with interaction dependent $A_{1,2}$ and $c_2 = \sqrt{(1+g_{1\perp})\pi u_\rho/e^2}$. The most important observation is the slow decay of the $4k_F$ term, which is an incipient charge density wave at $4k_F$. For short range interactions, the $2k_F$ and $4k_F$ terms are expected to decay as a power law (x^{-1-K_ρ} and x^{-4K_ρ}, respectively) [16, 90]. These oscillations with period $4k_F$ are precisely the average interparticle spacing expected for a Wigner crystal. Although there is no true long range order in a 1D system, it is nonetheless surprising that the $4k_F$ term results. This implies that even in a theoretical picture of relatively weak interactions, as long as the interaction spread is *relatively long range*, then a Wigner type lattice will be able to form.

2.3 One Dimensional Wigner Crystal

In practice however, the long-range potential is destroyed in 1D predominantly by quantum fluctuations and also by partial screening from a top metal gate electrode. This implies that the Wigner crystal can only persist in a critical density range. We consider a metal plane gate a distance d away from the quantum wire, which modifies the Coulomb interaction potential to the following:

$$V(x) = \frac{e^2}{\epsilon}\left(\frac{1}{|x|} - \frac{1}{\sqrt{x^2 + (2d)^2}}\right). \tag{2.8}$$

At large distances the potential decays much more rapidly than the usual $1/r$ as $V(x) \sim 2e^2d^2/\epsilon|x|^3$. Thus, the lower bound for Wigner crystallization is set by $a_{Bohr}d^{-2} \ll n$, provided that the gate is far enough away, $d \gg a_{Bohr}$. The upper bound is as usual, with $n \ll a_{Bohr}^{-1}$. In GaAs, the typical Bohr length is

$$a_{Bohr} = 4\pi\epsilon\hbar^2/me^2 \simeq 100\mathring{A}, \tag{2.9}$$

with $\epsilon = \epsilon_{GaAs} * \epsilon_0 = 13.1\epsilon_0$ and $m = m_{GaAs} * m_e = 0.067m_e$, while the gates are at least ten times the distance (80 nm in our sample). Thus, it is possible, theoretically, to achieve the Wigner crystal with the 1D quantum point contacts.

2.3.1 Charge and Spin Excitations

The assumptions considered in building the Hamiltonian describing the Wigner crystal are different from that for the set of equations resulting in TLL. Here, we are in the limit of strong interaction forces, and it may be useful to think of the crystal as a continuous medium with propagating waves of electron density, or acoustic plasmon excitations. Thus we consider a charge Hamiltonian of the form:

$$H_\rho = \int \left[\frac{p^2}{2mn} + \frac{1}{2} mns^2 (\partial_x u)^2 \right] dx. \tag{2.10}$$

Here $p(x)$ is the momentum density, $u(x)$ is the displacement of the medium at point x from equilibrium, and the term s describes the speed of plasmons:

$$s = \sqrt{\frac{2e^2 n}{\epsilon m} ln(8.0nd)}. \tag{2.11}$$

Equation 2.10 completely describes the low-energy excitations for a spinless system, and in fact describes the same physics as Eq. 2.5 if we identify the following equivalences:

$$\phi_\rho(x) = \frac{\pi n}{\sqrt{2}} u(x), \tag{2.12}$$

$$\Pi_\rho(x) = \frac{\sqrt{2}}{\pi n \hbar} p(x), \tag{2.13}$$

$$u_\rho = s, \tag{2.14}$$

$$K_\rho = \frac{\pi \hbar n}{2ms}. \tag{2.15}$$

To incorporate the additional effects from spin, we utilize the Heisenberg antiferromagnetic exchange,

$$H_\sigma = \sum_l J S_l \cdot S_{l+1}. \tag{2.16}$$

This is a reasonable approach as we imagine the Wigner lattice as equidistantly spaced localized charge, which to a first approximation do not have coupled spins.

The exchange of spins is exponentially suppressed due to strong Coulomb repulsion and only nearest neighbor interactions play a significant role. The Heisenberg exchange model can be shown to be equivalent to Eq. 2.6 when the excitation bandwidths are much smaller than exchange, $D \ll J$. This is via a bosonization technique [73], and from that the speed of the spin excitations can be extracted as

$$u_\sigma = \frac{\pi J}{2\hbar n}. \tag{2.17}$$

What of the exchange J term? If we only consider pure Coulomb interaction, the exchange has form,

$$J = J^* exp(-\eta/\sqrt{n a_{Bohr}}), \tag{2.18}$$

$$J^* \approx 1.79 \frac{E_F}{(n a_{Bohr})^{3/4}}. \tag{2.19}$$

Here, $\eta \approx 2.82$ for an infinite chain of electrons and $E_F = (\pi\hbar n)^2/8m$. As for the Coulomb potential, we also consider the limit where effects of a metallic screening gate could be large. In such a case, the decrease of the exchange with decreasing density is expected to saturate when $n \sim d^{-1}$. Thus, according to Matveev [73], for $a_{Bohr}/d^2 \ll n \ll d^{-1}$, the exchange is estimated to be,

$$J = E_F(\frac{nd^2}{a_{Bohr}})^{3/4} exp(-8.49\sqrt{\frac{d}{a_{Bohr}}}). \tag{2.20}$$

At lower densities, the exchange constant has a power-law dependence on the density. At exceptionally low densities, $n \leq a_{Bohr}/d^2$, the exchange term is found to be similar to Eq. 2.20, but nd^2/a_{Bohr} goes as the first power instead of 3/4 [73].

The above derivations imply that the bosonized Hamiltonians for low energy, weakly interacting 1D TLLs, Eqs. 2.5 and 2.6, also work for the Wigner crystal in the strong coupling regime, but at $T \ll J$. However, the strong exponential dependence of J on the density also suggests that one can easily enter a regime where $J \ll T$. In such a case, the equivalent picture for the spin density waves breaks down, and we must use Eq. 2.16 to describe the spins. The charge motion is still adequately described by the bosonized picture as long as $T \ll E_F$.

2.3.2 Violation of Spin-charge separation

In experimental devices, it is reasonable to expect that the density of the entire system of quantum point contact connected to leads is not entirely uniform, $n = n(x)$. The density is likely to be higher close to the edges of the point contact than at the center, and the width also widens near the edges. Güclü et al. have substantiated this hunch and found from simulations on realistic confinement potentials that the density in the 1D channel can indeed be rather non-uniform and low at the center [35]. The low and non-uniform density configuration leads to a position dependent exchange J in the point contact, illustrated in Fig. 2.1. The strength of the exchange coupling between neighboring spins will then depend on the position of the spins. Thus, for the lth and $l+1$ electron, $J = J(x_l)$, where $x_l = x(l,t)$ is in general a function of both the lth lattice site and time. Time dependence of the position arises from the fact that the Wigner lattice moves in the presence of an electric current. Thus, considering that a number $q(t)$ electrons move in time t through the channel, we can expect the lth lattice site to have moved to position $l + q$. This analysis modifies the Hamiltonian to,

$$H_\sigma = \sum_l J[l + q(t)] S_l \cdot S_{l+1}. \tag{2.21}$$

Quite importantly, the q dependence of Eq. 2.21 means that the coupling between spins depends on the amount of charge passing through the wire. This Hamiltonian, which arises from the assumption of inhomogeneous density in the quantum point contact connected to leads, violates the spin-charge separation observed earlier, with important measurable consequences in the conductance.

2.3.3 Charge and Spin Contribution to Conductance

We first estimate the contribution to the conductance from the charge dynamics based on Eq. 2.5. First we consider an infinite wire without attachment to leads, and we bias to drive an AC current $I = I_0 \cos\omega t$ at $x = 0$. In terms of the plasmon velocities, we have $I = en\dot{u}$. This imposes the following boundary condition on $\phi_\rho(0,t)$:

$$\phi_\rho(0,t) = \frac{\pi}{\sqrt{2}} \frac{I_0}{e\omega} \sin\omega t = \frac{\pi}{\sqrt{2}} q(t). \tag{2.22}$$

We can then find the fields ϕ_ρ and Π_ρ, which gives the following time-averaged energy density,

$$\langle E \rangle_t = \frac{\pi\hbar}{4e^2} \frac{I_0^2}{K_\rho u_\rho}. \tag{2.23}$$

We are effectively driving the system with an oscillating external force, leading to emission of plasmon waves which dissipates into the larger reservoir. The total energy dissipated by the waves then is $W = 2u_\rho \langle E \rangle_t$, which we compare to the well known Joule heat law (time-averaged) $W = \frac{1}{2} I_0^2 R_\rho$ to find,

$$R_\rho = \frac{h}{2K_\rho e^2} = \frac{1}{G_\rho}. \tag{2.24}$$

In the strong coupling Wigner crystal, we found that the spin Hamiltonian is modified to Eq. 2.21, which now depends on the oscillating parameter $q(t)$. This adds an additional series resistance to the wire due to spin [74, 73, 75], $R = R_\rho + R_\sigma$.

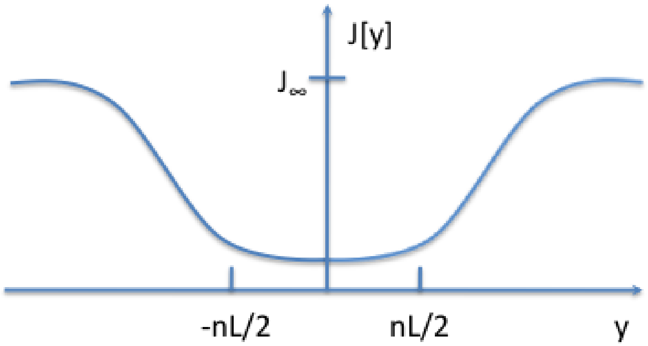

FIGURE 2.1: Sketch of the y dependence of position dependent J. J is exponentially small inside the wire, $-nL/2 < y < nL/2$, and saturates to $J_\infty \sim E_F$ close to the leads.

The resistances are in series and not in parallel because the spins do not directly respond to the bias and instead are driven by the change in electron number or electrical current.

Matveev estimated the value of R_σ by assuming J to be slowly varying in the channel with form

$$J[y] = \begin{cases} J \ll E_F & \text{at } |y| < nL/2 \\ J_\infty \sim E_F & \text{at } |y| \to \pm\infty. \end{cases} \tag{2.25}$$

This allows the spin chain to be approximated by a homogeneous Heisenberg model, which can be solved with a Bethe ansatz, giving "spinon" particles with spectrum $\epsilon(k) = \frac{\pi J}{2} \sin k$ as the elementary excitations. This points to a threshold energy $\pi J/2$ for spinon propagation, with the J referring to the smallest value in the channel. Spinons with energy less than $\pi J/2$ pass through the channel without issue, while those with larger energies are reflected by moving scatters, which are a result of the time dependence of J (due to $q(t)$). At low temperature, $T \ll J$, the resistance due to spinons is exponentially small, $R_\sigma = R_0 \exp(-\frac{\pi J}{2T})$. Here R_0 is a model dependent prefactor.

For $T \gg J$, but still $T \ll E_F \sim J_\infty$, all spinons are expected to be reflected. The dissipation R_σ is not easy to calculate in this regime, but Matveev conjectures that the result should be similar to any problem where all the spin excitations are reflected by moving scatterers. Thus, at $T \gg J$,

$$R_\sigma = \frac{h}{2e^2}. \tag{2.26}$$

This result combined with Eq. 2.24, points to an overall conductance that is reduced to $G = e^2/h$ as the density in the constriction is reduced. This is the primary theoretical prediction concerning the conductance.

2.3.4 Zigzag and Unusual Spin Configurations

Aside from the predictions on the measurable conductance, what other interesting behavior might result from the 1D Wigner crystal? The strong Coulomb repulsion in the channel forces a relaxation of the confinement, so that the wire is no longer strictly 1D, but rather, has a quasi-1D configuration. Instead of a linear chain of electrons, more exotic arrangements such as a zigzag are now possible, as shown in Fig. 2.2. As mentioned earlier, several studies indicated the possibility for unusual spin states in the zigzag state [57, 56, 55]. The argument here is that in such a zigzag chain, it is possible for the distance between next-nearest neighbor electrons to be smaller than the nearest-neighbor. Thus, the exchange between next-nearest neighbors, J_2, may be equal to or exceed the nearest-neighbor exchange, J_1. Competition between the two exchange energies may frustrate the antiferromagnetic ground state, and three or more particle ring-exchange processes could become possible. The ground state for odd number of electron interactions then, is likely to be ferromagnetic in nature [56]!

Is this a realistic situation for quantum point contact 1D channels? We con-

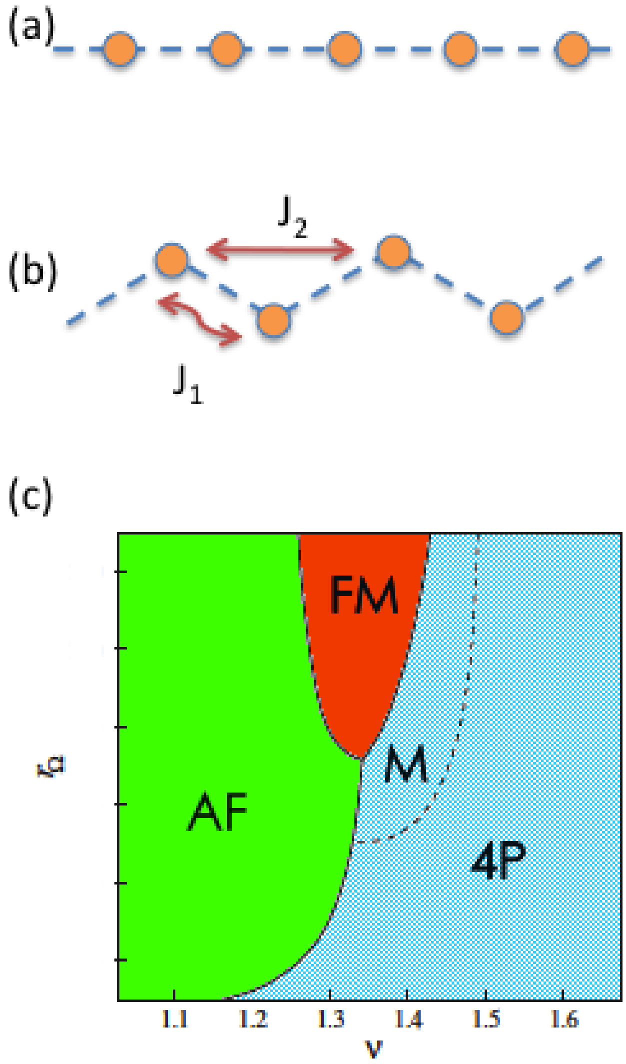

FIGURE 2.2: Zigzag in quasi-1D quantum point contact. (a) The zigzag conformation is characterized by the dimensionless number $\nu = n_{1D} * r_0$ (see text). As interactions become stronger, a zigzag shape results (b), with various possible exchange mechanism, such as the nearest neighbor J_1 and next-nearest neighbor J_2. (c) Phase diagram following that shown in Ref. [55]. r_Ω is defined in the text. For a linear chain (low ν), antiferromagnetism (AF) is the possible magnetic behavior. In the density range allowing for zigzag to form, exotic magnetic behaviors such as ferromagnetism (FM), four-particle ring exchange (4P) and partial polarization (M) are predicted to occur.

sider the parabolic confinement potential along the y-axis (quantization direction) $V_{conf}(y) = \frac{1}{2}m\Omega^2 y^2$, with Ω the frequency of harmonic oscillations. The condition for zigzag Wigner crystal to form is when the Coulomb energy is comparable to the confinement, $V_{coul}(r_0) = V_{conf}(r_0)$. Thus, a zigzag develops when the distances between electrons are on the order of

$$r_0 = \left(\frac{2e^2}{4\pi m\epsilon\Omega^2}\right)^{\frac{1}{3}}. \tag{2.27}$$

As r_0 has units of length, we can define a dimensionless quantity to describe the zigzag by multiplying the 1D density, n_{1D}.

$$\nu = n_{1D} * r_0. \tag{2.28}$$

Theoretical studies indicated that a 1D crystal as in Fig. 2.2(a) is stable for $\nu < 0.78$, while zigzag chains, Fig. 2.2(b), form from $0.78 < \nu < 1.75$. Larger channel density gives larger ν, which correlates to a larger distance between the zigzag rows. The primary result, is that in such a range of ν, it becomes possible to support a ferromagnetic state as well as other exotic spin states, as shown in the phase diagram of Fig. 2.2.

Here, $r_\Omega \equiv r_0/a_{Bohr}$ is a scaling factor which quantifies the strength of the electron-electron interactions. As can be seen, at low ν, which corresponds to a linear chain, the expected magnetic behavior is antiferromagnetic regardless of interaction strength. This is expected for a strictly 1D system as argued by Lieb-Matthis. At the correct density range for zigzag formation however, the magnetic behavior is not so simple. When interactions are not strong, it is possible to have various ring exchange processes, denoted as 4P. This exotic state is not well understood, and we refer the reader to these theoretical papers [56, 55, 75] for more on this topic. However, the prediction is that if interactions are strong, then it is possible to have a partial polarization region M, and above this, at stronger interactions, a ferromagnetic state is possible, FM.

3

Experimental System Fabrication and Measurement Techniques

In the first part of this chapter, I describe the experimental system studied. Then I detail procedures for nanoscale electron beam lithography device fabrication. Finally, I will discuss electronic measurement techniques used.

3.1 High Mobility 2DES

The advent of molecular beam epitaxy (MBE) in the 1960s, and its subsequent development into a now very mature technology, has allowed researchers to realize the growth of many types of novel semiconducting structures. MBE allows for the precise placement of single atoms, so that growth can be controlled layer by layer. Growth of heterojunctions, which is the broad term for materials that are grown composed of two semiconductors with different band gaps and crystalline structure, became possible. This in turn, led to the development of heterostructures (crystals with multiple heterojunctions) and other devices, such as the heterojunction bipolar transistors (HBT) [79], high mobility electron transistors (HEMT) [76], and quantum

Table 3.1: Lattice constants and energy gap for several III-V ternary compounds.

Compound	Lattice constant ($\AA$)	Energy gap (eV)
AlAs	5.6611	2.168
GaAs	5.65325	1.424
InAs	6.0583	0.354
InP	5.8687	1.344
Si	5.431	1.12

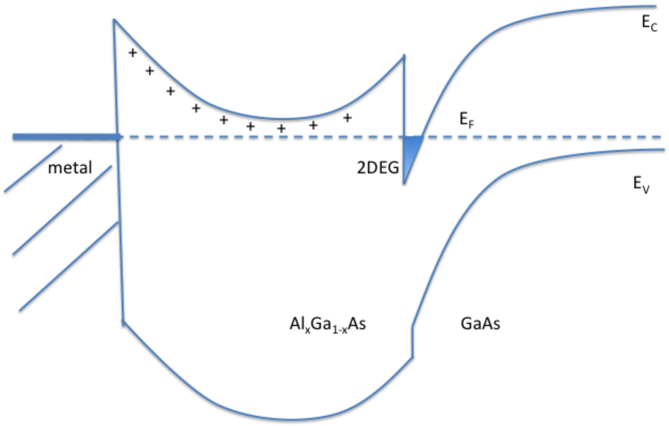

FIGURE 3.1: Band diagram of a modulation doped GaAs-$\mathrm{Al}_x\mathrm{Ga}_{1-x}$As heterostructure. A 2DEG is formed at the interface of the undoped GaAs with p-type doped AlGaAs.

cascade lasers [30].

A simple but rather ideal model to understand what happens when two materials of different band gap and crystalline structure are meshed together is the electron affinity rule [1]. The rule assumes that the vacuum levels of the two materials align at the junction, and therefore the conduction band offset $E_{C1} - E_{C2} = \Delta E_C$ equals the difference in electron affinities $\chi_1 - \chi_2 = \Delta\chi$. This allows one to calculate the conduction and valence band offsets. Once thermal equilibrium is reached, the Fermi levels of the two materials also match, and this enables a more detailed calculation of the final band bending. Band gap structure of most heterojunctions can be classified as straddled, staggered or broken.

However, this simple model does not account for lattice mismatch between materials, which naturally have different lattice spacings. Lattice constants for typical III-V ternary compounds are shown in Table 3.1. The model is also unable to accurately describe most observed band gap values as the electron affinity can depend on surface states and electron correlation effects. In particular, it does not predict the quantum well formed at the junction of the GaAs and AlGaAs, see Fig. 3.1, the experimental test system that is studied in this thesis. A more accurate description, the effective dipole model [5, 100], assumes the conduction band offset to be the difference in the Schottky barrier height. Essentially, dipole charges arise from locally different atomic and electronic structure at the interface in comparison to the bulk, and these charges dictate how the bands merge. This model works well for AlGaAs-GaAs structures (material parameters and electronic properties are shown in Table 3.2). The lattice constant in $\mathring{A}$ and energy gap in eV can be estimated for $\mathrm{Al}_x\mathrm{Ga}_{1-x}\mathrm{As}$ with the following:

$$a = 5.6533 + 0.0078x, \tag{3.1}$$

$$E_g = \begin{cases} 1.424 + 1.247x & \text{for } x < 0.45 \\ 1.9 + 0.125x + 0.143x^2 & \text{for } x > 0.45. \end{cases} \tag{3.2}$$

Two dimensional electron gases are interesting from both a fundamental and applications point of view. As the name implies, a 2DEG is a physical realization of a two dimensional Fermi gas. Fundamental phenomena such as the integer and fractional quantum hall effect, noncompressibility of Fermi liquids, have been observed in clean 2DEGs. This has opened up the possibility for observation of new physics, such as anyon and non-abelian statistics. On the applications side, 2DEGs have been important for ultrafast transistor operation, and more recently, as a potential test

Table 3.2: Electronic properties and parameters in GaAs-AlGaAs 2DEG heterostructures and Si inversion layers.

Property	GaAs(100)	Si(100)	Units
m	$0.067m_e$	$0.19m_e$	g
g_s	2	2	
g_v	1	2	
ϵ	$13.1\epsilon_0$	$11.9\epsilon_0$	F/m
$\rho(E) = g_s g_v(m/2\pi\hbar^2)$	0.28E-11	1.59E-11	$\text{cm}^{-2}\text{meV}^{-1}$
n_s	4E11	1-10E11	cm^{-2}
$k_F = (4\pi n_s/g_s g_v)^{(1/2)}$	1.58E6	0.56-1.77E6	cm^{-1}
$v_F = \hbar k_F/m$	2.7E7	0.34-1.1E7	cm/s
$E_F = (\hbar k_F)^2/2m$	14	0.63-6.3	meV
μ_e	10^4-10^6	10^4	cm^2/Vs
$\tau = m\mu_e/e$	0.38-38^1	1.1	ps
$D = v_F^2\tau/2$	140-14000	6.4-64	cm^2/s
$\rho = (n_s e\mu_e)^{-1}$	1.6-0.016	0.63-6.3	kΩ
$\lambda_F = 2\pi/k_F$	40	35-112	nm
$l = v_F\tau$	10^2-10^4	37-118	nm
$l_\phi = (D\tau_\phi)^{1/2}$	200-$\cdots$	40-400	$\text{nm(T/K)}^{-1/2}$
$l_T = (\hbar D/k_B T)^{1/2}$	330-3300	70-220	$\text{nm(T/K)}^{-1/2}$
$l_{cyc} = \hbar k_F/eB$	100	37-116	nm(B/T)^{-1}
$l_m = (\hbar/eB)^{1/2}$	26	26	$\text{nm(B/T)}^{-1/2}$
$k_F l$	15.8-1580	2.1-21	
$\omega_c\tau$	1-100	1	B/T
$E_F/\hbar\omega_c$	7.9	1-10	(B/T)^{-1}

system to realize quantum and topologically fault-tolerant computation [93, 94, 13].

One of the key ideas that made 2DEGs useful and ubiquitous is modulation doping, which is achieved with a Si δ-doping layer in AlGaAs-GaAs structures [28, 97]. The Si atoms in GaAs effectively separate the donors from the charge carriers, which reduces scattering affects and thus, enhances the electron mobility in the quantum well. 2DEGs can now be consistently grown with mobilities on the order of 10^7 cm^2/Vs at low temperature [84]. In general, the mobility increases very rapidly as the temperature is decreased, then saturates. Sample mobilities can be enhanced by illuminating with a light emitting diode [114].

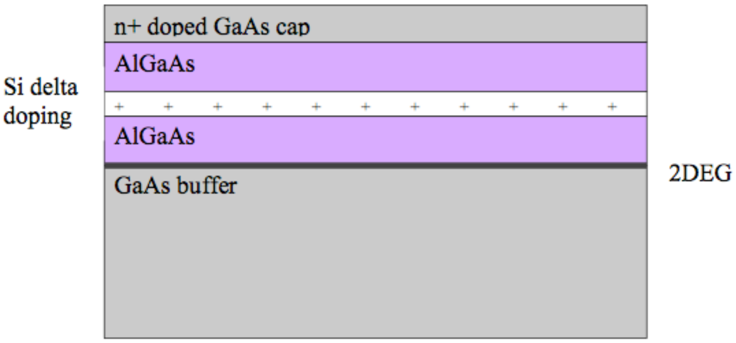

Figure 3.2: Layer by layer schematic of a typical GaAs-AlGaAs heterojunction. Specific details for structure used in this thesis are in the text.

A typical high mobility structure, see Fig. 3.2, consists of a relatively thick 0.2 - 1 μm buffer layer of GaAs, followed by an $Al_{0.3}Ga_{0.7}As$ spacer layer of $\sim$ 10-30 nm, a silicon δ-doping layer, and an additional 50-70 nm of $Al_{0.3}Ga_{0.7}As$ to bring to a total thickness of $\sim$ 80 nm of $Al_{0.3}Ga_{0.7}As$. This is capped with an n+ doped 6 nm GaAs cap layer. The total thickness from the heterojunction is roughly in the 90-100 nm range. Typically, the AlGaAs layer is kept relatively thin to reduce the chance for a parallel conduction channel arising.

The GaAs/AlGaAs heterostructure used in this thesis contains a 2DEG 80 nm below the surface, and the 2DEG mobility and density was $\mu = 9 \times 10^5$ cm^2/Vs and $n = 3.8 \times 10^{11}$ cm^{-2} at 4.2 K, respectively.

3.2 Device Fabrication

3.2.1 Electron Beam Lithography - Standard Procedures

Quantum dot and quantum point contacts in the 2DES can be fabricated by standard lithography methods. To begin with, a GaAs-AlGaAs wafer is cleaved to roughly 3 mm by 3 mm size. The size upper bound is restricted by the size of the sample holders (14 pin DIP socket, Newark 614-AG1 or Bond socket D14 Side Braze, Spectrum

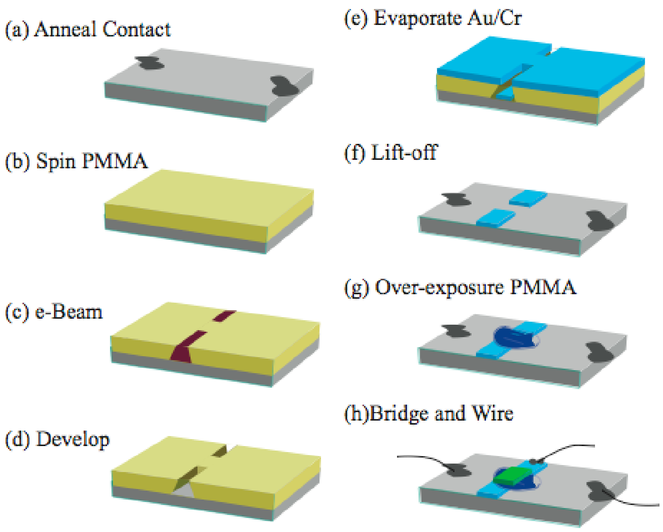

FIGURE 3.3: Schematic of sample fabrication procedure. Explanations are given in the text.

Semiconducting Materials Inc. CSB01419), while naturally the lower bound is chosen so that it is not too difficult to handle and see the crystal. The cleaved crystal is ultrasonically cleaned (Paragon Electronics Bransonic B3510) in a two step process of acetone then isopropanol wash for five minutes each, then blow dried with dry N_2 gas.

Next, electrical contact must be made to the 2DES, Fig. 3.3(a). As shown in the figure, pure Indium (In) contacts are soldered onto the top surface of the crystal. A homemade annealing station is utilized to heat the crystal in N_2 ambient atmosphere, so that the In diffuses from the top surface into the underlying electron gas. A photo of the annealer is shown in Fig. 3.4. Annealing procedures that I use are: 1) Place sample on the silicon carbide heating plate, close and screw cap tight 2) Fill with pure N_2 gas for 4 minutes 3) Heat to 435°C in ~2 minutes 4) Hold at 435°C for 4 minutes 5) Lower temperature to room temperature 6) Shut off gas and remove crystal.

The sample is now ready for the lithography process. The first step is to spincoat

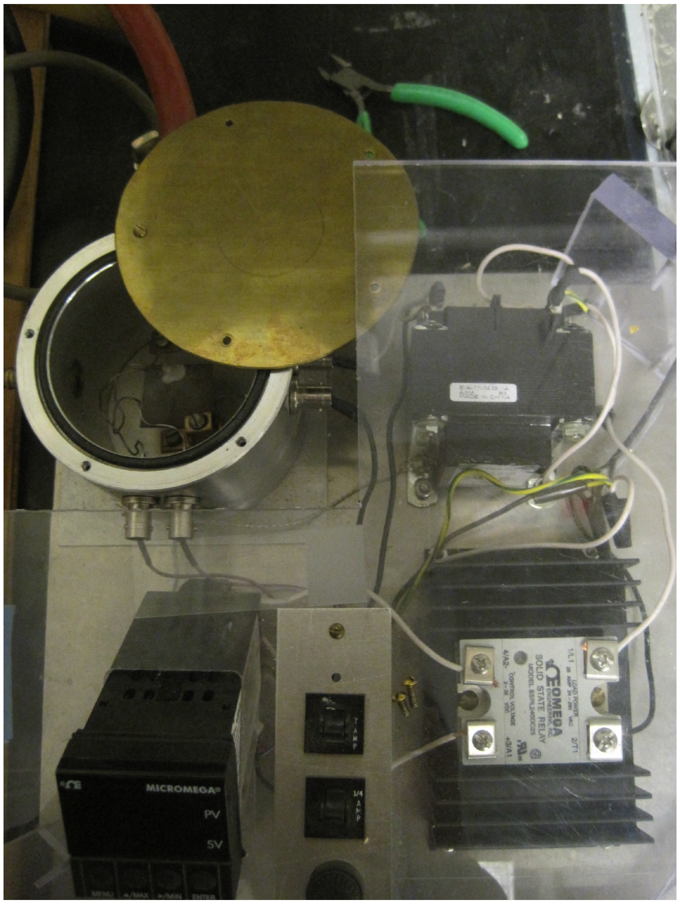

FIGURE 3.4: The annealing station uses a Micromega CN77343 dual output controller with Micromega SSRL240DC25 3-32 Vdc solid state relay. TRIAD VPS24-3300 class B power transformer is used. The heating plate is silicon carbide and thermocouples are used to measure the temperature. This annealing station was designed and built by Nathan Kundtz.

(Specialty Coating Systems P6700 Spincoater) the crystal with the synthetic polymer poly(methyl methacrylate) or PMMA, Fig. 3.3(b). Electron beam (Ebeam) or UV light illumination severs the polymer crosslinks in PMMA, which allows for the PMMA to be patterned into a mask to define nanostructures with line resolutions achievable in our lab around 30 nm on GaAs (Leo 440, 30 kV ebeam). I utilize Nano PMMA 495 (molecular weight) diluted to 4% in Anisole; the lower molecular weight is chosen such that thinner films can be spun, and thus, finer lithographical features achieved. Typical spincoating speeds are 5500 RPM for 45 s (ramp up to 2000 RPM in 2 s, then to 5500 RPM in 1s). The final PMMA thickness for this spin speed is approximately 100-200 nm. The PMMA is then baked at 120°C for 30 minutes. Then, as in (c), the pattern designed is "written" with the ebeam, which follows commands from a computer program. The Proxy ebeam cad program as well as more detailed ebeam settings will be discussed below in 3.2.2. But briefly, to achieve 50 nm line widths, a box feature is set at roughly 120% dose with 20 pA beam current for 14 μs so that the optimal undercut is formed. Typical ebeam doses are in the range 100-400 $\mu C/\mathrm{cm}^2$. Scattering effects of the incident electron beam in PMMA have been thoroughly studied [41, 80, 42, 69]. The long polymer chains broken down by ebeam bombardment can then be removed with a developer (methyl isobutyl ketone: isopropanol or MIBK:IPA in 1:3 ratio) which leaves an undercut in the PMMA as in (d). As the developing time is also a variable that determines the PMMA undercut, I fix the MIBK:IPA rinse time at 30 s, while maintaining freedom to change the beam parameters. Residual droplets of developer are immediately blown dry with N_2 gas after rinse.

The sample is now ready for metal evaporation Fig. 3.3(e). Depending on the particular device design, gold (Au), chrome (Cr), titanium (Ti) or aluminum (Al) may be deposited. We utilize an ancient (but still dependable and rather versatile due to the large bell jar space) Varian thermal evaporator (Automatic Deposition System 985-7009). Au is a commonly used material for surface gates as it does not oxidize, but the downside is that it does not naturally stick well to GaAs. Thus, combinations of Cr/Au or Ti/Au (5 nm/20 nm thickness) are used, with the "stickier" Cr or Ti providing the more dependable adhesion to the GaAs. The PMMA mask is "lifted-off" with acetone, step (f), leaving only metal deposited on the crystal surface. Au wire can then be wire-bonded or In soldered to provide electrical contact (Sigmund Cohn Corp. 98% Au, 2% Sn 0.002" size 171004).

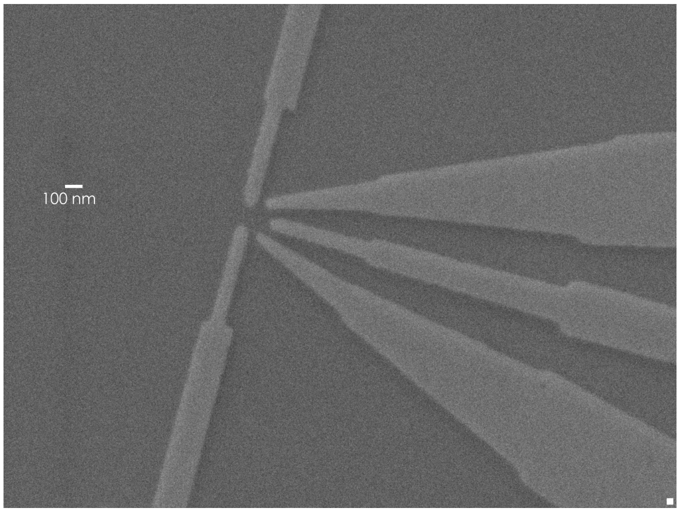

FIGURE 3.5: This is a single quantum dot structure formed from five Cr/Au top gate contacts. The darker colored regions are the bare top GaAs top surface, while the lighter structures are the deposited metal. The width of the gates at the tip ends are approximately 100 nm. Scale bar is 100 nm.

In cases where there are several lithographic procedures required, an O_2 plasma etch (Technics PE II-A Plasma System) is sometimes required to remove residue PMMA after the developing step (d). The residue PMMA could have built up if the beam exposure is not fully optimal, and the chances of this occurring is greater with designs that require multiple ebeam writes. The residue may prevent the deposited metal from actually adhering to the GaAs surface, and thus, the entire metallic feature could be removed during acetone lift-off.

A typical finalized device would look as in Fig. 3.5. These are SEM images looking from the top down, with the dark regions corresponding to the bare GaAs, and the bright features are the deposited metal. A larger field image of the same device is shown in Fig. 3.6. The gate electrodes are shorted to each other to prevent a potential from developing across the tips and causing discharge damage. Prior to device operation, the grounding shorts can be disconnected simply using a diamond scribe to remove some of the metal.

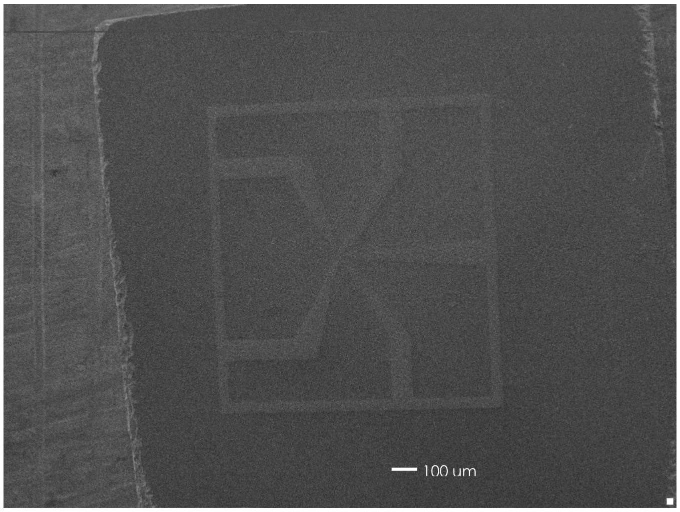

Figure 3.6: The five gate electrodes are shorted to each other so that the entire sample can be maintained at the same ground. This is done to prevent a potential from developing across the tips (see Fig. 3.5) and causing the small gate features to be damaged or "blown-up." Scale bar is 100 μm.

More fancy structures can be readily designed, but at the potential cost of having additional ebeam writes and/or additional metal depositions. The likelihood of failure or error also increases with complexity. Two additional useful fabrication techniques, PMMA overexposure and double angle evaporation, that I have utilized previously are discussed in Appendix B.

3.2.2 Gate Design - Proxy

Various shapes can be designed in the Proxy cad program. We utilize the box and contour shape command to accomplish this. However, the driving factor for pattern design is function. In the context of quantum point contacts, the shape of the patterned metallic gate will greatly influence the shape of the potential well in the 2DEG. As discussed in Ch. 1, Buttiker has shown that transmission through a saddle-point potential will give rise to conductance plateaus [15]. A truly accurate analysis however, requires self consistent potential calculations, taking into account the heterostructure design and gate geometry [24, 81, 82, 19, 64]. Simple electostatics

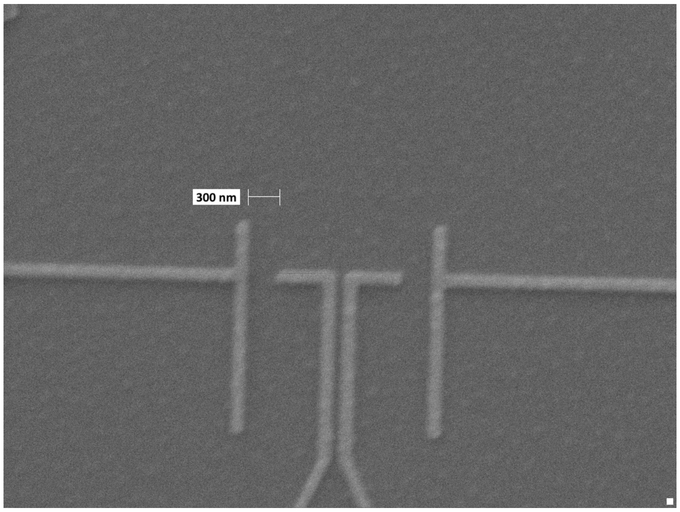

Figure 3.7: Asymmetrical quantum point contact with 300 nm gap width. The wall gate has length of $l = 1$ μm. Ti/Au metal of 10 nm/20 nm thickness is used for the gates.

for various shapes can be calculated based on the work of Davies et. al. [25].

Here I include the detailed Proxy values used to fabricate the gate patterns studied in this thesis.

Figure 3.7 is an SEM micrograph of an asymmetrical quantum point contact similar to those used to study spin-incoherent transport. We utilize three separate

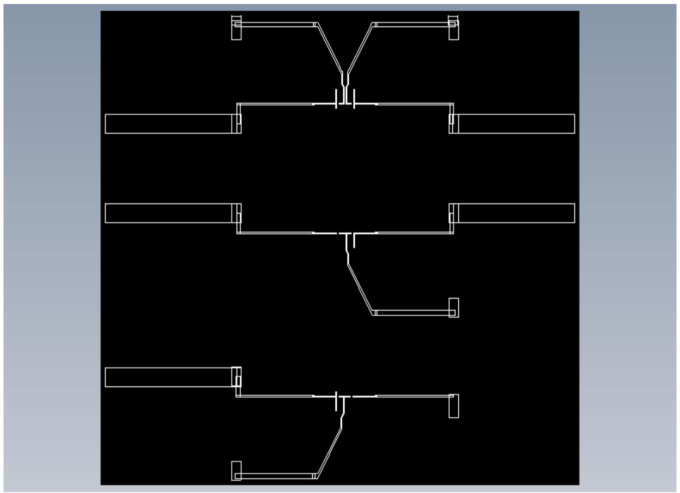

Figure 3.8: 50 μm by 50 μm Proxy pattern for the image in Fig. 3.7

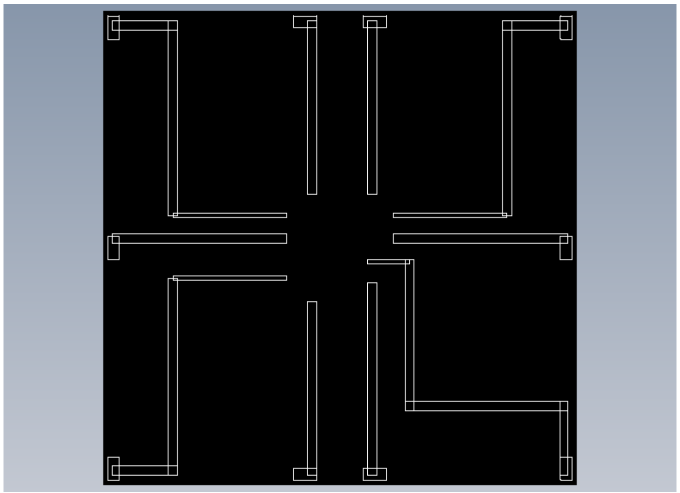

FIGURE 3.9: 200 μm by 200 μm Proxy pattern that is exposed following the pattern in Fig. 3.8.

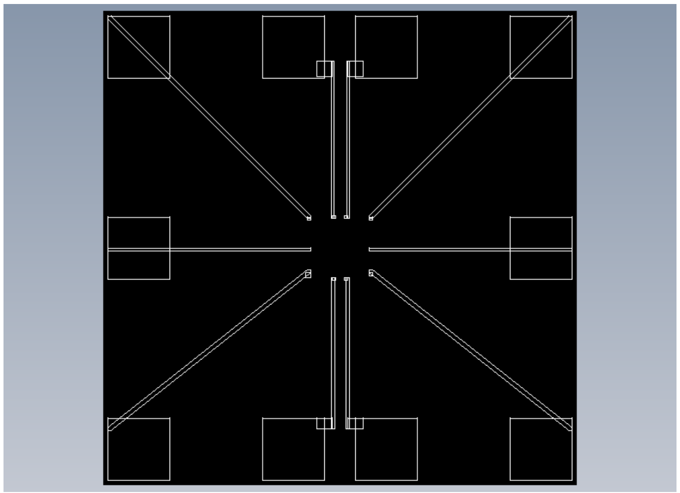

FIGURE 3.10: 1500 μm by 1500 μm large feature. This pattern ensures the contact pads are large enough to be seen by eye for In soldering.

exposure steps to write the device, starting from smallest to largest. In the first step, a field size of 50 μm by 50 μm with 4000 times magnification is written at 20 pA beam current with typically 10-15 μs dwell times. Figure 3.8 shows the design for the image in Fig. 3.7. The finest features are written in this step (roughly 60-100 nm in Fig. 3.8). Then the 200 μm by 200 μm features magnified to 1000 times is exposed with $\sim$ 100 pA current for 27 μs. Finally, the pattern with 1500 μm by 1500 μm field size at 133 times magnification is defined with $\sim$ 3000-3300 pA current for 32 μs. The large field patterns for the device of Fig. 3.7 are shown in Figs. 3.9 and 3.10. In this way, alignment can be ensured so that the smallest features are properly connected to the larger contact pads.

3.3 Measurement Techniques

In Fig. 3.11 I show a schematic of the basic (differential) conductance measurement setup. I utilize the PAR124 lockin to generate an AC excitation voltage of 17.3 Hz to the sample to serve as the source-drain bias. Here no DC voltage is applied. Typically, the 100 mV output at the lockin will be voltage divided to around 10 μV so that $V_{sd} \ll k_B T$. It's also important to remember not to use a huge shorting resistor value compared to the sample resistance.

The current from the sample is brought out to a current preamplifier. We have several available in our lab, either J. C. Chen's homemade preamp with OPA-128 chips or the Ithaco 1211. For most of the measurements discussed in this thesis, the Ithaco preamp is used. Typically, amplification is tuned to 10^{-5} to 10^{-6} A/V, as the currents are on the order of nA. The converted voltage signal is sent back to the PAR124 lockin for detection at 17.3 Hz, with usual time constants of 300 ms to 1 s.

Voltages to deplete the quantum point contact gates are applied via a homemade DAC power supply with +10V to -10V full range and 10 MΩ current limiting resistors. Typically, I limit the voltage to ±5 V, as the sample breakdown voltage is

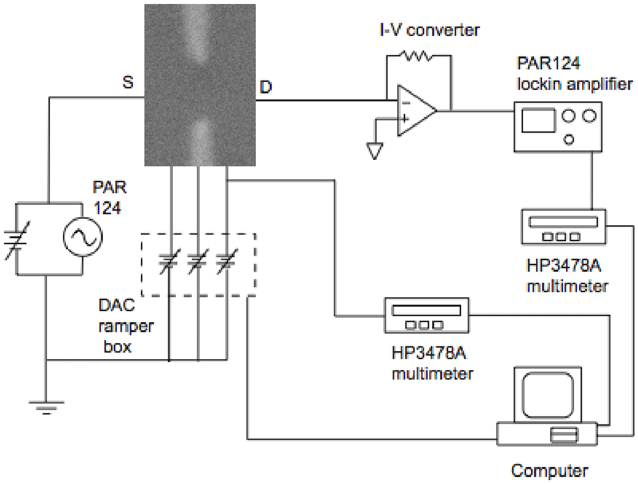

FIGURE 3.11: Setup for measuring the (differential) conductance through a quantum point contact.

reached around -4V.

To gain more information about the transport properties, differential conductance versus a DC source-drain bias can be measured. This is done by adding a small AC signal on top of a DC source-drain bias. Adding AC to DC can be accomplished with an isolation transformer, Geoformer G-40 from Triad-Utrad 17-8223 (or a biastee), paying special attention to the ground configuration. In our setup, the AC signal ground is isolated from the ground of the shielding box, which is tied to the ground of the DC power source and sample, see Fig. 3.12. The current through the quantum point contact as a result of this voltage bias is converted to voltage at the preamp and measured in the lockin.

3.3.1 Homemade Sample Measurement Probes

Figure 3.13 show homemade He3 system measurement probes and a liquid He4 sample dipstick. These probes are meant for operation in an Oxford He3 cryostat with base temperature 300 mK and a helium dunker, respectively. The He3 cryostat was

Figure 3.12: Transformer box for AC+DC addition.

custom fitted with a triaxial magnet allowing up to 4 T in the vertical z and 200 mT in the horizontal x directions. The dunker has a single z field up to 6 T.

The He3 sample probe and holder was custom designed for both DC and coaxial connections. Four stainless steel cables can be seen in the figure. Larger diameter flexible stainless steel coax was wired from room temperature down to roughly 1 K (where the sample probe thermally contacts the 1Kpot), then switched to semi-rigid mini-coax. A pc board designed with 50 Ω microstrips connects the different coaxial cables. Constantan DC cables were used from room temperature down to base temperature. There are 4 coaxial connections and 18 DC wire cables available for measurement.

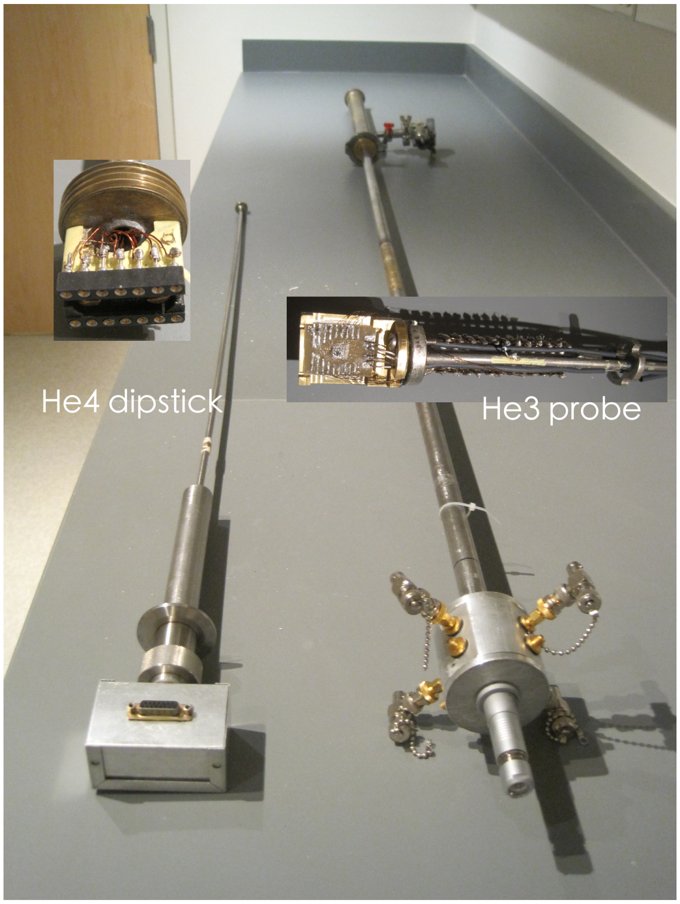

FIGURE 3.13: Homemade He3 measurement probe and He4 sample dipstick. Insets show the sample holder design. The dipstick allows for 14 pin connection, while the He3 probe has 18 DC wire connections and 4 coaxial connections.

The He4 dipstick is much simpler in design, and consists of only copper wires from top to bottom. The socket holder is a 14 pin dip socket mounted on brass.

4

Asymmetric Quantum Point Contacts

At the end of Ch. 1, I raised the question of what would happen to the conductance if asymmetries were introduced into the potential that defines the quantum point contact? I consider the following two ways to introduce asymmetries: first, into the lithographic gate design, and second, by gating asymmetrically. Asymmetries in the lithographic design can be introduced as in Fig. 4.1. Essentially, instead of trying to create gates that are mirror-images of each other, we make one gate longer than the other.

The potential that defines the gates can be tilted as in Fig. 4.2. Consider the gates V1 and V2. The conductance traces in the past have usually been obtained by applying voltages equally to V1 and V2. This creates a potential that possibly looks like the bottom left figure of Fig. 4.2. The QPC can be asymmetrically gated by applying unequal voltages to V1 and V2.

4.1 Asymmetrically Gating Symmetric QPC

First let us look at the case where voltages are applied asymmetrically to a symmetric lithographic geometry, for example, the constriction formed by V1 and V2 in Fig.

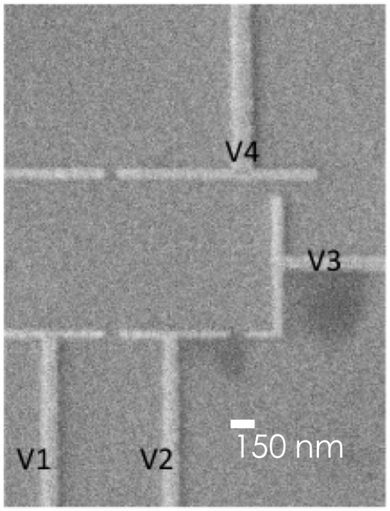

FIGURE 4.1: SEM image of symmetric and asymmetric QPC geometries. The gates V1 and V2 are mirror-images of each other, and together form a symmetric QPC. V3 and V4 have quite different lengths, and so are asymmetric.

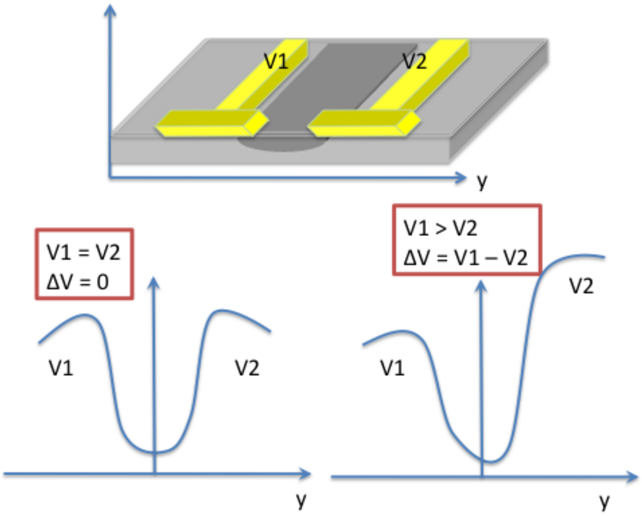

FIGURE 4.2: Schematic of potential profile under symmetric and asymmetric gating. The top image is a side view of the crystal with 2DEG beneath the surface. Voltages are applied to metallic gates V1 and V2 deposited on the surface to deplete the electron gas.

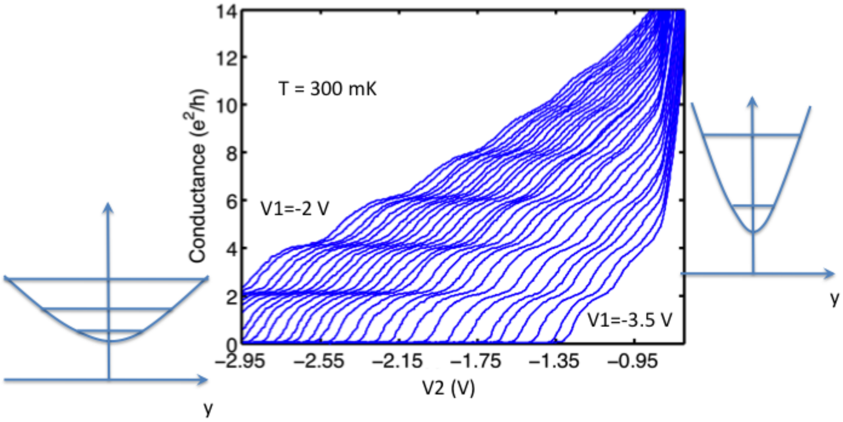

FIGURE 4.3: Asymmetrically gating symmetric QPC. Here we asymmetrically apply voltages to V1 and V2, shown in Fig. 4.1. Voltages are fixed on V1 from -2 V to -3 V, with 50 mV decrements. The voltage on V2 is swept at each fixed value of V1. A slight kink at $1.5e^2/h$ is discernible in some of the traces, but there are no other significant anomalous conductance features observable.

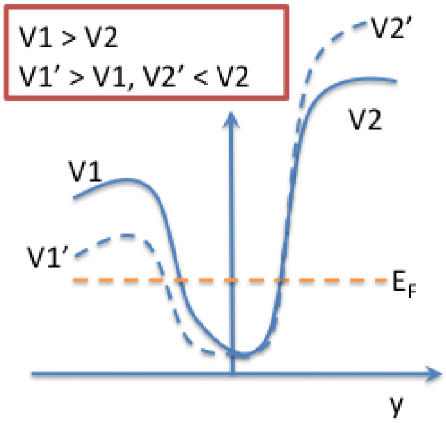

FIGURE 4.4: Schematic of potential of asymmetrically gated symmetric QPC. As the voltage on the gate is made more positive, the potential wall becomes more shallow. Making the gate voltage more negative sharpens the wall. In the figure, we imagine a situation where $\Delta V \leq \Delta V'$, with ΔV =V1 − V2 (solid), and $\Delta V'$ =V1' − V2' (dashed).

4.1. Here, $W = 100$ nm and $L = 60$ nm. The measured conductance traces are shown in Fig. 4.3. Each individual trace is taken by sweeping the voltage on V2 with voltage on V1 fixed. The leftmost trace has V1 $= -2$ V, which is decreased by 50 mV steps as we move rightwards. The rightmost trace has V1 $= -3.5$ V. The first observation is that asymmetrically gating a symmetric QPC does not seem to introduce any unusual behavior in the conductance quantization. All the plateaus at even multiples of $2e^2/h$ are still there, and there are no substantial anomalous features (there is a slight kink at $1.5e^2/h$ in most of the traces). The pinchoff positions for the traces are shifted, though as expected, the depletion point stays the same. Second, it is important to note that in going from left to right, the number of conductance plateaus drops. This means that are fewer number of subbands accessed, and this gives an indication of the potential shape. On the left, as shown in Fig. 4.3, the potential has a shallower shape, while on the right, the potential wall increases much more sharply. The shape shift changes the subband energies spacing, while the Fermi energy is fixed. Thus, there are less total number of subbands below the Fermi energy, and fewer quantization plateaus are observed.

The fact that nothing unusual is observed under asymmetric gating is not that surprising. By making V1 $\neq$ V2, the curvature of the potential wall is only slightly changed, see Fig. 4.4. However, the shape near the band bottom is expected to be essentially unaffected. This means that the quantization of subbands still remains, though as one edge dips lower and lower, for example by making V1 less negative, the number of subbands below the Fermi level decreases, in agreement with experimental results.

4.2 Asymmtrically Gating Asymmetric QPC

Next, consider what happens if the gate geometry itself has significant asymmetries, for example, in gates V3 and V4 in Fig. 4.1, which has a point contact gap $W = 250$

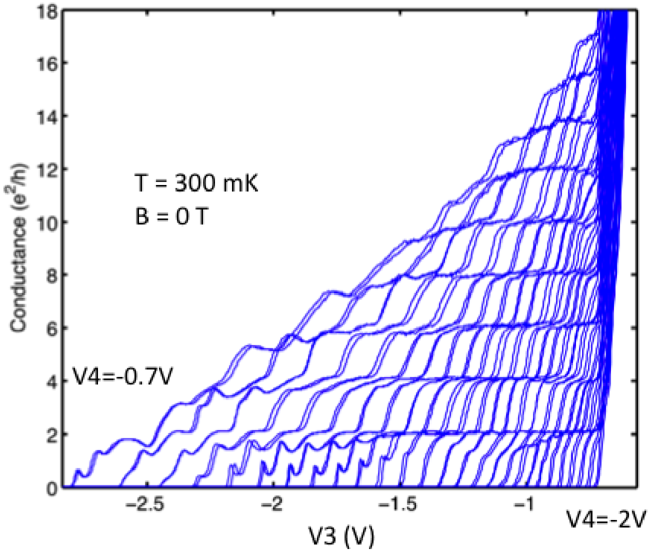

FIGURE 4.5: Asymmetrically gating asymmetric QPC. Here we asymmetrically apply voltages to V3 and V4, shown in Fig. 4.1. Voltages are fixed on V3 from -0.7 V to -2 V, with 50 mV decrements. The voltage on V4 is swept at each fixed value of V3.

nm, and short edge length $L = 100$ nm. The measured conductances are shown in Fig. 4.5. The voltage on V4 is kept fixed from -0.7 V to -2 V in 50 mV decrements, while V3 is swept from 0 to -3 V. Quite interestingly, a number of unexpected features are observed below the first quantization plateau at $2e^2/h$. The traces are taken twice to show the reproducibility of the features during each cooldown. In particular, we focus on the following two features, shown in Fig. 5.1. The red trace shows a well developed e^2/h feature, while the blue curve has no anomalous conductance below $2e^2/h$. As was discussed in Ch. 1, plateaus at odd multiples of e^2/h develop under a strong magnetic field, which spin polarizes the electrons. It is quite interesting that such a strong feature at e^2/h is observed in the asymmetric geometry, even when there is no applied magnetic field! We will further discuss this well developed e^2/h feature and its implications in the next chapter. However, the fact that we can tune through this regime to one with no anomalous features perhaps indicates that

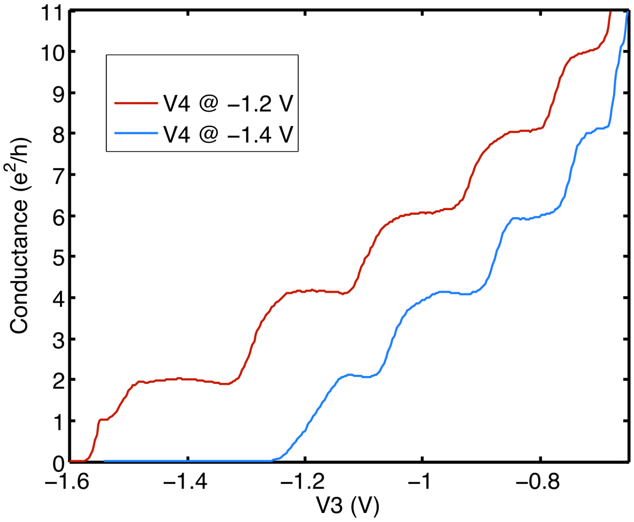

FIGURE 4.6: Conductance of asymmetric QPC with $e^2/h(2e^2/h)$ feature shown in red(blue).

asymmetrically gating the asymmetric geometry is drastically altering the transport dynamics by changing the confinement potential profile.

In a hand-wavy sort of argument, let us recall that for a saddle-point potential, a larger ω_y/ω_x ratio gives rise to better, or wider, quantized plateaus. In Fig. 4.5, we indeed see that going from right to left, the quantized plateaus seem to be wider. The leftmost trace corresponds to a less negative $V3$, or in other words, the channel is likely closer to V3. This observation seems consistent with the fact that we have a slightly longer x confinement (longer V3 length). This argument needs to be substantiated by self-consistent potential calculations.

4.3 Optimizing Asymmetric QPC Gap Width

What is clear from these results is that the asymmetric QPC geometry seems to give rise to very unusual conductance behavior. We decided to focus on this aspect and more fully investigate the geometry related or induced effects. Let us consider the series of gates shown in Fig. 4.7, which have gap widths of 450 nm (g1-g3), 350

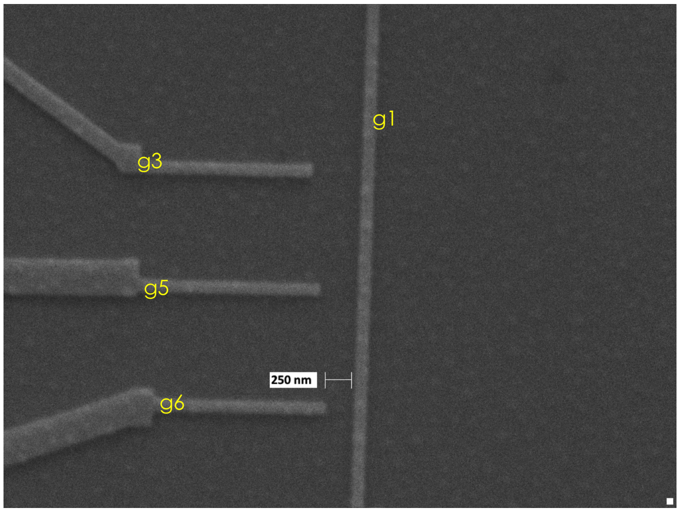

FIGURE 4.7: Asymmetrical quantum point contacts with gap widths of 250, 350 and 450 nm. The gates are Ti/Au::10nm/20nm.

nm(g1-g5), and 250 nm (g1-g6). The length of the short gate is 100 nm for all three constrictions.

Figures 4.8, 4.9, 4.10 show the asymmetrical gating conductance traces for the 450 nm, 350 nm, and 250 nm devices, respectively. While measuring each point contact, the gates for the other two were grounded. Thus, when measuring the constriction formed by g1-g3, for example, gates g5 and g6 were grounded so as not to influence the charge configuration. Clearly, in all three measurements, anomalous conductance features below $2e^2/h$ are observable. This is additional validation that the asymmetric geometry is important.

In Fig. 4.10, which is for the 250 nm gap width, a very unusual feature marked by the red arrow is noticeable. It seems that the conductance at the $2e^2/h$ plateau is drastically suppressed to e^2/h. This feature occurs very near the right edge of traces, indicating that at this gap width, the potential wall is rather sharp. Quite interestingly, such a trace was not observed in the 350 nm gap or the 450 nm gap. This seemed to indicate that there is an optimal gap width for observing the interesting

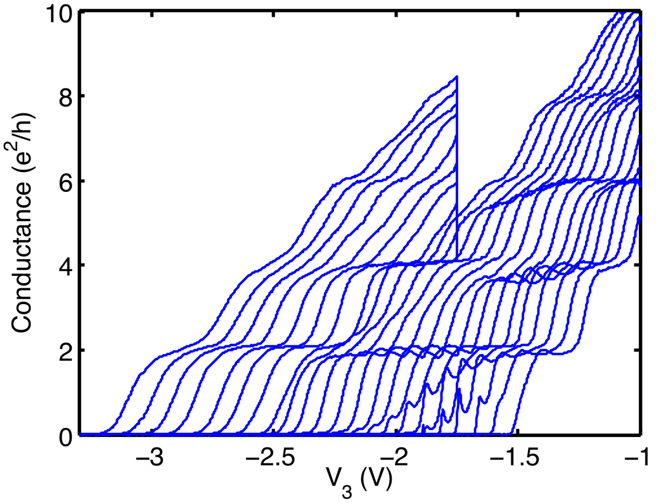

FIGURE 4.8: Asymmetrical voltage sweep of 450 nm (g1-g3)asymmetric QPC at 300 mK. g1 is set from -2.5 V (leftmost) to -3.5 V (rightmost) in 50 mV steps.

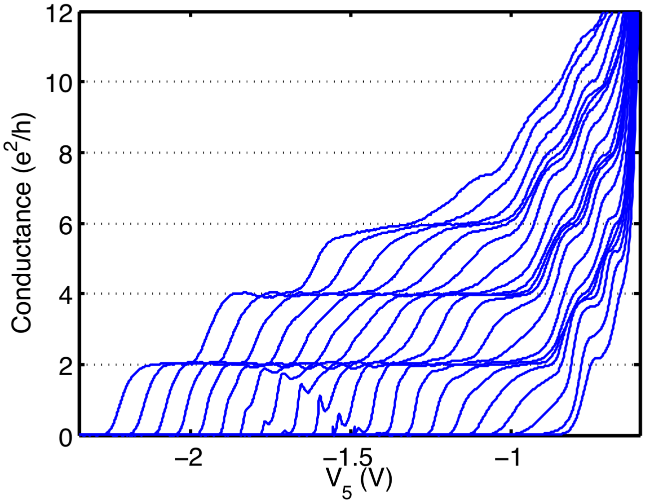

FIGURE 4.9: Asymmetrical voltage sweep of 350 nm (g1-g5) asymmetric QPC at 300 mK. g1 is set from -2 V (leftmost) to -3 V (rightmost) in 50 mV steps.

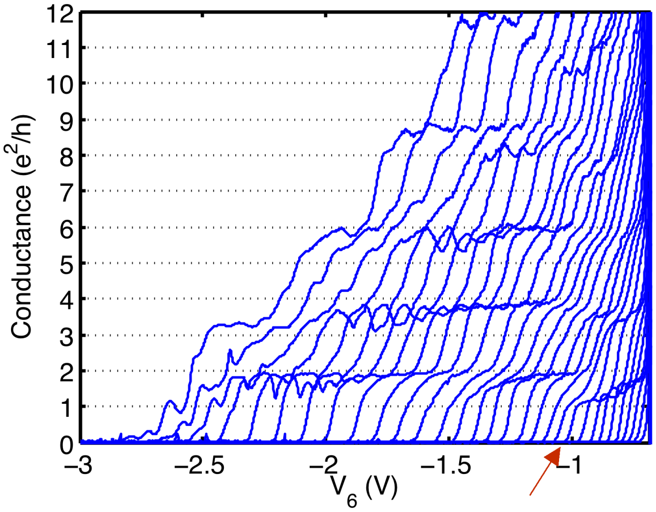

FIGURE 4.10: Asymmetrical voltage sweep of 250 nm (g1-g6) asymmetric QPC at 300 mK. g1 is set from -1 V (leftmost) to -2.5 V (rightmost) in 50 mV steps. Quite interestingly, the trace denoted with a red arrow has a suppressed $2e^2/h$ plateau.

conductance behavior.

Thus, I made a 300 nm gap sample, and the result of the asymmetrical gate tuning is shown in Fig. 4.11. Here, we see that we are clearly able to tune through the suppressed conductance regime.

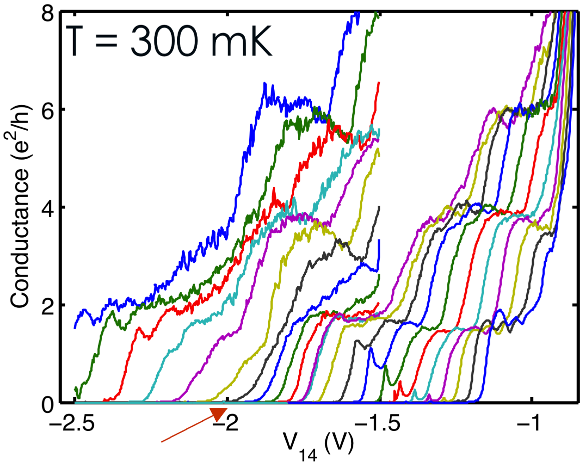

Figure 4.11: Asymmetrical voltage sweep of 300 nm (g2-g14)asymmetric QPC at 300 mK. g1 is set from -1.5 V (leftmost) to -2.5 V (rightmost) in 50 mV steps.

5

Electron Correlations in Asymmetric Quantum Point Contacts

5.1 Spin-incoherent Regime and Possible Wigner Crystallization

As discussed in Ch. 1, the conductance of a one dimensional conductor (quantum wire) is known to be quantized in units of $G = 2e^2/h$. The observed experimental result can be explained in a noninteracting electron picture with each subband contributing equally to the conductance. Intriguingly, at low electron density, anomalous behavior unexpected for noninteracting electrons occurs below the first subband at zero field at $0.7 * 2e^2/h$ [103] and sometimes $0.5 * 2e^2/h$ [87]. The origins of the conductance features are still under debate, with one possibility discussed in Ch. 2 being the formation of a Wigner crystal in the quantum wire [119, 90].

Wigner crystallization becomes feasible in a specific low density range, $a_{Bohr}d^{-2} \ll n \ll a_B^{-1}$. In this limit, the kinetic energy of electrons, which is typically $E_F = (\pi\hbar n)^2/8m$, is small compared to the Coulomb interaction between electrons, of order e^2n/ϵ. Thus, electrons prefer to "keep a distance" and form a lattice with equidistant spacings to minimize the repulsive Coulomb energy. Electronic transport through such a lattice is closely related to the spin-incoherent Luttinger liquid regime, where electron-electron interactions separate the spin and charge modes of propagation. Spin-incoherent transport is described as the sum of the spin and charge modes, Eq. 2.24, $R = R_\rho + R_\sigma$. For large exchange processes $T \ll J$, the spin contribution is small so that the total conductance remains quantized at $2e^2/h$. However, in the spin-incoherent regime [32], $J \ll T \ll E_F$, spin contributes $R_\sigma = h/2e^2$ (Eq. 2.26) to the resistance, giving a total conductance which is suppressed to $G = e^2/h$.

Here we present evidence for conductance behavior that is attributed to the spin-incoherent regime in quantum wires formed by split-gate quantum point contacts, and signatures related to possible Wigner crystallization in one dimension are also observed. Specifically, we observe traces with a well developed e^2/h feature at zero magnetic field, Fig. 5.1 (red trace). This conductance behavior agrees with the predicted signature of a spin-incoherent Luttinger liquid. As the channel density is reduced by applying more negative gate voltage to V3, the conductance at $2e^2/h$ drops to e^2/h. This occurs when the density of the channel is reduced to less than the inverse Bohr radius ($a_{Bohr} \sim 10$ nm in GaAs). We know the density is in the correct regime based on subband depopulation measurements shown below. Strong Coulomb interaction in the channel localizes the electron motion, which allows for possible zigzag conformation and exotic spin exchange mechanisms. This state is possibly related to the $0.7(2e^2/h)$ effect (or $1.5e^2/h$ in our language) observed in 1D quantum wires [103, 23, 87].

To compare the behavior to known results, we look at the differential conductance under a source-drain bias, dI/dV_{SD}. The measurement methods are described in Ch. 3.3, and the result is shown in Fig. 5.2. Applying a DC source-drain bias introduces a voltage difference between the chemical potentials on either side of the QPC. The bunching of the traces in Fig. 5.2 correspond to plateaus in the conductance.

We find that the e^2/h structure is indeed related to $1.5e^2/h$ by applying a DC

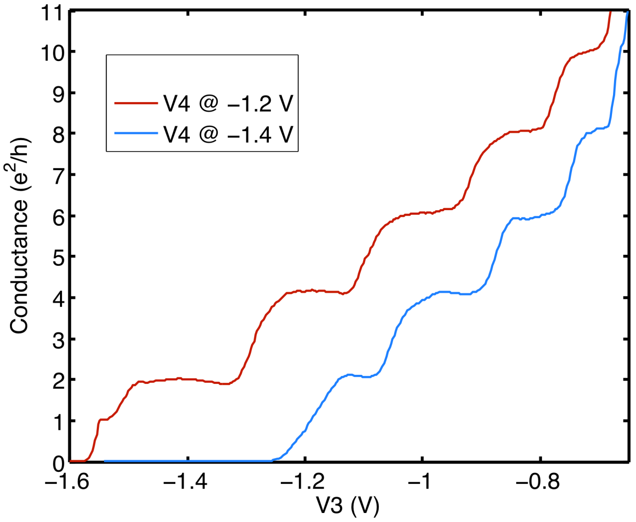

FIGURE 5.1: Conductance of asymmetric QPC with $e^2/h(2e^2/h)$ feature shown in red(blue).

source-drain bias, Fig. 5.2(left panel). Note that an e^2/h plateau typically develops under a strong magnetic field which spin polarizes the electrons. Here, no magnetic field is applied. Figure 5.2(a) is quite similar to the result obtained in [23], but their trace is taken at a field of 8 T. In their paper, the voltage where the e^2/h bunch merges into $1.5e^2/h$ is 0.2 mV, which is consistent with the 8 T field. Recall that $E_Z = g\mu B_z$, where $g = -0.44$ gives a conversion of $g\mu \sim 25\mu\text{eV/T}$. In our case, the transition occurs at approximately 1 mV, which translates to a Zeeman splitting of nearly five times as large as previous works [23]! This suggests a strong zero field polarization of the electrons, and is experimental evidence that the spin-incoherent wire has undergone a transition from a linear chain to a zigzag Wigner crystal formation which could support a ferromagnetic state. At the moment, we do not fully understand the ripples observed in the regions between the e^2/h to $2e^2/h$ bunches.

Figure 5.3 shows conductance traces for the 300 nm gap sample (shown in inset) at 4.2 K with asymmetric gating. Data taken at 300 mK on a similar geometry was

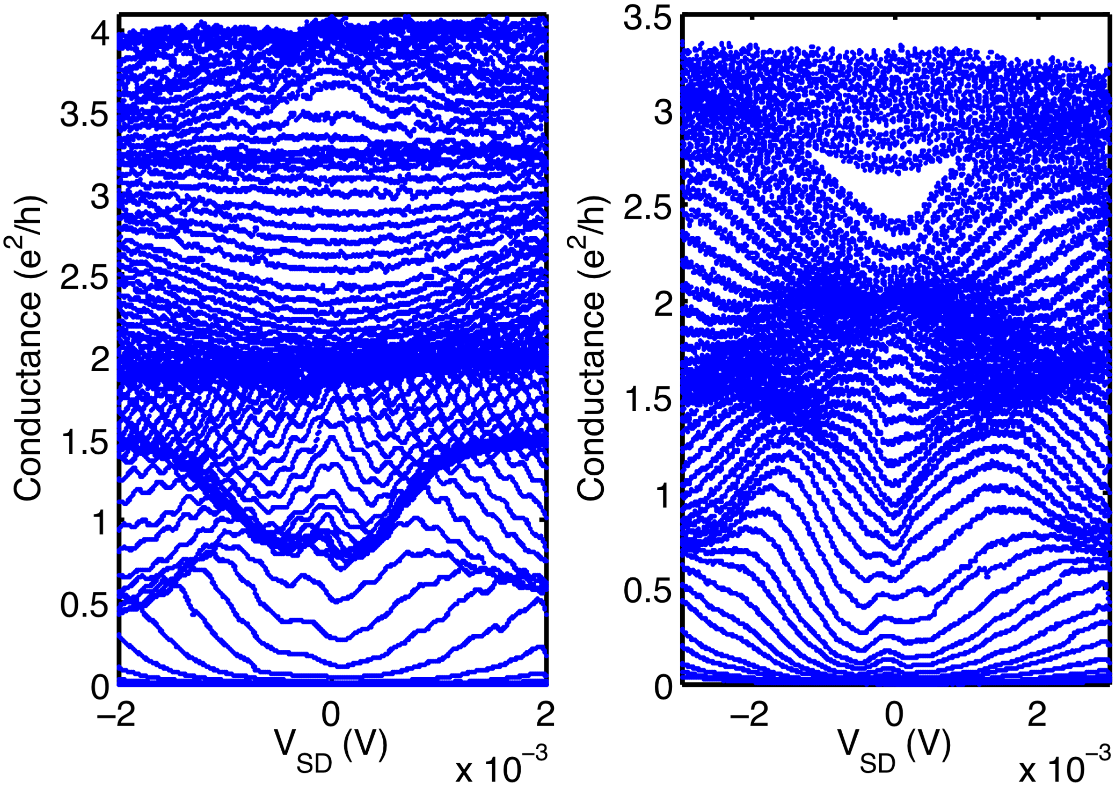

FIGURE 5.2: Differential conductance versus source-drain bias of asymmetric QPC when (a) the conductance has a strong e^2/h feature (red trace in Fig. 5.1) and (b) when there are no anomalous features below $2e^2/h$ in the conductance (blue trace in Fig. 5.1).

shown previously, Fig. 4.11. Here, each trace is obtained by sweeping the finger gate with the wall gate set at a fixed voltage. We caution against placing too much emphasis on the precise voltage value, as depending on the cool-down procedure, which determines the initial local charge configuration, the voltages shift in value. However, the qualitative features are stable over a single cooldown and reproducible over multiple thermal cycles and in a separate device. From left to right, the wall gate is made successively negative starting from $V_{wall} = -2$ V (in decrements of 50 mV steps). The density of successive conductance traces drops going from left

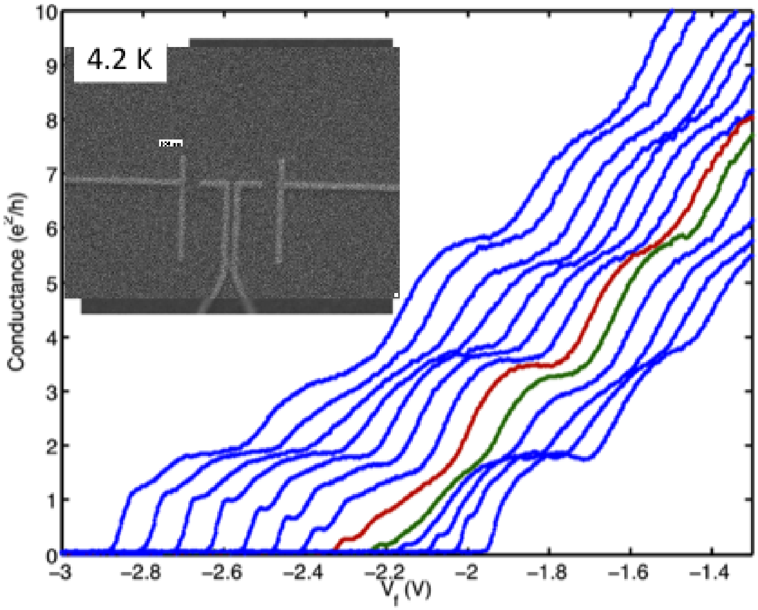

FIGURE 5.3: Conductance through $W = 300$ nm asymmetric QPC. Dotted (colored) lines measured with V_{wall} set at fixed voltage from -2 V (leftmost) to -2.6 V (rightmost) in 50 mV decrements while sweeping V_f. Inset shows the sample gate geometry.

to right, indicated by the increasingly positive pinchoff value and reduced number of conductance plateaus. We note several interesting regimes, similar to previous observations [45, 96]. First, the system enters the spin-incoherent regime where the $2e^2/h$ plateau is suppressed to e^2/h. Further displacing the channel with more negative V_{wall} leads to traces where the $2e^2/h$ plateau is completely suppressed (red and green traces). These two conductance traces are bounded by regimes where $2e^2/h$ plateaus exist. On the leftmost trace, V_{wall} is less negative, and the conductance shows a "0.7" type feature near $(1-1.5)e^2/h$. The $1.5e^2/h$ feature is depressed as V_{wall} is set more negative, evolving to $\sim (0.5)e^2/h$. Another kink seems to develop around $(1.5)e^2/h$ when the initial $(1.5)e^2/h$ has become e^2/h (trace with pinchoff near -2.6 V). Eventually this second inflection starts to depress to e^2/h, and this process eventually ends with the $2e^2/h$ plateau suppressed. Note that the higher

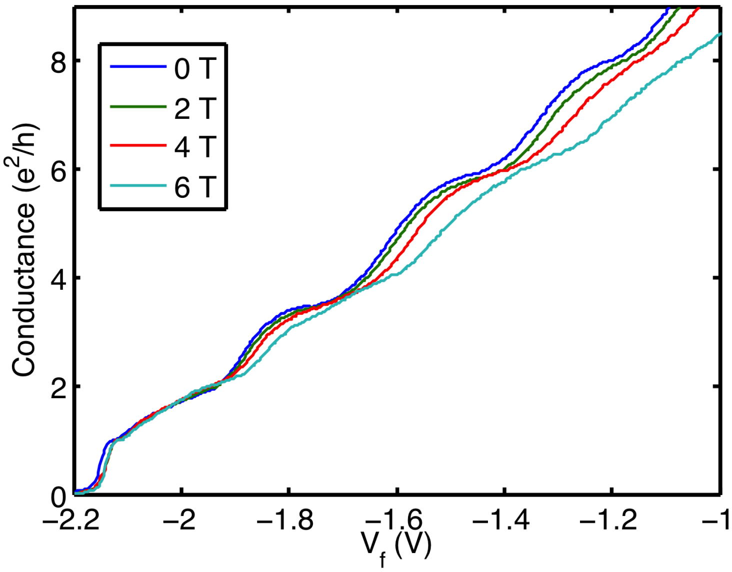

FIGURE 5.4: Dependence of the suppressed conductance in a field parallel to the 2DEG plane. The field is applied perpendicular to the current channel direction. The gate voltage on $V_{wall} = -1.93V$, and the traces are measured in the He dunker at 4.2 K.

index subband conductance values above $8e^2/h$ do not seem to be as affected, as was observed previously [45, 96].

A field parallel to the 2DEG (in y direction) at strengths up to 6 T was also measured, but no changes in the conductance were observable, Fig. 5.4. The field is applied parallel to the 2DEG plane to prevent cyclotron states from developing and is applied perpendicular to the current channel to couple to the subband quantization direction (y-axis). A series resistance that takes into account the change in the lead magnetoresistance is subtracted to obtain the traces. We see that at least up to 6 T, no dramatic change results; that is, the $2e^2/h$ plateau is not recovered in this situation. This suggests that the spins may already be polarized, which further supports our observation in Fig. 5.2.

A magnetic field perpendicular to the 2DEG plane, $B_\perp$, was also applied to study

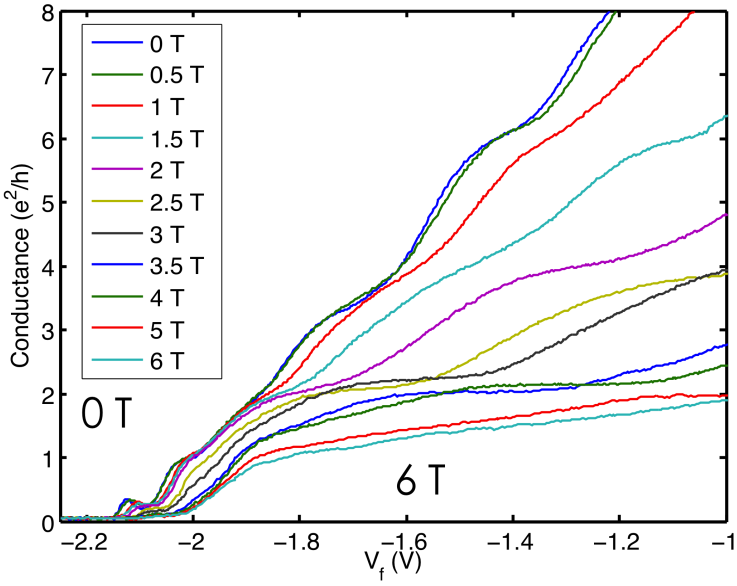

Figure 5.5: Evolution of suppressed $2e^2/h$ plateau in a magnetic field. Field strengths of 0, 0.5, 1, 1.5, 2, 2.5, 3, 3.5, 4, 5, 6 T were applied perpendicular to the 2DEG plane.

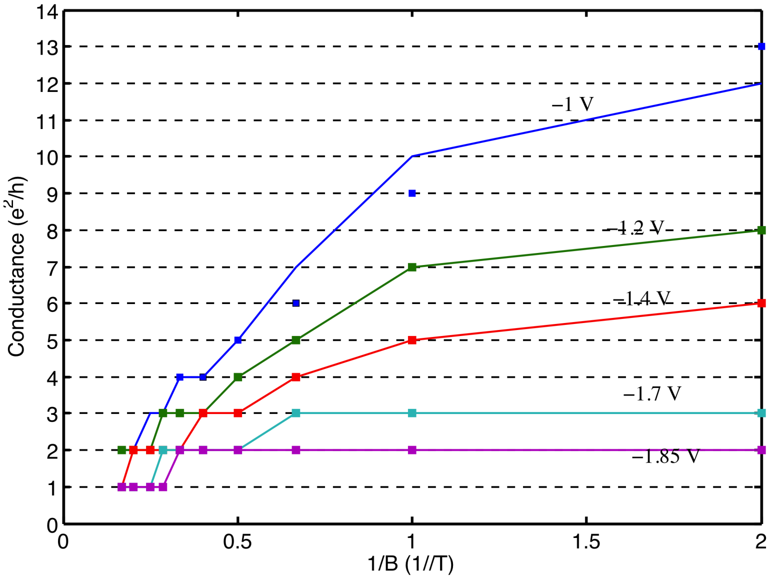

Figure 5.6: Number of subbands occupied versus 1/B for fixed gate voltages based on experimental data from Fig. 5.5.

the field dependence of the suppressed conductance regime, Fig. 5.5. The suppressed conductance under a perpendicular magnetic field is not affected up to 0.5 T, which provides a lower bound estimate of 5 K (taking the value at half the Landau gap). At 1 T, an inflection near $2e^2/h$ is noticeable, suggesting an upper bound of 10 K. This is a rather large energy scale. Beyond 3 T, the system enters the filling factor $\nu = 2$ quantum Hall regime (only the ground subband remains [12]), and a $2e^2/h$ plateau is clearly visible, which indicates that the cyclotron confinement has exceeded Coulomb energy. The suppression of $0.5e^2/h$ and e^2/h features in a field suggests it is not due to local resonances (as was suggested by Hew et al.), which should strengthen at stronger confinement in an applied $B_\perp$. At stronger fields, Zeeman energy begins to lift spin degeneracy, and signature of the Zeeman spin gap at e^2/h re-develops. It is important to note here that in comparison to Hew et. al., we do not observe a return of the $2e^2/h$ plateau until $\sim$ 1 T, whereas a transverse field of $B_z = 0.35$ T reestablishes the $2e^2/h$ plateau in their work. This is an important experimental clue pointing to the larger energy scale observed, which we believe is made possible by the asymmetric QPC geometry.

From magnetic subband depopulation, the density of the channel at $V_f = -1.85$ V (where $2e^2/h$ plateau should exist) is estimated to be $n_{1d} \sim 3.4 * 10^7$ /m. We provide some estimates based on both square well and parabolic potential in Table 5.1 and Table 5.2. Width estimates tend to be larger for square wells, as noted earlier in Ch. 1. We also estimate as an upper bound $n_{1D} \sim 6 * 10^7$ /m from $n_{2D} = 3.8 * 10^{15}$ /cm^2 and the inter-electron spacing, which satisfies $n_{1D} < 1/a_{Bohr}$. However, an additional condition is that the temperature should be bounded by the exchange J and Fermi energy, $J \ll T \ll EF$. We estimate $E_F/k_B \sim 19$ K and $J/k_B \sim 0.64$ K, which suggests that in principle no spin-incoherent behavior remains at 300 mK. This discrepancy is not understood but points to the important role an asymmetric geometry has in stabilizing the observed behavior.

Table 5.1: Magnetic Subband Depopulation Calculations with Square Well. Estimates are accurate to within hundredth digit.

Gate Voltage	k_F	Width	n_{2D}	n_{1D}
-1 V	1.7E8/m	223 nm	4.6E15/m^2	6.78E7/m
-1.2 V	1.5E8/m	170 nm	3.58E15/m^2	5.98E7/m
-1.4 V	1.33E8/m	150 nm	2.82E15/m^2	5.31E7/m
-1.7 V	1.08E8/m	95 nm	1.86E15/m^2	4.31E7/m
-1.85 V	9.8E7/m	60 nm	1.53E15/m^2	3.91E7/m

Table 5.2: Magnetic Subband Depopulation Calculations with Parabolic Well. Estimates are accurate to within hundredth digit.

Gate Voltage	k_F	Width	n_{2D}	n_{1D}
-1 V	1.45E8/m	385 nm	3.34E15/m^2	5.78E7/m
-1.2 V	1.3E8/m	264 nm	2.69E15/m^2	5.19E7/m
-1.4 V	1.27E8/m	140 nm	2.57E15/m^2	5.07E7/m
-1.7 V	9.6E7/m	106 nm	1.47E15/m^2	3.83E7/m
-1.85 V	8.5E7/m	93.5 nm	1.15E15/m^2	3.4E7/m

We can estimate the dimensionless parameter ν, Eq. 2.28, from these measurements. We find that the standard non-interacting quantized plateaus at even multiples of $2e^2/h$ tend to smear out at an applied DC bias of ~ 2.1 meV. Considering a parabolic confinement with equal subband spacings, we then extract the frequency of harmonic oscillations as $\Omega = 3.14 * 10^{12}$ /s. This allows for an estimate of r_0 and ν as shown in Table 5.3. Our estimate of $\nu = 1.32$ places the QPC directly within the allowed range for zigzag formation (see Ch. 2 Fig. 2.2). However, the rather small interaction strength, characterized by r_0/a_{Bohr} 4, seems to theoretically preclude a ferromagnetic state, and instead, places our wire well into the 4P state [55]. The exact behavior of 4P (four-particle) exchange processes is not well understood. However, if one imagines specific arrangements where interactions among odd numbered subsets of four interacting exchange electrons are slightly stronger, then it may be

Table 5.3: Rough estimates and calculations based on 1D density. The value of Ω (considering a parabolic well) is found by considering a subband energy of approximately $\hbar\Omega = 2.1$ meV. Equations in the last two rows from [55].

Estimate based on $n_{1D} =$	3E7/m	3.4E7/m	7E7/m
E_F/k_B	14.7 K	18.8 K	80 K
J/k_B	0.4 K	0.6 K	6.6 K
V_{coul}/k_B	38.2 K	43.3 K	89 K
$r_0 = (2e^2/4\pi\epsilon m\Omega^2)^{(1/3)}$	38.8 nm	38.8 nm	38.8 nm
$\nu = n_{1D} * r_0$	1.16	1.32	2.72

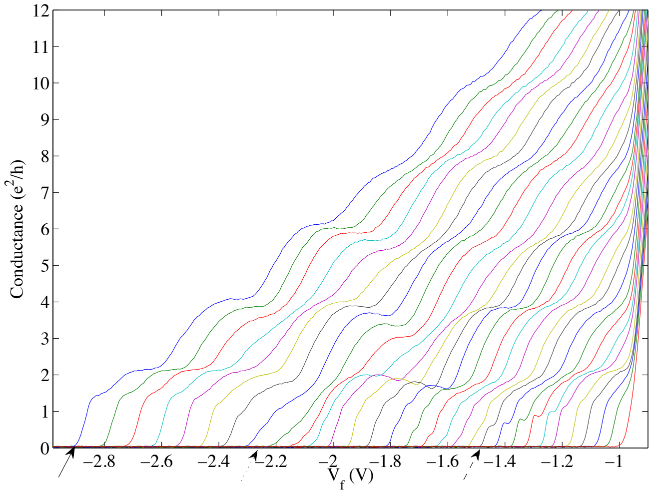

FIGURE 5.7: Conductance through W =300 nm T-QPC measured with V_{wall} set at fixed voltage from -1.5 V (leftmost trace) to -3.0 V (rightmost trace) in 50 mV decrements while sweeping V_f.

possible to have a polarized situation (this explains the existence of the M region in Fig. 2.2). Nonetheless, the observed behavior does not quite follow the predicted phase diagram, motivating further experimental and theoretical studies.

Next we present conductance traces from a separate cooldown, Fig. 5.7. The qualitative behavior is reproduced, but the feature near $(0.5)e^2/h$ is not as pronounced. The reason for this is not clear, but likely the different local charge configuration indirectly influences the relative strength of the spin modes. A numerical derivative of the conductance traces, dG/dV_f, is presented in Fig. 5.8. Flat regions in the derivative correspond to a conductance plateau, and peaks are from the riser between plateaus. The trace showing straight rise to $\sim 4e^2/h$ is marked with black arrow. Above and below this regime, several small distinct bumps below the $2e^2/h$ plateau can be seen, which is likely due to competition between the spin modes. Going from bottom to top, the plateau width and the number of available subbands decreases. Both trends indicate that the density is decreasing as we move from trace to trace, and confinement potential is becoming more shallow.

In Fig. 5.9, the differential conductance versus source-drain bias is shown for several asymmetric gate settings: (left panel) the $(1.5)e^2/h$ effect when $V_{wall} = -1.5$ V, (middle panel) spin-incoherent conductance with the $2e^2/h$ plateau suppressed to e^2/h and (right panel) row formation at $V_{wall} = -1.875$ V. The middle panel was taken during at a third cooldown, separate from the first two, explaining why the voltage values are slightly shifted. There is a weak plateau at e^2/h even at zero DC bias, in contrast to the right panel where there is clearly no bunching of the traces at zero source-drain bias. In both cases, there is no $2e^2/h$ plateau, in contrast to the left panel. At higher bias, there seems to be bunching of traces, signaling plateau formation, at $(0.5)e^2/h$ in all three panels. In the leftmost panel, the traces also more clearly bunch up around $3e^2/h$. In Fig. 5.10, I show a conductance regime with a $(0.5)e^2/h$ feature already at zero bias. This seems to be a rather different regime from all the others. These effects present more compelling evidence that we have tuned the point contact into regimes with unusual electron and spin correlations.

Temperature dependence of the conductance when the $2e^2/h$ plateau is fully suppressed is shown in Fig. 5.11. The quantized conductance of the $4e^2/h$ plateau is washed out by thermal averaging above 6 K; however, there still appears to be a clear feature below $\sim e^2/h$, which persists up to 10 K. At 18 K, the features near pinchoff are thermally smeared, but an inflection in the curvature near e^2/h can be

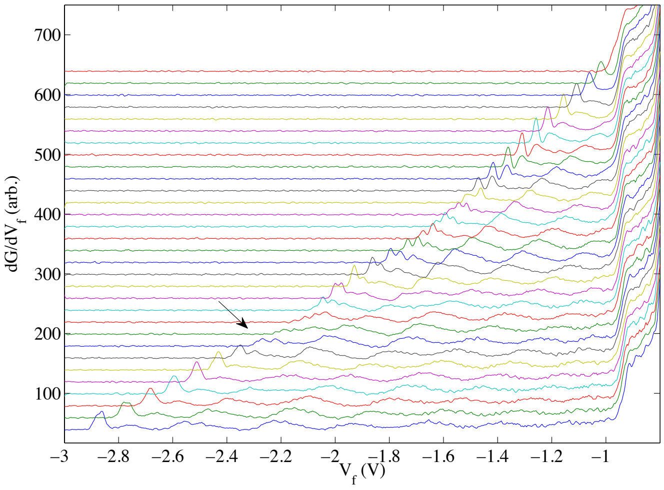

FIGURE 5.8: Numerical derivative, dG/dV_f, of conductance traces shown in Fig. 5.7. Traces are offset vertically for clarity, with bottom to top corresponding to those from left to right in Fig. 5.7.

discerned. This supports the high energy scale estimate of electron interactions in the conducting channel. Based on our estimate, the $2e^2/h$ plateau should return once the temperature exceeded $\sim 6 - 10$ K. Unfortunately, that is not observable as above 6 K conductance quantization is already thermally smeared. Nonetheless, the high bias and temperature results offer compelling evidence that we have tuned the point contact into regimes with unusual electron and spin correlations.

Recently, evidence for incipient lattice formation have been reported in the Coulomb blockade of carbon nanotubes [27], localization of double quantum wires [9, 8] and conductance of quantum wires [44, 45]. Similar to [44, 45], our experiment directly probes the conductance of the correlated state. Moreover, our large energy scale and unusual asymmetric geometry, which appears to enhance these correlation effects, leads to a stabilization of the Wigner Crystal even though the density of our 1D channel is higher.

In particular, the completely suppressed $2e^2/h$ regime is most clearly observed

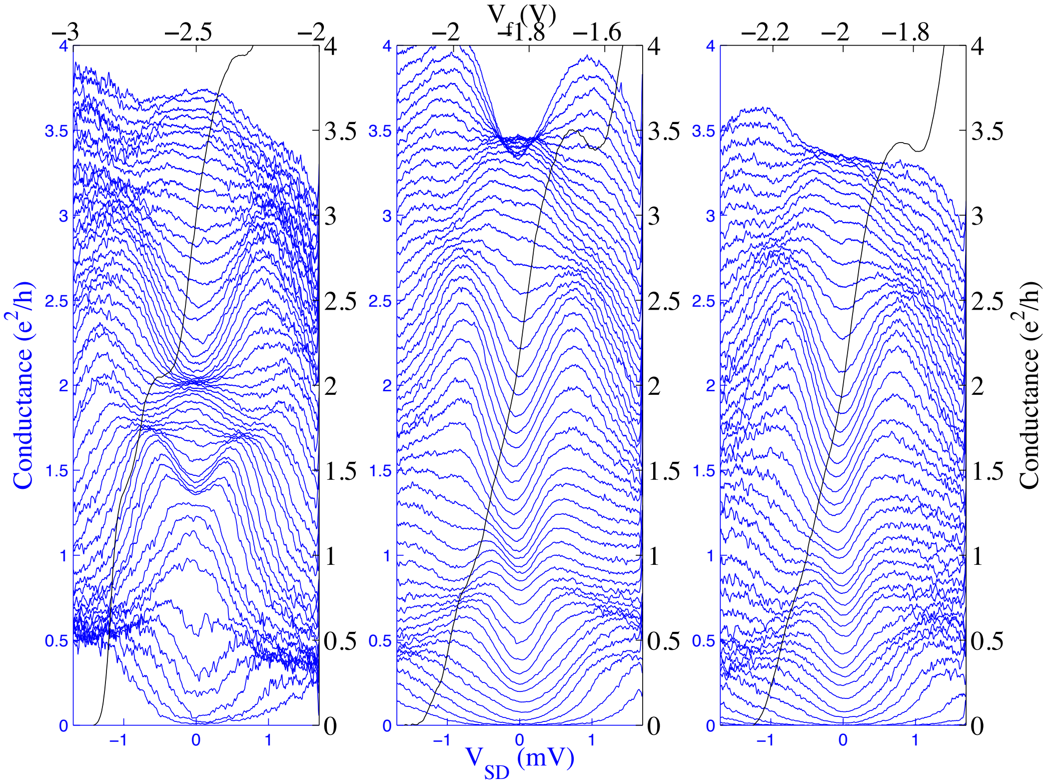

FIGURE 5.9: Differential conductance versus source-drain bias, V_{sd}. (left panel) $V_{wall} = -1.5V$ with clear $(1.5)e^2/h$ feature (lined arrow trace in Fig. 5.7), (middle panel) spin-incoherent regime (traces from separate cooldown, hence the shifted voltage values), (right panel) $V_{wall} = -1.875V$, direct jump to second subband.

in 300 nm gap samples. We observe the suppression regime in 250 nm gap samples with design as in Fig. 4.7, but at voltages very close to depletion (to the right in the asymmetrically biased traces). In 350 nm gap width samples and larger, no suppression behavior is observed. As was suggested, a shallower potential with less confinement is likely necessary to form zigzag rows, which give rise to the conductance behavior observed [45]. This suggests that for our 2DEG of depth 80 nm, a 300 nm gap is near optimal for forming the right potential shape to observe this strongly suppressed conductance. We note that the longer width of the quantization plateaus when V_{wall} is less negative suggests $\omega_y/\omega_x > 1$ (recall saddle-point potential). This

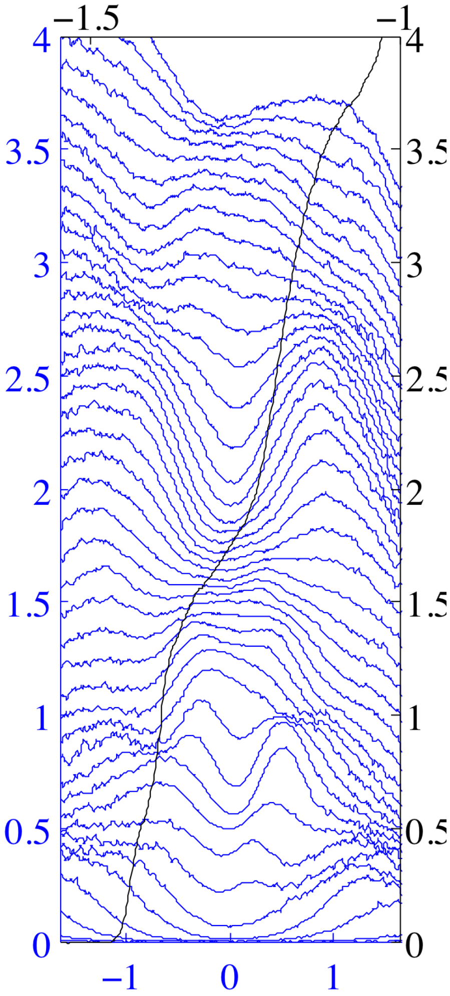

FIGURE 5.10: Differential conductance versus source-drain bias, V_{sd}, for $V_{wall} = -2.5V$. The conductance trace shows a feature at $(0.5)e^2/h$.

ratio decreases in the asymmetric geometries as V_{wall} is made more negative. A self-consistent potential calculation would provide additional insight into how the asymmetric geometry and gating influences the individual spin and charge modes and their coupling to the larger Fermi reservoirs, but that is beyond the scope of this paper.

From the data presented, it is clear that by tuning the gate voltages of highly asymmetric QPCs, a number of unusual conductance behaviors related to strong

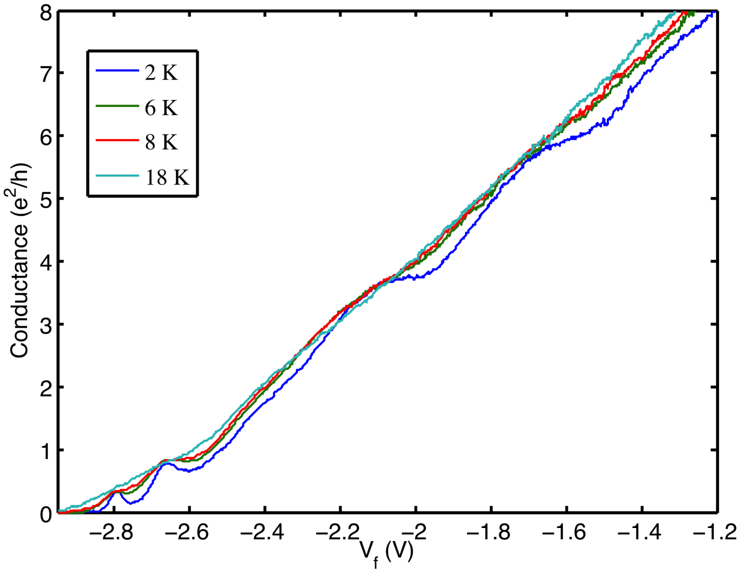

Figure 5.11: Temperature dependence of suppressed conductance trace in the suspected row formation regime. Conductance is measured at T = 2 K, 6 K, 8 K, 18 K.

interaction effects can be realized. In particular, a plateau at e^2/h related to a zigzag chain is believed to form. By optimizing the asymmetric geometry to a 300 nm gap in a crystal with 80 nm 2DEG depth, we observe unexpected suppression of the $2e^2/h$ plateau, suggesting highly unusual electron localization configurations in the channel. The large energy scale of the correlated behavior and the relatively high densities in our devices indicate the unusual effects an asymmetric geometry has in stabilizing the quantum state. These results suggest that studying how asymmetry, in design and gating, can give rise to unexpected interaction effects in 1D may help to point the way to understanding this strongly-correlated 1D electronic state.

6

Superconductivity in β-FeSe

6.1 Introduction

The discovery of superconductivity in La[$O_{1-x}F_x$]FeAs (x=0.05-0.12) with superconducting transition temperature Tc=26 K [52] was perhaps one of the most remarkable events in the physics community in year 2008. The initial discovery sparked a worldwide race similar to what occurred nearly twenty years ago with the copper oxide superconductors to find new Fe based materials with higher Tc. Reports of new superconducting compounds appeared almost weekly on the arXiv server with ever higher Tc. Currently, the highest Tc stands at 55 K in Sm[$O_{1-x}F_x$]FeAs [125], marking the Fe based superconductors as the only non-cuprate high temperature superconductors known to date.

I was fortunate to be part of the excitement as our collaboration with researchers at the Institute of Physics, Academia Sinica was responsible for discovering the superconducting β-FeSe compound[46]. Although Tc is $\sim$ 8 K as shown in Fig. 6.1, the crystal lattice structure of β-FeSe is by far the simplest of the Fe superconductors, consisting of only Fe and Se arranged in a layered tetrahedral conformation, Fig.

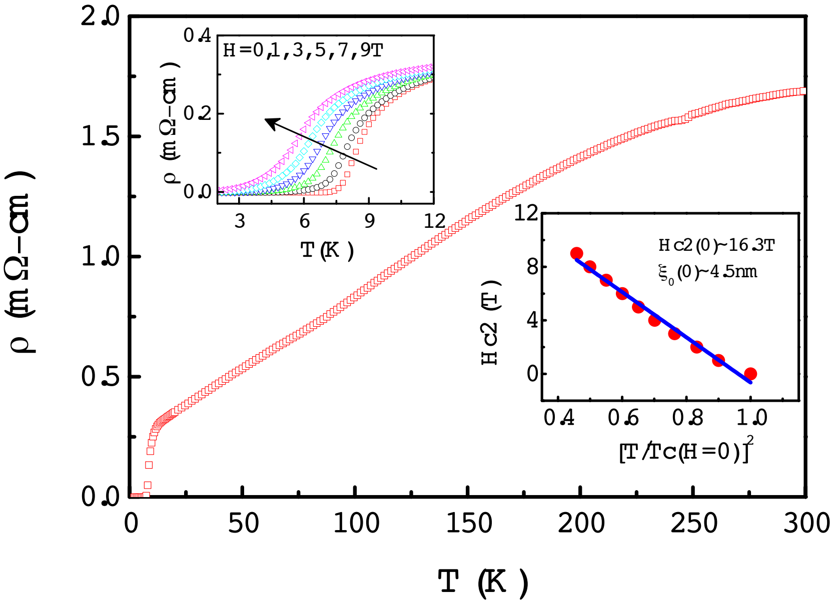

FIGURE 6.1: Resistivity of bulk β-FeSe. Field dependence shown in top left inset. The extracted critical field of $\sim$ 16.3 T and coherence length of 4.5 nm are shown in bottom right inset.

6.2. This simple structure would allow researchers to most easily discern the crucial mechanisms giving rise to superconductivity. Also of importance is the fact that Selenium has much less stringent safety requirements in the laboratory compared to the highly toxic As.

In the following, I will briefly detail the procedures for preparing polycrystalline and thinfilm FeSe samples. Then I will discuss results from Hall effect studies on FeSe.

6.2 Polycrystal Preparation

I am indebted to members of the Institute of Physics, Academia Sinica for sample growth. Samples used in the bulk Hall effect study were prepared by Dr. Fong Chi Hsu [46]. Polycrystalline bulk samples were prepared with the following procedure.

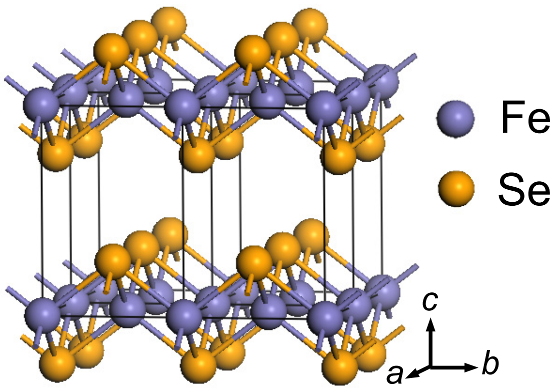

FIGURE 6.2: Tetragonal structure of FeSe. The superconductivity exists in the Fe layer (purple spheres).

High- purity (99%) powder of selenium and iron with appropriate stoichiometry ($FeSe_{1-x}$ with x = 0.03 - 0.18) were mixed and ground with an agate mortar and pestle. The grinding process was carried out in a fume hood with strong ventilation. The ground powder was cold-pressed into discs with 400 kg/cm^2 uniaxial stress. The discs were sealed in an evacuated quartz tube (to 10^{-5} torr vacuum) and slowly ramped to 700 °C, which is a little above the boiling point of Se, at the rate of 100°C/hr. Finally, the temperature was kept at 700°C for 24 hours. After cooling to room temperature at the rate of 300°C/hr, the loose sample was reground, pressed, sealed in a quartz tube, sintered again at 700°C for 24 hours, and finally annealed at 400°C for 36 hours. All of the samples were kept in vacuum dessicators before measurement.

Four terminal contacts for resistivity measurements were achieved by allowing Silver paste to dry on the bulk material surface. This method is sufficient to observe the superconducting transition; however, Hall signals are typically small, and in the Van der Pauw geometry the signals are even smaller, necessitating much better contacts with lower contact resistances. The small Hall signals are due to the fact that FeSe has densities in the range of typical semi-metallic type compounds, of order $10^{19} - 10^{21}$ cm^{-3}. This was crudely achieved by limiting by hand the amount of Silver paste applied to the sample surface, then gently heating the paste and bulk to coagulate the silver particles in the paste. Contacts were prepared in such a fashion on the four corners of square cut bulk material for Hall studies to be presented in 6.4. Standard Van der Pauw methodology was applied, but the measured signals were unfortunately still rather noisy, though sufficient to give the correct trend. There were two dominant factors contributing to the noise 1) intrinsic contact resistance from the heavy Fe oxidation layer 2) large measurement wire resistance. To obtain cleaner data, we decided to push for thinfilm samples measurements with a more sophisticated measurement contact methodology.

6.3 Pulsed Laser Deposition of Thinfilm

Here I briefly describe the pulsed laser deposition growth procedure for FeSeTe thin films used in Hall effect study. These films were prepared by Dr. Ji Yong Luo. A more detailed description of the thinfilms can be found in the review paper [121]. A description of the pulsed laser deposition system is discussed in A.

$FeSe_{1-x}Te_x$ thin films were deposited on a MgO substrate in a vacuum chamber (depositing pressure 10^{-5} torr) using a KrF (k = 248 nm) excimer laser (Lambda Physik LPX Pro) to bombard a sample target. The power density of the focused laser on the target is 56 J/cm^2, and the repetition rate is 2 Hz. To make targets, the starting materials of Fe, Se and Te powders were ground and pressed into disks with desired compositions of $FeSe_{1-x}Te_x$. Then, these disks were sintered in a vacuum furnace with temperature from 600 to 700°C. The final sizes of targets are roughly 1 inch (ϕ) x 8 mm(t) in size. The target substrate distance is approximately 50 mm. The substrate temperature during deposition is varied from 250 to 500°C. The deposition rate of thin film is about 0.5 $\AA$/shot. In addition, the surfaces of the targets were polished before each deposition to improve reproducibility.

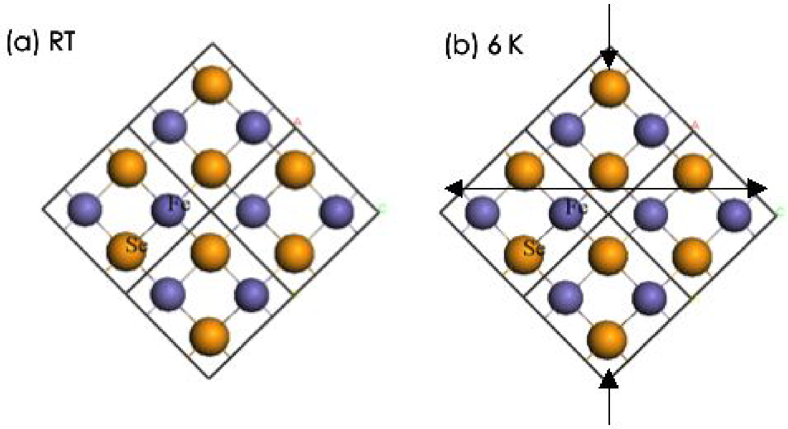

FIGURE 6.3: Top down view of FeSe structure. The Fe (purple) atoms sit on a plane. At low temperature, the lattice distorts so that the Fe planes become more two dimensional.

In contrast to the bulk material, a more careful approach was developed to contact to the thinfilms.

6.4 Hall Effect Measurements and Structural Transitions

One of the most interesting observations regarding FeSe is that the crystal structure undergoes a structural transition at ∼ 105 K from tetragonal to orthorhombic (or triclinic) symmetry (from x-ray diffraction data [46]). We believe this structural transition to be closely related to the origin of superconductivity in this class of materials.

Electrical transport studies seem to support this claim, although indirectly. From Hall effect measurements of bulk FeSe, Fig. 6.4, we find that FeSe is likely a two band superconductor, which suggests it is quite different from the cuprates, and that very unconventional superconducting mechanisms are at play. The two band nature is discerned from the temperature dependence of the Hall coefficient, which is positive for hole bands and negative for electron carriers. At high temperature, the Hall coefficient is positive. Around 100 K, the coefficient dips negative, indicative of electrons as the major carriers. However, at lower temperatures, the Hall coefficient rapidly turns positive again. We argue in the next few paragraphs that this low temperature behavior indirectly points to the importance of the structural change as a precursor to superconductivity.

A simple multi-band model for one hole and one electron can help to provide physical intuition. The Hall coefficient can be expressed as $R_H = \rho^2(n_h e^3 \tau_h^2/m_h^2 - n_e e^3 \tau_e^2/m_e^2)$, where ρ is the resistivity, e is unit of charge, and n_i, m_i, τ_i, are the carrier density, effective mass, and carrier scattering time of band i (i=electron or hole), respectively. The dominant temperature dependence typically comes from the resistivity, which was found to vary slowly with temperature in the normal state [17]. In addition, the carrier density and effective mass are in general fixed regardless of temperature. We conclude that the rapid rise in Hall coefficient observed arises predominantly from the strong temperature dependence of the relaxation times, τ_h and τ_e. Specifically, τ_h must increase much faster than τ_e.

Increases in the carrier scattering time, or time between scattering events, are expected as the temperature drops. Typically, scattering occurs off of either phonons or magnetic moments. Interestingly, despite the excess of Fe, no magnetic ordering is observed at low temperatures in FeSe [121]. This suggests that scattering events due to Fe magnetic moment are relatively constant from high to low temperature. This implies that the large increase in τ_h is likely due to a suppression in phonon scattering. Such an effect could arise when the crystal lattice undergoes a distortion. This argument seems to be consistent with the diffraction data showing the widened γ angle, which suggests the Fe layer has become more two dimensional. The initial bulk results have been clarified and corroborated by much cleaner work on thin films, Fig. 6.5 [17].

In conclusion, the experimental evidence from electrical transport and x-ray diffraction methods clearly points to the important role the low temperature struc-

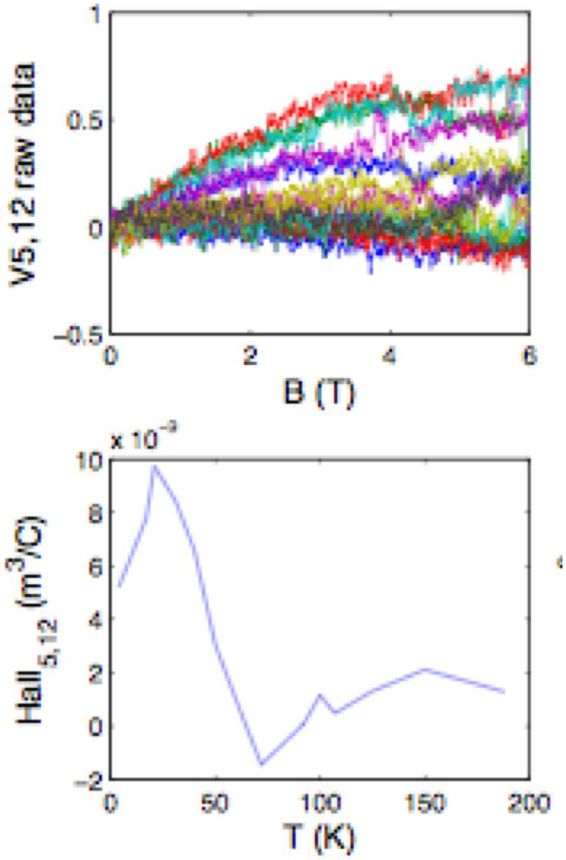

FIGURE 6.4: (a) Measured Hall signal raw data as function of field. (b) Temperature dependence of Hall coefficient for bulk FeSe.

tural change plays in FeSe. Preliminary studies suggest that this behavior is generally true across the Fe based superconductor family as a whole.

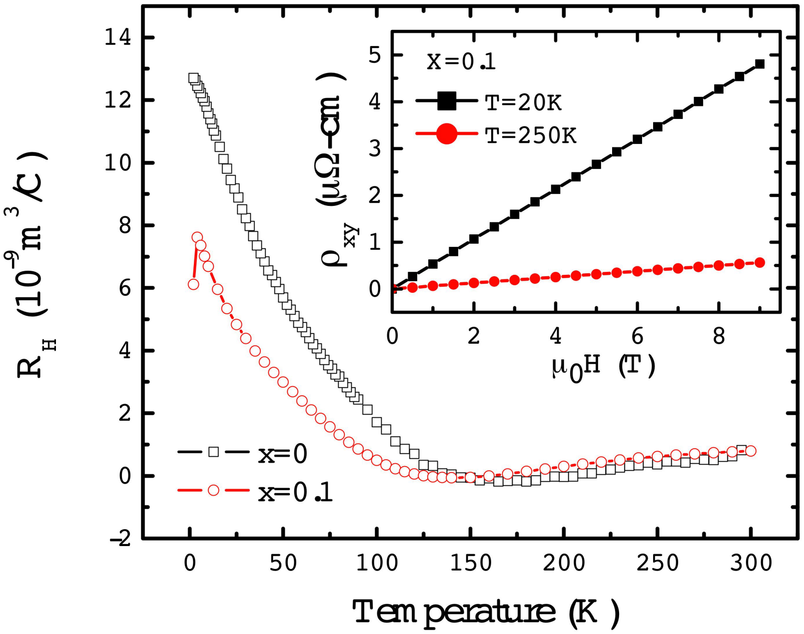

FIGURE 6.5: The temperature dependence of Hall coefficient for $FeSe_{1-x}Te_x$ films, x=0, 0.1. The inset shows the Hall resistivity as a function of magnetic field.

7

Conclusion

This thesis presents experimental transport data from asymmetric quantum point contacts. The asymmetric designs, which have been largely overlooked by the research community, can provide a wealth of novel transport behavior, and deserves our attention. A strongly suppressed $2e^2/h$ conductance plateau to e^2/h is observed in these asymmetric QPCs, which is a predicted theoretical property of a spin-incoherent Luttinger liquid. Furthermore, traces with direct drops of the conductance from $\sim 4e^2/h$ to pinchoff with no other anomalous features are observed. Although the theory does not predict such behavior, we believe this conductance behavior to be correlated with the formation of parallel conduction rows in the quantum point contact. Differential conductance versus DC source-drain bias measurements further show signatures of a strongly correlated 1D Wigner crystal. To our knowledge, this is only the second observation of a quantum Wigner crystal of any form to date.

There are still many unanswered questions however. The most obvious is why an asymmetric geometry gives rise to such unusual transport behavior. For instance, in the theory of Matveev, the issue of asymmetry in the confinement does not appear

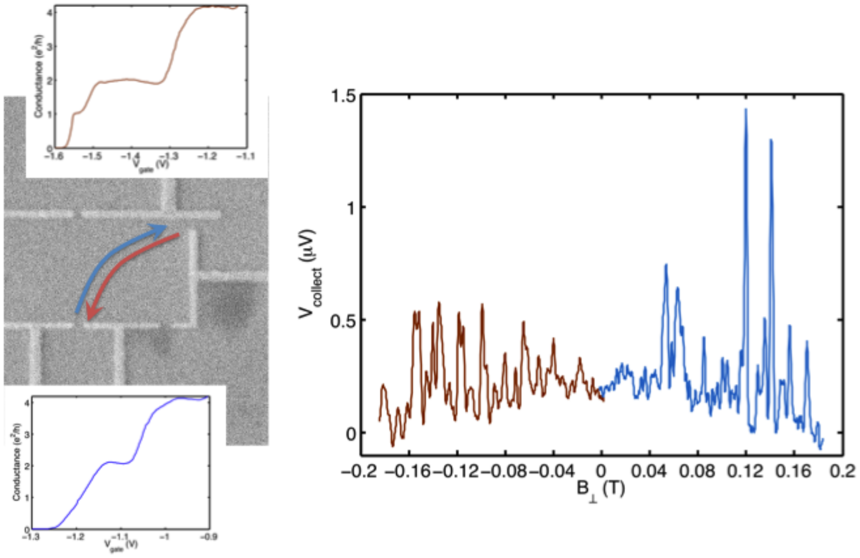

Figure 7.1: Coherent electron focusing in asymmetrical QPCs. The image on the left shows the two point contacts used for the focusing measurement. The asymmetric QPC is tuned to the e^2/h kink, while the symmetric QPC is tuned to the first quantization plateau at $2e^2/h$. The collector voltage versus perpendicular magnetic field is presented on the right.

at first glance to be relevant. Furthermore, why is there an optimal gap width for observing the spin-incoherent and Wigner crystal behavior? To properly address these questions, we require help from our friends on the theoretical side in simulating self-consistently the precise potential shape in the 2DEG.

In addition to these interesting questions, the asymmetric gate design can serve as a model system for a variety of other transport measurements. For example, consider the coherent electron focusing measurement performed in Fig. 7.1. Electron focusing with 2DEG QPCs was first studied in [107]. The long mean free path of the electron allows for the ability to coherently focus a beam of electrons injected out of a QPC into a second QPC collector. The beam of electrons focused into the collector creates a measurable chemical potential difference across the collection QPC, which can be measured as a voltage drop. The focusing is achieved by applying a magnetic field perpendicular to the plane of the 2DEG. The Lorentz force from the applied field

$qv \times B$, where q is electron charge, v is the electron velocity, bends the motion of the electrons that are injected out of a QPC. The cyclotron orbit has a radius $r = mv/qB$.

In Fig. 7.1, if we look at the positive field scans, which corresponds to injecting electrons out of the symmetric QPC into the asymmetric QPC, we can discern a periodicity of ~ 60 mT, which corresponds to a focusing radius of $\sim 3\mu$m. This is the dominant focusing beam which goes directly from injector to collector without any specular reflections. However, quite unusually, instead of a single peak, sharp double peaks are observed, along with many small peaks. Also quite interesting is the behavior in the reverse direction. Here, the negative field trace corresponds to situations where the electrons are injected out of the asymmetric qpc and collected in the symmetric one. No large periodicity corresponding to a focusing radius is observed, instead, we have a uniform period of ~ 20 mT. This is currently not well understood, though one wonders whether this is related to scattering off unusual incipient lattice structure formed in the asymmetric point contact.

In Ch. 6, we presented Hall Effect measurements on the β-FeSe superconductor. We observed a sharp increase in the Hall coefficient at low temperatures, which we speculate to be due to a suppression in phonon scattering. Such an effect could arise when the crystal lattice undergoes a distortion. This argument seems to be consistent with the diffraction data showing the widened γ angle, which suggests the Fe layer has become more two dimensional.

The hypothesis that the structural distortion is critical for superconductivity in FeSe may turn out to be true more generally for the Fe based superconductors as a whole. Preliminary studies seem to support this conjecture. However, there are still many issues to understand. The FeSe superconductors do not have any magnetic ordering, in contrast to some of the FeAs based materials. On the other hand, spin fluctuations are known to exist in FeSe, and may be important for the superconductivity. What is not understood is whether the structural distortion gives rise to spin fluctuations, and then superconductivity? Or is there a completely different causal relation? Understanding these issues will greatly enhance our understanding of the Fe based superconductors, as well as the high temperature superconductor family as a whole.

Appendix A

Nano Certificate: Superconducting Thin Film Fabrication and Measurements

A.1 Introduction

Recently, advances have been made in engineering strong flux pinning nanocomposite superconducting thin films that at 65 K have 5 times stronger vortex pinning force than NbTi at 4.2 K [36]. NbTi is the typical material used to fabricate high field magnets, but with the disadvantage in that the magnets can only be operated at liquid helium temperatures. Nanocomposite superconducting materials potentially could provide more versatile and higher operating temperature high field applications.

In order to study these materials, a collaboration was formed between the groups of Prof. Albert Chang at Duke University, and Prof. Maw-Kuen Wu at the Institute of Physics, Academia Sinica, Taiwan. Prof. Wu's group helped grow various superconducting thin film crystals to be measured with a scanning hall probe system in Prof. Chang's group.

The superconducting thin films were grown in a pulsed laser deposition (PLD) chamber during my trip to Taiwan in early June 2007. Two types of crystal based on the well known $YBa_2Cu_3O_{7-\delta}$ (YBCO) family of type II high-T_c superconductors were grown during this trip: 1) pure YBCO superconductor thin film with the 123 structure, and 2) YBCO thin film crystal with CeO nanoparticle impurities, forming a 123-211 structure [39, 40].

A.2 Sample Fabrication

In this section I will detail the PLD sample fabrication procedure. Figure A.1 shows a schematic of the PLD system. In PLD, a pulsed laser bombards a target sample, situated in a chamber that is either in vacuum or in the presence of a background gas. The laser beam vaporizes the target, and the ejected vapour forms a bright plume or plasma that is directed towards the substrate. The target material is deposited as a thin film onto the substrate. Typically the substrate is heated so that the deposited material remains in molten form, and gradually solidifies during the ramp down/cooling process.

For YBCO thin films, the sample chamber was first pumped to vacuum and then 300 mbar of O_2 was introduced and maintained. Oxygenation was required for the growth of oxide superconductors. The substrate was glued with silver paste to the heater, which was heated to roughly 900 degrees Celsius. As the ramp speed was very slow, the heating process took roughly an hour and half. Substrates used were $SrTiO_3$ and MgO. The target was a bulk puck of the desired material. These were grown with a separate process in the lab with high temperature furnaces. A 238 nm wavelength excimer laser, using Kr, Neon, F gases, was pulsed at 4 kHz with 130 mW power; the laser beam spot of roughly mm in size was scanned in a 10 mm by 5 mm rectangle centered at the target surface's center so as to obtain the most homogeneous emission of material. Experience from several group members indicated that roughly 200 nm thick film was deposited over half an hour's time. Unfortunately, the PLD system currently does not contain any energy electron diffraction detectors, such as

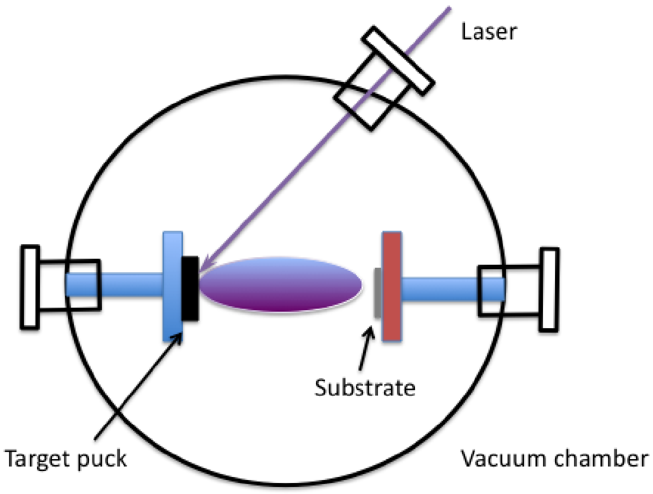

FIGURE A.1: Schematic of the pulsed laser deposition system. The target puck is irradiated with laser pulses, which generate a plasma beam that deposits onto the sample substrate. The substrate stage can be heated.

RHEED, for discerning the exact film thickness during growth.

After the film was deposited, the laser pulse was stopped, and the substrate temperature allowed to gradually cool to room temperature. The substrate would then be removed from the chamber and DC four terminal resistivity measurements performed to ensure the crystal's integrity.

Figures A.2 and A.3 are photos of the PLD system in Prof. Wu's lab at IOP, Academia Sinica.

A.3 Measurements

Below are four terminal resistance versus temperature measurements for three samples, one pure YBCO on $SrTiO_3$ substrate and two YBCO with impurities, on different substrates, $SrTiO_3$ and MgO. Measurements were performed on a physical property measurement system (PPMS) from Quantum Design, see Figure A.4, as well as using the simple dipstick method. Observing a superconducting transition from the four terminal resistivity measurement essentially validated the crystal growth,

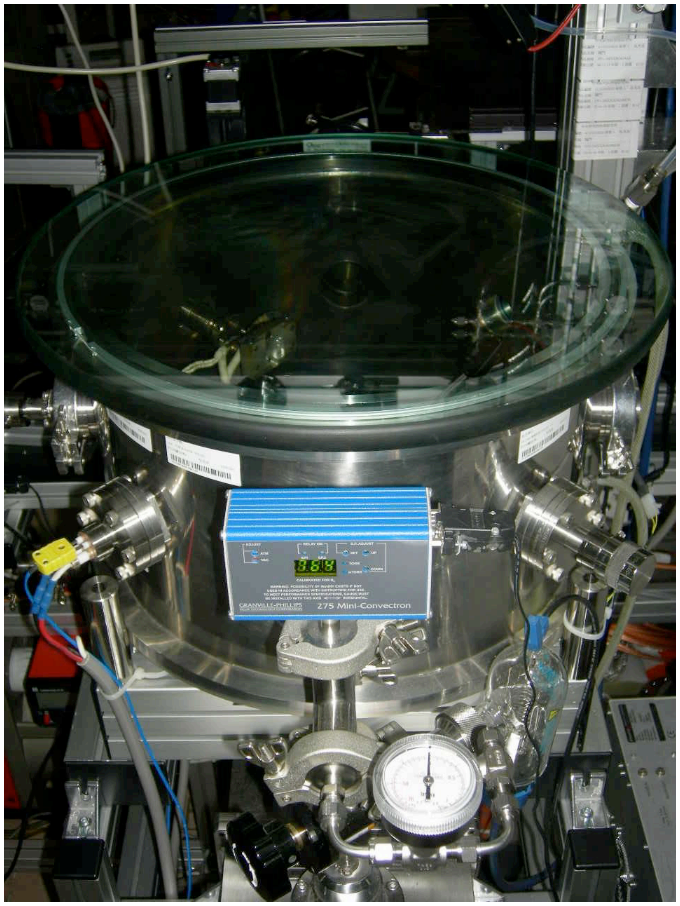

FIGURE A.2: Front side photo of the pulsed laser deposition equipment, showing the deposition chamber and vacuum gauges.

although, for the impurity samples, the success in adding CeO to improve pinning strength must wait to be seen.

I would like to thank Profs. Chang and Wu for allowing me the opportunity to participate in this project. I would also like to thank Dr. Chi-Yung Luo and Chun-Te Wu for their assistance in sample fabrication.

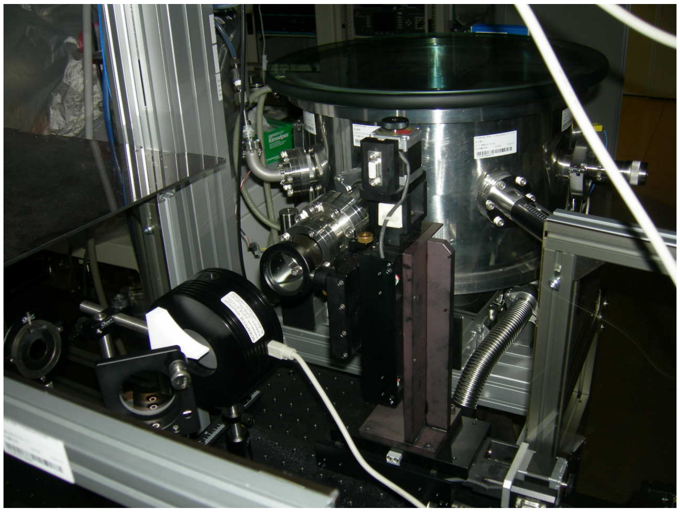

Figure A.3: Back side photo of the pulsed laser deposition equipment. Here we can see the laser entry port, currently blocked by a power meter.

Figure A.4: Physical property measurement system from Quantum Design, capable of measuring DC resistivity or electro-transport, magnetometry (for example, AC susceptibility), thermal transport, and heat capacity.

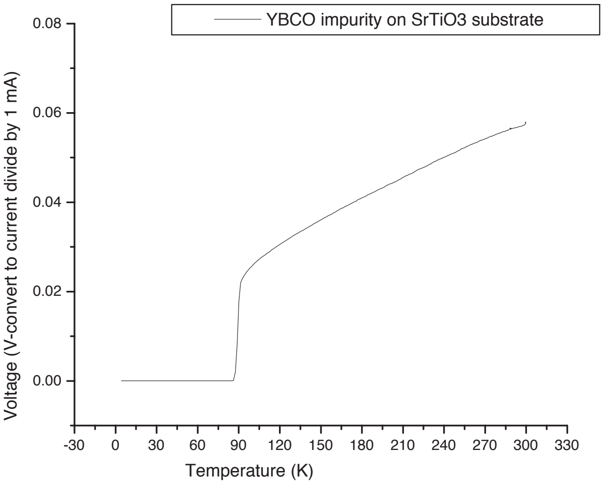

Figure A.5: YBCO 123-211 with CeO_2 (hopefully) nanoparticles on $SrTiO_3$ substrate. $T_c = 88$ K with sharp transition width.

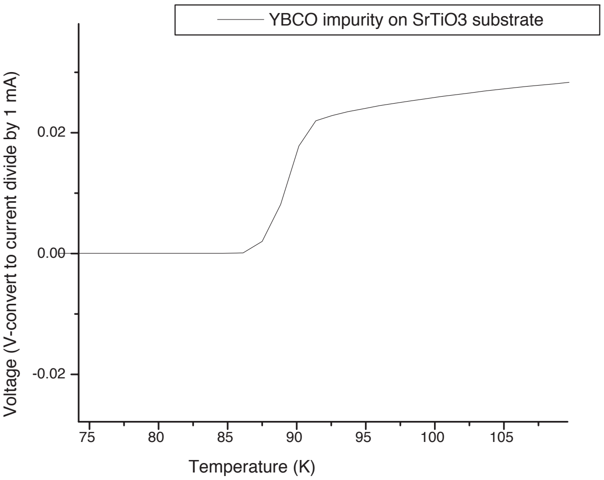

Figure A.6: Close up view of Figure A.5.

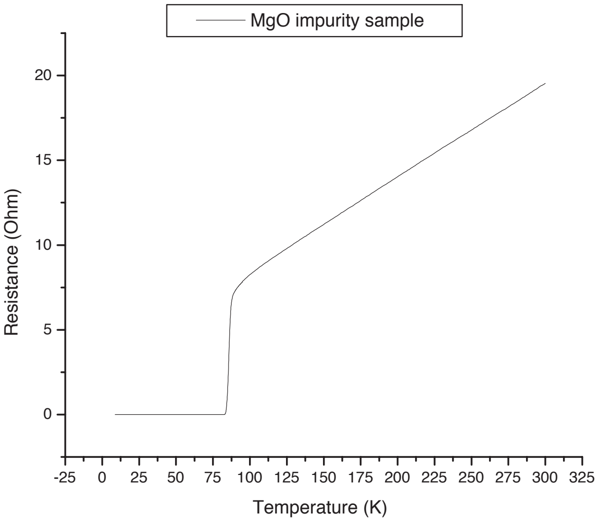

FIGURE A.7: YBCO 123-211 with CeO_2 (hopefully) nanoparticles on MgO substrate. T_c roughly 85 K with large approximately 2 K transition width.

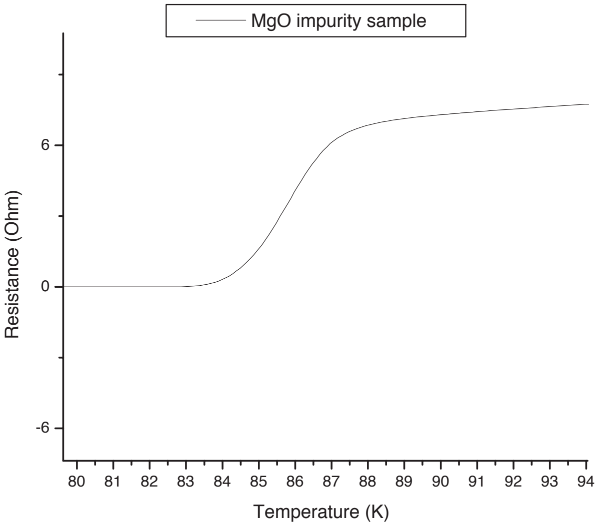

FIGURE A.8: Blow up of transition for Figure A.7.

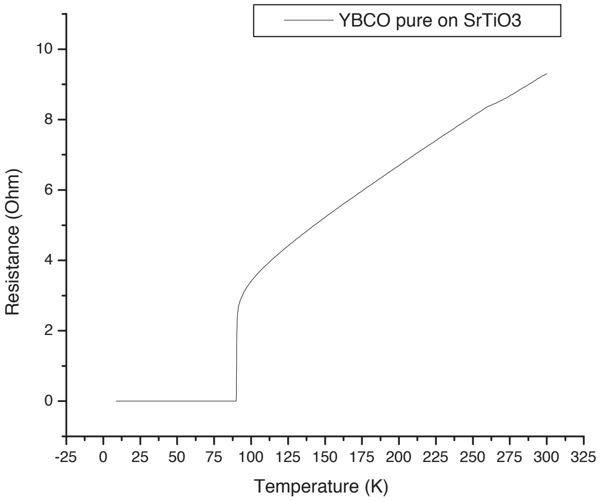

Figure A.9: Pure YBCO on SrTiO$_3$ substrate. T$_c$ = 90 K with sharp transition.

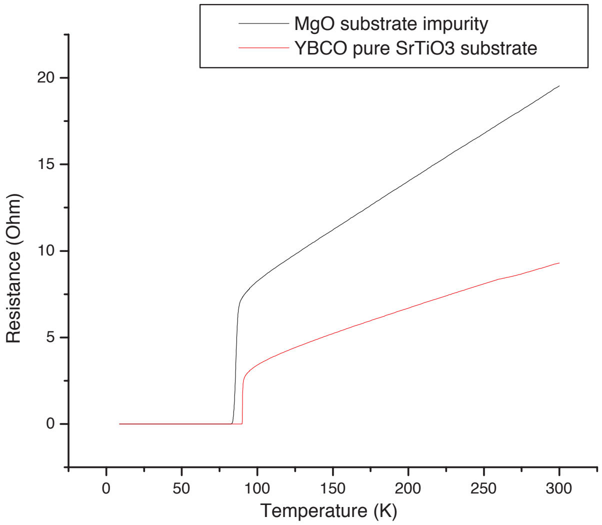

Figure A.10: Plot of Impurity sample with pure YBCO sample. Impurity samples decrease T$_c$ slightly by 2 to 5%.

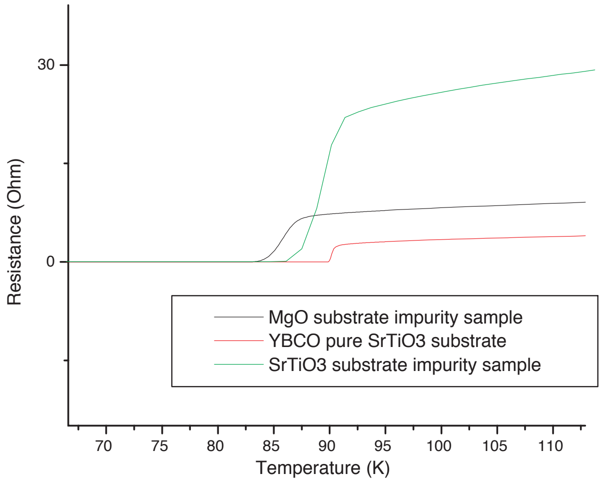

Figure A.11: Close up plot of Impurity samples with pure YBCO sample.

Appendix B

Additional Fabrication Techniques

I discuss two additional and useful nanolithography fabrication techniques. Although these methods were not used in the main device under study in this thesis, I have utilized these methods to create GaAs quantum dots and Aluminum double tunneling barrier single electron transistors.

B.0.1 PMMA Overexposure

PMMA can crosslink and become hardened by an excessive bombardment of electrons (typically at doses larger than a mC/cm^3)[41], which allows the resist to be used as an insulating spacer layer. This is an additional tool to develop more complicated structures. However, the PMMA exposure step must be done separate from the actual device exposure, so the drawback is that additional lithography steps are required in the fabrication process. Adding extra lithography steps is nontrivial as each successive ebeam write must be properly aligned to the first. But this can be done by creating alignment marks.

The fabrication procedures for devices with overexposed PMMA are as follows. First, a sample with Cr/Au or Ti/Au alignment marks is prepared. This is done with standard ebeam lithography steps. Au alignment marks are necessary as only Au provides enough contrast to be visible beneath the PMMA layer. This step can be skipped if the device alignment requirements are not as stringent. Then PMMA is spin coated onto the sample surface and baked to harden in the usual way to achieve a PMMA thickness of 100-200nm. Prior to actual ebeam exposure, the sample edges are imaged using the viewing crosshair, for example the bottom two corners and the top right corner, to get a rough location bearing of the center of the ebeam write pattern. Then I overexpose the PMMA in the shape, size and location that I want. A large beam current, as well as long dwell times are needed to achieve the overexposure. I have found that for 1000 magnification (200x200 μm^2 lithographic design), a 500pA beam current and 50 μs to 100 μs dwell time is required to overexpose PMMA. The sample is then developed in MIBK:IPA for 30s, followed by an immediate acetone ultrasonic rinse to remove the unexposed PMMA. I found that it takes three to four ultrasonic acetone washes of 10 minutes each before the overexposed PMMA starts to loosen. Subsequently, a new layer of PMMA is spun onto the sample, and the actual device is written at the required location by following the sample edge distances as rough measure, and alignment marks for fine tuning. It is important to also match the sample rotation as precisely as possible.

Fig. B.1 is an image of a Cr/Au top gate raised by overexposed PMMA (black rectangular region). The Cr/Au gate must be raised so that the underlying 2DEG is not depleted by the applied negative gate voltage. Effectively, the PMMA region increases the capacitive coupling, so that a larger voltage would be needed to fully repel all the electrons underneath the raised region. A potential problem is that the Cr/Au gate may not be properly connected if the PMMA layer is too high. However, as shown in Fig. B.2, this is not the case with the above parameters.

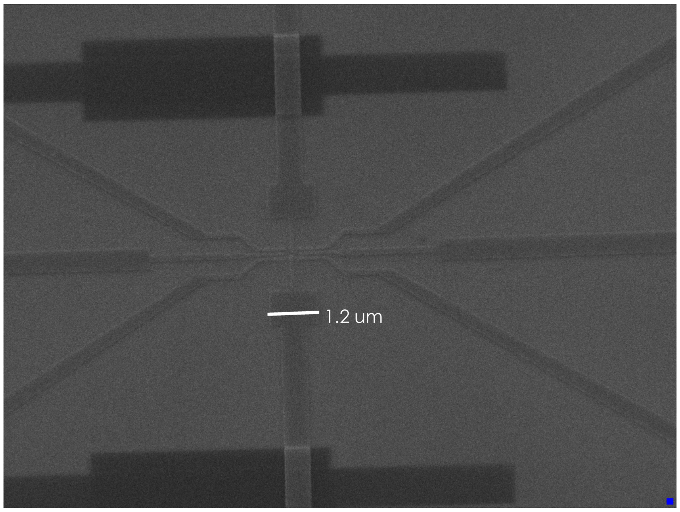

Figure B.1: PMMA overexposure to create a raised layer on either side of the parallel coupled double quantum dot. This allows the source-drain of both quantum dots to be tied together.

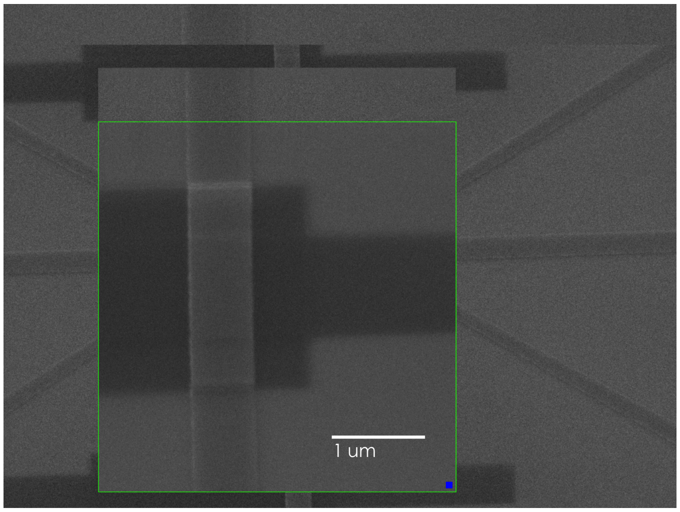

Figure B.2: A more detailed look of the previous figure, showing that the gate is connected with no breaks developing due to the raised PMMA.

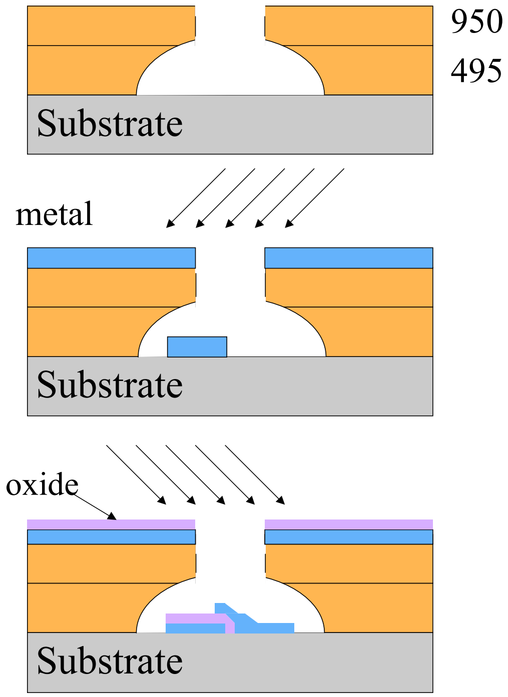

FIGURE B.3: PMMA with differing molecular weight are coated onto the sample surface to create a double layered mask. A single ebeam write completes the mask patterning. Metal is then deposited first from the right at an angle (which direction first is arbitrary). Oxygen is next introduced to form the insulating oxide layer. Finally, metal is deposited at an angle 180° from the first to form a complete junction.

B.0.2 Double Angle Evaporation

The double angle or "shadow" evaporation technique was first demonstrated by Dolan and Fulton[29, 33]. This technique was developed for the study of small Josephson tunnel junctions. Our method, which was worked out by Limin Cao, is somewhat simpler than Dolan's original technique. The technique is illustrated in Fig. B.3. First, instead of a single layer of ebeam resist, two layers of PMMA with differing molecular weight are used. We utilize 495 PMMA 8% for the bottom layer,

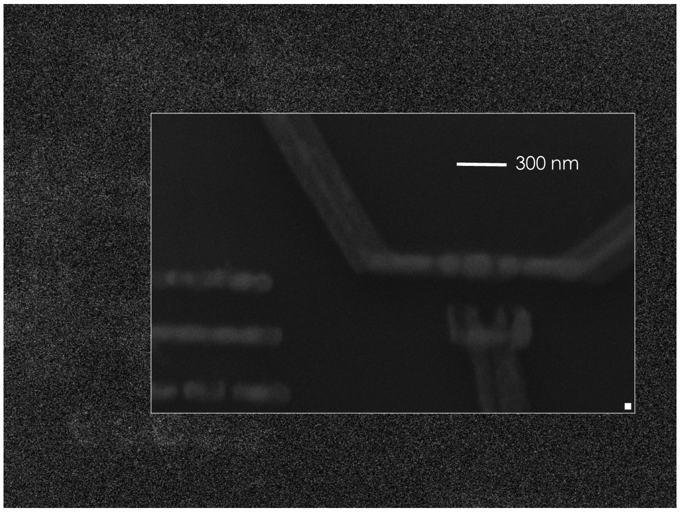

Figure B.4: This is a two junction single electron transistor (SET). The junctions are Al/AlO$_x$/Al, fabricated following the technique described in the text.

and 950 PMMA 8% for the top. As the response of the 495 and 950 PMMA to ebeam is different, a large undercut of the bottom layer (495) with a narrower opening at the top layer (950) can be achieved in a single ebeam write and developer wash (40s in MIBK:IPA for these devices). This sets up the mask for the angled metal evaporation. Typically, metal deposition is oriented normal to the sample surface; instead, we deposit the metal at an angle to provide an offset. To create the oxide barrier, the sample is then exposed to oxygen (this requires breaking the vacuum in our evaporator, typically I inject into the chamber oxygen to 100 millitorr pressure then hold for 10 minutes before pumping it out). The oxide thickness should be within several nanometers. Finally, the second layer of metal is deposited at an angle 180° from the first. The end product of this process is a metal/insulator/metal or superconductor/insulator/superconductor type junction.

An Al double junction transistor is shown in Fig. B.4. The two round circles are the junctions to the larger block in the middle, the central charge island. The angled evaporation is done from left and right, and a clear overlap region is observable. A

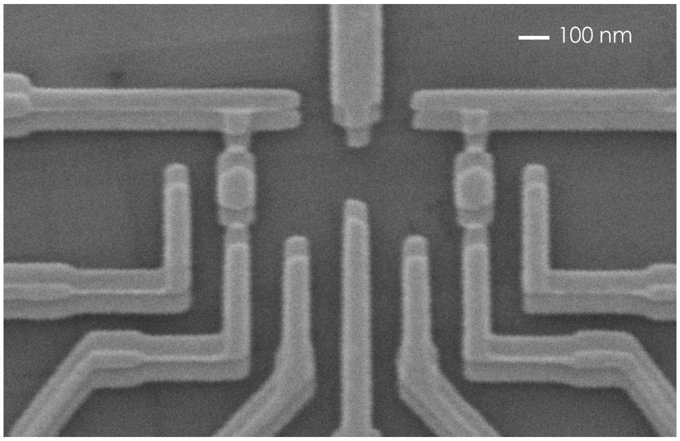

Figure B.5: This design consists of two series coupled quantum dots, each with its own Al-SET detector. The width of the gates at the tips are designed to be 100 nm.

more complicated double quantum dot each with an Al-SET is shown in Fig. B.5. Here the evaporation is done top and bottom.

Bibliography

[1] RL ANDERSON. Germanium-gallium arsenide heterojunctions, 1960. Ibm Journal of Research and Development.

[2] T ANDO. Theory of quantum transport in a 2-dimensional electron-system under magnetic-fields .2. single-site approximation under strong fields. *Journal of the Physical Society of Japan*, 36(6):1521–1529, 1974.

[3] T ANDO. Theory of quantum transport in a 2-dimensional electron-system under magnetic-fields .3. many-site approximation. *Journal of the Physical Society of Japan*, 37(3):622–630, 1974.

[4] T ANDO. Theory of quantum transport in a 2-dimensional electron-system under magnetic-fields .4. oscillatory conductivity. *Journal of the Physical Society of Japan*, 37(5):1233–1237, 1974.

[5] T ANDO and S MORI. Effective-mass theory of semiconductor heterojunctions and super-lattices. *Surface Science*, 113(1-3):124–130, 1982.

[6] T ANDO and Y UEMURA. Theory of quantum transport in a 2-dimensional electron-system under magnetic-fields .1. characteristics of level broadening and transport under strong fields. *Journal of the Physical Society of Japan*, 36(4):959–967, 1974.

[7] N. W. Ashcroft and N. D. Mermin. *Solid State Physics*. Holt, Rinehart and Winston, New York, 1976.

[8] OM Auslaender, H Steinberg, A Yacoby, Y Tserkovnyak, BI Halperin, KW Baldwin, LN Pfeiffer, and KW West. Spin-charge separation and localization in one dimension. *Science*, 308(5718):88–92, April 2005.

[9] OM Auslaender, A Yacoby, R de Picciotto, KW Baldwin, LN Pfeiffer, and KW West. Tunneling spectroscopy of them elementary excitations in a one-dimensional wire. *Science*, 295(5556):825–828, February 2002.

[10] PF BAGWELL and TP ORLANDO. Landauer conductance formula and its generalization to finite voltages. *Physical Review B*, 40(3):1456–1464, July 1989.

[11] CWJ BEENAKKER and H VANHOUTEN. Quantum transport in semiconductor nanostructures. *Solid State Physics-Advances In Research and Applications*, 44:1–228, 1991.

[12] KF BERGGREN, TJ THORNTON, DJ NEWSON, and M PEPPER. Magnetic depopulation of 1d subbands in a narrow 2d electron-gas in a gaas-algaas heterojunction. *Physical Review Letters*, 57(14):1769–1772, October 1986.

[13] G Burkard, D Loss, and DP DiVincenzo. Coupled quantum dots as quantum gates. *Physical Review B*, 59(3):2070–2078, January 1999.

[14] M BUTTIKER. 4-terminal phase-coherent conductance. *Physical Review Letters*, 57(14):1761–1764, October 1986.

[15] M BUTTIKER. Quantized transmission of a saddle-point constriction. *Physical Review B*, 41(11):7906–7909, April 1990.

[16] AM Chang. Chiral luttinger liquids at the fractional quantum hall edge. *Reviews of Modern Physics*, 75(4):1449–1505, October 2003.

[17] H. H. Chang, J. Y. Luo, C. T. Wu, F. C. Hsu, T. K. Chen, P. M. Wu, M. K. Wu, and M. J. Wang. *Te substitution effect on electronic properties of b-FeSe thin films*, volume In Press. Physica C, 2009.

[18] J. C. Chen, Yiping Lin, Kuan Ting Lin, T. Ueda, and S. Komiyama. Effects of impurity scattering on the quantized conductance of a quasi-one-dimensional quantum wire. *Applied Physics Letters*, 94(1), January 2009.

[19] MH CHEN, W POROD, and DJ KIRKNER. Coupled finite-element boundary-element method for semiconductor quantum devices with exposed surfaces. *Journal of Applied Physics*, 75(5):2545–2554, March 1994.

[20] T. M. Chen, A. C. Graham, M. Pepper, I. Farrer, and D. A. Ritchie. Bias-controlled spin polarization in quantum wires. *Applied Physics Letters*, 93(3):032102, July 2008.

[21] T. M. Chen, A. C. Graham, M. Pepper, I. Farrer, and D. A. Ritchie. Non-kondo zero-bias anomaly in quantum wires. *Physical Review B*, 79(15):153303, April 2009.

[22] T. M. Chen, A. C. Graham, M. Pepper, F. Sfigakis, I. Farrer, and D. A. Ritchie. Odd-even spin effects and variation of g factor in a quasi-one-dimensional subband. *Physical Review B*, 79(8):081301, February 2009.

[23] SM Cronenwett, HJ Lynch, D Goldhaber-Gordon, LP Kouwenhoven, CM Marcus, K Hirose, NS Wingreen, and V Umansky. Low-temperature fate of the 0.7 structure in a point contact: A kondo-like correlated state in an open system. *Physical Review Letters*, 88(22):226805, June 2002.

[24] JH DAVIES. Electronic states in narrow semiconducting wires near threshold. *Semiconductor Science and Technology*, 3(10):995–1009, October 1988.

[25] JH DAVIES, IA LARKIN, and EV SUKHORUKOV. Modeling the patterned 2-dimensional electron-gas - electrostatics. *Journal of Applied Physics*, 77(9):4504–4512, May 1995.

[26] JH DAVIES and JA NIXON. Fluctuations in submicrometer semiconducting devices caused by the random positions of dopants. *Physical Review B*, 39(5):3423–3426, February 1989.

[27] Vikram V. Deshpande and Marc Bockrath. The one-dimensional wigner crystal in carbon nanotubes. *Nature Physics*, 4(4):314–318, April 2008.

[28] R DINGLE, HL STORMER, AC GOSSARD, and W WIEGMANN. Electron mobilities in modulation-doped semiconductor heterojunction super-lattices. *Applied Physics Letters*, 33(7):665–667, 1978.

[29] GJ DOLAN. Offset masks for lift-off photoprocessing. *Applied Physics Letters*, 31(5):337–339, 1977.

[30] J. Faist, F. Capasso, D. L. Sivco, C. Sirtori, A. L. Hutchinson, and A. Y. Cho. *Quantum Cascade Laser*, volume 264 of *553-556*. Science, 1994.

[31] GA Fiete and L Balents. Green's function for magnetically incoherent interacting electrons in one dimension. *Physical Review Letters*, 93(22):226401, November 2004.

[32] Gregory A. Fiete. Colloquium: The spin-incoherent luttinger liquid. *Reviews of Modern Physics*, 79(3):801–820, Jul-Sep 2007.

[33] TA FULTON and GJ DOLAN. Observation of single-electron charging effects in small tunnel-junctions. *Physical Review Letters*, 59(1):109–112, JUL 6 1987.

[34] LI GLAZMAN, IM RUZIN, and BI SHKLOVSKII. Quantum transport and pinning of a one-dimensional wigner crystal. *Physical Review B*, 45(15):8454–8463, April 1992.

[35] A. D. Gueclue, C. J. Umrigar, Hong Jiang, and Harold U. Baranger. Localization in an inhomogeneous quantum wire. *Physical Review B*, 80(20):201302, November 2009.

[36] J. Gutierrez, A. Llordes, J. Gazquez, M. Gibert, N. Roma, S. Ricart, A. Pomar, F. Sandiumenge, N. Mestres, T. Puig, and X. Obradors. Strong isotropic flux pinning in solution-derived yba2cu3o7-x nanocomposite superconductor films. *Nature Materials*, 6(5):367–373, May 2007.

[37] EG HAANAPPEL and D VANDERMAREL. Conductance oscillations in two-dimensional sharvin point contacts. *Physical Review B*, 39(8):5484–5487, March 1989.

[38] FDM HALDANE. Luttinger liquid theory of one-dimensional quantum fluids .1. properties of the luttinger model and their extension to the general 1d interacting spinless fermi gas. *Journal of Physics C-Solid State Physics*, 14(19):2585–2609, 1981.

[39] T Haugan, PN Barnes, I Maartense, CB Cobb, EJ Lee, and M Sumption. Island growth of y2bacuo5 nanoparticles in (211(similar to 1.5 nm)/123(similar to 10) (nm))xn composite multilayer structures to enhance flux pinning of yba2cu3o7-delta films. *Journal of Materials Research*, 18(11):2618–2623, November 2003.

[40] T Haugan, PN Barnes, R Wheeler, F Meisenkothen, and M Sumption. Addition of nanoparticle dispersions to enhance flux pinning of the yba2cu3o7-x superconductor. *Nature*, 430(7002):867–870, August 2004.

[41] RJ HAWRYLUK, AM HAWRYLUK, and HI SMITH. Energy dissipation in a thin polymer film by electron-beam scattering. *Journal of Applied Physics*, 45(6):2551–2566, 1974.

[42] RJ HAWRYLUK, HI SMITH, A SOARES, and AM HAWRYLUK. Energy dissipation in a thin polymer film by electron-beam scattering - experiment. *Journal of Applied Physics*, 46(6):2528–2537, 1975.

[43] W. K. Hew, K. J. Thomas, I. Farrer, D. Anderson, D. A. Ritchie, and M. Pepper. Tuning the confinement strength in a split-gate quantum wire. *Physica E-Low-Dimensional Systems & Nanostructures*, 40(5):1645–1647, March 2008.

[44] W. K. Hew, K. J. Thomas, M. Pepper, I. Farrer, D. Anderson, G. A. C. Jones, and D. A. Ritchie. Spin-incoherent transport in quantum wires. *Phys. Rev. Lett.*, 101(3):036801, Jul 2008.

[45] W. K. Hew, K. J. Thomas, M. Pepper, I. Farrer, D. Anderson, G. A. C. Jones, and D. A. Ritchie. Incipient formation of an electron lattice in a weakly confined quantum wire. *Phys. Rev. Lett.*, 102(5):056804, Feb 2009.

[46] Fong-Chi Hsu, Jiu-Yong Luo, Kuo-Wei Yeh, Ta-Kun Chen, Tzu-Wen Huang, Phillip M. Wu, Yong-Chi Lee, Yi-Lin Huang, Yan-Yi Chu, Der-Chung Yan, and Maw-Kuen Wu. Superconductivity in the pbo-type structure alpha-fese. *Proceedings of the National Academy of Sciences of the United States of America*, 105(38):14262–14264, September 2008.

[47] S. Ihnatsenka and I. V. Zozoulenko. Conductance of a quantum point contact based on spin-density-functional theory. *Physical Review B*, 76(4):045338, July 2007.

[48] S. Ihnatsenka and I. V. Zozoulenko. Origin of the "0.25 anomaly" in the nonlinear conductance of a quantum point contact. *Physical Review B*, 79(23):235313, June 2009.

[49] Adilet Imambekov and Leonid I. Glazman. Universal theory of nonlinear luttinger liquids. *Science*, 323(5911):228–231, January 2009.

[50] Sin itiro Tomonaga. *Remarks on Bloch's method of sound waves applied to many-fermion problems*, volume 5 of *544-569*. Progress of Theoretical Physics, 1950.

[51] J. H. Jefferson, A. Ramsak, and T. Rejec. Entanglement and transport anomalies in nanowires. *Journal of Physics-Condensed Matter*, 20(16):164206, April 2008.

[52] Yoichi Kamihara, Takumi Watanabe, Masahiro Hirano, and Hideo Hosono. Iron-based layered superconductor la[o1-xfx]feas (x=0.05-0.12) with t-c=26 k. *Journal of the American Chemical Society*, 130(11):3296, March 2008.

[53] CL KANE and MPA FISHER. Resonant tunneling in an interacting one-dimensional electron-gas. *Physical Review B*, 46(11):7268–7271, September 1992.

[54] CL KANE and MPA FISHER. Transmission through barriers and resonant tunneling in an interacting one-dimensional electron-gas. *Physical Review B*, 46(23):15233–15262, December 1992.

[55] A. D. Klironomos, J. S. Meyer, T. Hikihara, and K. A. Matveev. Spin coupling in zigzag wigner crystals. *Physical Review B*, 76(7):075302, August 2007.

[56] AD Klironomos, JS Meyer, and KA Matveev. Spontaneous spin polarization in quantum wires. *Europhysics Letters*, 74(4):679–685, May 2006.

[57] AD Klironomos, RR Ramazashvili, and KA Matveev. Exchange coupling in a one-dimensional wigner crystal. *Journal De Physique Iv*, 131:233–234, December 2005.

[58] W KOHN and LJ SHAM. Self-consistent equations including exchange and correlation effects. *Physical Review*, 140(4A):1133, 1965.

[59] JM KRANS, JM VANRUITENBEEK, VV FISUN, IK YANSON, and LJ DEJONGH. The signature of conductance quantization in metallic point contacts. *Nature*, 375(6534):767–769, June 1995.

[60] A Kristensen, H Bruus, AE Hansen, JB Jensen, PE Lindelof, CJ Marckmann, J Nygard, CB Sorensen, F Beuscher, A Forchel, and M Michel. Bias and temperature dependence of the 0.7 conductance anomaly in quantum point contacts. *Physical Review B*, 62(16):10950–10957, October 2000.

[61] A Kristensen, JB Jensen, M Zaffalon, CB Sorensen, SM Reimann, PE Lindelof, M Michel, and A Forchel. Conductance quantization above 30 k in gaalas shallow-etched quantum point contacts smoothly joined to the background 2deg. *Journal of Applied Physics*, 83(1):607–609, January 1998.

[62] A Kristensen, PE Lindelof, JB Jensen, M Zaffalon, J Hollingbery, SW Pedersen, J Nygard, H Bruus, SM Reimann, CB Sorensen, M Michel, and A Forchel. Temperature dependence of the "0.7" 2e(2)/h quasi-plateau in strongly confined quantum point contacts. *Physica B*, 251:180–184, June 1998.

[63] R LANDAUER. Spatial variation of currents and fields due to localized scatterers in metallic conduction. *Ibm Journal of Research and Development*, 1(3):223–231, 1957.

[64] IA LARKIN and EV SUKHORUKOV. Method to investigate the random potential in a quantum point-contact. *Physical Review B*, 49(8):5498–5507, February 1994.

[65] RB LAUGHLIN. Anomalous quantum hall-effect - an incompressible quantum fluid with fractionally charged excitations. *Physical Review Letters*, 50(18):1395–1398, 1983.

[66] Patrick A. Lee and Daniel S. Fisher. Anderson localization in two dimensions. *Phys. Rev. Lett.*, 47(12):882–885, 1981.

[67] Alex Levchenko and Alex Kamenev. Coulomb drag in quantum circuits. *Physical Review Letters*, 101(21):216806, November 2008.

[68] E LIEB and D MATTIS. Theory of ferromagnetism and ordering of electronic energy levels. *Physical Review*, 125(1):164, 1962.

[69] W LU, N GU, ZH LU, and Y WEI. An investigation of the backscattering yield of langmuir-blodgett resist films in electron-beam lithography. *Modelling and Simulation In Materials Science and Engineering*, 2(4):913–920, JUL 1994.

[70] JM LUTTINGER. Fermi surface and some simple equilibrium properties of a system of interacting fermions. *Physical Review*, 119(4):1153–1163, 1960.

[71] DL MASLOV and M STONE. Landauer conductance of luttinger liquids with leads. *Physical Review B*, 52(8):R5539–R5542, August 1995.

[72] K. A. Matveev, A. Furusaki, and L. I. Glazman. Asymmetric zero-bias anomaly for strongly interacting electrons in one dimension. *Physical Review Letters*, 98(9):096403, March 2007.

[73] KA Matveev. Conductance of a quantum wire at low electron density. *Physical Review B*, 70(24):245319, December 2004.

[74] KA Matveev. Conductance of a quantum wire in the wigner-crystal regime. *Physical Review Letters*, 92(10):106801, March 2004.

[75] Julia S. Meyer and K. A. Matveev. Wigner crystal physics in quantum wires. *Journal of Physics-Condensed Matter*, 21(2):023203, January 2009.

[76] T MIMURA, K JOSHIN, S HIYAMIZU, K HIKOSAKA, and M ABE. High electron-mobility transistor logic. *Japanese Journal of Applied Physics*, 20(8):L598–L600, 1981.

[77] Yoshikazu Mizuguchi, Fumiaki Tomioka, Shunsuke Tsuda, Takahide Yamaguchi, and Yoshihiko Takano. Superconductivity at 27 k in tetragonal fese under high pressure. *Applied Physics Letters*, 93(15):152505, 2008.

[78] B. H. Mok, S. M. Rao, M. C. Ling, K. J. Wang, C. T. Ke, P. M. Wu, C. L. Chen, F. C. Hsu, T. W. Huang, J. Y. Luo, D. C. Yan, K. W. Ye, T. B. Wu, A. M. Chang, and M. K. Wu. Growth and investigation of crystals of the

new superconductor alpha-fese from kc1 solutions. *Crystal Growth & Design*, 9(7):3260–3264, July 2009.

[79] MJ MONDRY and H KROEMER. Heterojunction bipolar-transistor using a (ga,in)p emitter on a gaas base, grown by molecular-beam epitaxy. *Ieee Electron Device Letters*, 6(4):175–177, 1985.

[80] B. P. Nigam, M. K. Sundaresan, and Ta-You Wu. Theory of multiple scattering: Second born approximation and corrections to molière's work. *Phys. Rev.*, 115(3):491–502, Aug 1959.

[81] JA NIXON and JH DAVIES. Potential fluctuations in heterostructure devices. *Physical Review B*, 41(11):7929–7932, April 1990.

[82] JA NIXON, JH DAVIES, and HU BARANGER. Breakdown of quantized conductance in point contacts calculated using realistic potentials. *Physical Review B*, 43(15):12638–12641, May 1991.

[83] H Ohnishi, Y Kondo, and K Takayanagi. Quantized conductance through individual rows of suspended gold atoms. *Nature*, 395(6704):780–783, October 1998.

[84] L PFEIFFER, KW WEST, HL STORMER, and KW BALDWIN. Electron mobilities exceeding 107 cm2/v s in modulation-doped gaas. *Applied Physics Letters*, 55(18):1888–1890, OCT 30 1989.

[85] VV PONOMARENKO. Renormalization of the one-dimensional conductance in the luttinger-liquid model. *Physical Review B*, 52(12):R8666–R8667, September 1995.

[86] DJ Reilly, TM Buehler, JL O'Brien, AR Hamilton, AS Dzurak, RG Clark, BE Kane, LN Pfeiffer, and KW West. Density-dependent spin polarization in ultra-low-disorder quantum wires. *Physical Review Letters*, 89(24):246801, December 2002.

[87] DJ Reilly, GR Facer, AS Dzurak, BE Kane, RG Clark, PJ Stiles, RG Clark, AR Hamilton, JL O'Brien, NE Lumpkin, LN Pfeiffer, and KW West. Many-body spin-related phenomena in ultra low-disorder quantum wires. *Physical Review B*, 63(12):art. no.–121311, March 2001.

[88] I Safi and HJ Schulz. Transport in an inhomogeneous interacting one-dimensional system. *Physical Review B*, 52(24):17040–17043, December 1995.

[89] S. Sarkozy, F. Sfigakis, K. Das Gupta, I. Farrer, D. A. Ritchie, G. A. C. Jones, and M. Pepper. Zero-bias anomaly in quantum wires. *Physical Review B*, 79(16):161307, April 2009.

[90] HJ SCHULZ. Wigner crystal in one-dimension. *Physical Review Letters*, 71(12):1864–1867, September 1993.

[91] Yu. V. Sharvin. volume 21 of *655*. Sov. Phys. JETP, 1965.

[92] Yu. V. Sharvin and N. I. Bogatina. volume 29 of *419*. Sov. Phys. JETP, 1969.

[93] PW SHOR. Scheme for reducing decoherence in quantum computer memory. *Physical Review a*, 52(4):R2493–R2496, October 1995.

[94] PW Shor. Polynomial-time algorithms for prime factorization and discrete logarithms on a quantum computer. *Siam Review*, 41(2):303–332, June 1999.

[95] Luke Shulenburger, Michele Casula, Gaetano Senatore, and Richard M. Martin. Correlation effects in quasi-one-dimensional quantum wires. *Physical Review B*, 78(16):165303, October 2008.

[96] L. W. Smith, W. K. Hew, K. J. Thomas, M. Pepper, I. Farrer, D. Anderson, G. A. C. Jones, and D. A. Ritchie. Row coupling in an interacting quasi-one-dimensional quantum wire investigated using transport measurements. *Phys. Rev. B*, 80(4):041306, Jul 2009.

[97] HL STORMER. Electron mobilities in modulation-doped gaas-(alga)as heterostructures. *Surface Science*, 132(1-3):519–526, 1983.

[98] A SZAFER and AD STONE. Theory of quantum conduction through a constriction. *Physical Review Letters*, 62(3):300–303, January 1989.

[99] S TARUCHA, T HONDA, and T SAKU. Reduction of quantized conductance at low-temperatures observed in 2 to 10 mu-m-long quantum wires. *Solid State Communications*, 94(6):413–418, May 1995.

[100] J TERSOFF. Theory of semiconductor heterojunctions - the role of quantum dipoles, 1984. Physical Review B.

[101] KJ Thomas, JT Nicholls, NJ Appleyard, MY Simmons, M Pepper, DR Mace, WR Tribe, and DA Ritchie. Interaction effects in a one-dimensional constriction. *Physical Review B*, 58(8):4846–4852, August 1998.

[102] KJ Thomas, JT Nicholls, M Pepper, WR Tribe, MY Simmons, and DA Ritchie. Spin properties of low-density one-dimensional wires. *Physical Review B*, 61(20):13365–13368, May 2000.

[103] KJ Thomas, JT Nicholls, MY Simmons, M Pepper, DR Mace, and DA Ritchie. Possible spin polarization in a one-dimensional electron gas. *Physical Review Letters*, 77(1):135–138, July 1996.

[104] TJ THORNTON, M PEPPER, H AHMED, D ANDREWS, and GJ DAVIES. One-dimensional conduction in the 2d electron-gas of a gaas-algas heterojunction. *Physical Review Letters*, 56(11):1198–1201, March 1986.

[105] DC TSUI, HL STORMER, and AC GOSSARD. Two-dimensional magnetotransport in the extreme quantum limit. *Physical Review Letters*, 48(22):1559–1562, 1982.

[106] D VANDERMAREL and EG HAANAPPEL. Model-calculations of the quantum ballistic transport in two-dimensional constriction-type microstructures. *Physical Review B*, 39(11):7811–7820, April 1989.

[107] H VANHOUTEN, CWJ BEENAKKER, JG WILLIAMSON, MEI BROEKAART, PHM VANLOOSDRECHT, BJ VANWEES, JE MOOIJ, CT FOXON, and JJ HARRIS. Coherent electron focusing with quantum point contacts in a two-dimensional electron-gas. *Physical Review B*, 39(12):8556–8575, April 1989.

[108] H VANHOUTEN, BJ VANWEES, JE MOOIJ, G ROOS, and KF BERGGREN. Magnetic depopulation of subbands and universal conductance fluctuations in quasi-one-dimensional gaas-algaas heterostructures. *Superlattices and Microstructures*, 3(5):497–501, 1987.

[109] BJ VANWEES, LP KOUWENHOVEN, CJPM HARMANS, JG WILLIAMSON, CE TIMMERING, MEI BROEKAART, CT FOXON, and JJ HARRIS. Observation of zero-dimensional states in a one-dimensional electron interferometer. *Physical Review Letters*, 62(21):2523–2526, May 1989.

[110] BJ VANWEES, LP KOUWENHOVEN, H VANHOUTEN, CWJ BEENAKKER, JE MOOIJ, CT FOXON, and JJ HARRIS. Quantized conductance of magnetoelectric subbands in ballistic point contacts. *Physical Review B*, 38(5):3625–3627, August 1988.

[111] BJ VANWEES, LP KOUWENHOVEN, EMM WILLEMS, CJPM HARMANS, JE MOOIJ, H VANHOUTEN, CWJ BEENAKKER, JG WILLIAMSON, and

CT FOXON. Quantum ballistic and adiabatic electron-transport studied with quantum point contacts. *Physical Review B*, 43(15):12431–12453, May 1991.

[112] K VONKLITZING, G DORDA, and M PEPPER. New method for high-accuracy determination of the fine-structure constant based on quantized hall resistance. *Physical Review Letters*, 45(6):494–497, 1980.

[113] F Wakaya, J Takahara, S Takaoka, K Murase, and K Gamo. Confinement potential in an asymmetrically biased quantum point contact. *Japanese Journal of Applied Physics Part 1-Regular Papers Short Notes & Review Papers*, 35(2B):1329–1332, February 1996.

[114] W WALUKIEWICZ, HE RUDA, J LAGOWSKI, and HC GATOS. Electron-mobility in modulation-doped heterostructures. *Physical Review B*, 30(8):4571–4582, 1984.

[115] CK Wang and KF Berggren. Spontaneous spin polarization in quantum wires. *Physica E*, 2(1-4):964–968, July 1998.

[116] M. J. Wang, J. Y. Luo, T. W. Huang, H. H. Chang, T. K. Chen, F. C. Hsu, C. T. Wu, P. M. Wu, A. M. Chang, and M. K. Wu. Crystal orientation and thickness dependence of the superconducting transition temperature of tetragonal fese1-x thin films. *Physical Review Letters*, 103(11):117002, September 2009.

[117] JF WEISZ and KF BERGGREN. Characterization of narrow quantum channels using model potentials. *Physical Review B*, 40(2):1325–1327, July 1989.

[118] DA WHARAM, TJ THORNTON, R NEWBURY, M PEPPER, H AHMED, JEF FROST, DG HASKO, DC PEACOCK, DA RITCHIE, and GAC JONES. One-dimensional transport and the quantization of the ballistic resistance. *Journal of Physics C-Solid State Physics*, 21(8):L209–L214, March 1988.

[119] E Wigner. On the interaction of electrons in metals. *Physical Review*, 46(11):1002–1011, December 1934.

[120] JG WILLIAMSON, CE TIMMERING, CJPM HARMANS, JJ HARRIS, and CT FOXON. Quantum point contact as a local probe of the electrostatic potential contours. *Physical Review B*, 42(12):7675–7678, October 1990.

[121] M. K. Wu, F. C. Hsu, K. W. Yeh, T. W. Huang, J. Y. Luo, M. J. Wang, H. H. Chang, T. K. Chen, S. M. Rao, B. H. Mok, C. L. Chen, Y. L. Huang, C. T. Ke, P. M. Wu, A. M. Chang, C. T. Wu, and T. P. Perng. The development

of the superconducting pbo-type beta-fese and related compounds. *Physica C-Superconductivity and Its Applications*, 469(9-12):340–349, May-Jun 2009.

[122] A Yacoby, HL Stormer, NS Wingreen, LN Pfeiffer, KW Baldwin, and KW West. Nonuniversal conductance quantization in quantum wires. *Physical Review Letters*, 77(22):4612–4615, November 1996.

[123] Kuo-Wei Yeh, Tzu-Wen Huang, Yi-Lin Huang, Ta-Kun Chen, Fong-Chi Hsu, Phillip M. Wu, Yong-Chi Lee, Yan-Yi Chu, Chi-Lian Chen, Jiu-Yong Luo, Der-Chung Yan, and Maw-Kuen Wu. Tellurium substitution effect on superconductivity of the alpha-phase iron selenide. *Epl*, 84(3):37002, November 2008.

[124] HZ ZHENG, HP WEI, DC TSUI, and G WEIMANN. Gate-controlled transport in narrow gaas/alxga1-xas heterostructures. *Physical Review B*, 34(8):5635–5638, October 1986.

[125] Ren Zhi-An, Lu Wei, Yang Jie, Yi Wei, Shen Xiao-Li, Zheng-Cai, Che Guang-Can, Dong Xiao-Li, Sun Li-Ling, Zhou Fang, and Zhao Zhong-Xian. Superconductivity at 55 k in iron-based f-doped layered quaternary compound sm[o1-xfx]feas. *Chinese Physics Letters*, 25(6):2215, 2008.

[126] SL Zhu, ZD Wang, and L Hu. Conductance of a quantum point contact in the presence of spin-orbit interaction. *Journal of Applied Physics*, 91(10):6545–6552, May 2002.

Biography

Phillip M Wu

Born April 29, 1980 in Houston, Texas, USA.

Ph.D., Department of Physics, Duke University 2009

B.A., Physics, Columbia University 2002

I joined the Physics department at Duke in 2003 as a graduate assistant in the Low Temperature Transport group of Prof. Albert Chang. Prior to this, I worked for one year at the Institute of Physics, Academia Sinica. I also took on a part time job teaching high school AP level physics for one year at National Experimental High School (NEHS) in Taiwan. I received my BA in Physics from Columbia University in 2002.

Publications

1. H.H. Chang, J.Y. Luo, C.T. Wu, F.C. Hsu, T.K. Chen, P.M. Wu, M.K. Wu, M.J. Wang. *Te substitution effect on electronic properties of β-FeSe thin films.* Physica C. In Press (2009)
2. M.J. Wang, J.Y. Luo, T.W. Huang, H.H. Chang, T.K. Chen, F.C. Hsu, C.T. Wu, P.M. Wu, A.M. Chang, M.K. Wu. *Crystal orientation and thickness dependence of superconductivity on tetragonal $FeSe_{1-x}$ thin films.* Phys. Rev. Lett. 103, 117002 (2009).
3. K. W. Yeh, C. T. Ke, T. W. Huang, T. K. Chen, Y. L. Huang, P. M. Wu and M. K. Wu. *Superconducting $FeSe_{1-x}Te_x$ Single Crystals Grown by Optical Zone-Melting Technique.* Cryst. Growth Des. 9(11), 4847-4851 (2009).
4. Andrew K. Stemshorn, Yogesh K. Vohra, Phillip M. Wu, F.C. Hsu, Y.L. Huang, M.K. Wu and K.W. Yeh. *Pressure-induced reversible amorphization in superconducting compound $FeSe_{0.5}Te_{0.5}$.* High Pressure Research 29, 267-271 (2009).

5. M.K. Wu, F.C. Hsu, K.W. Yeh, T.W. Huang, J.Y. Luo, M.J. Wang, H.H. Chang, T.K. Chen, S.M. Rao, B.H. Mok, C.L. Chen, Y.L. Huang, C.T. Ke, P.M. Wu, A.M. Chang, C.T. Wu and T.P. Perng. *The development of the superconducting PbO-type beta-FeSe and related compounds.* Physica C 469, 340-349 (2009).
6. B. H. Mok, S. M. Rao, M. C. Ling, K. J. Wang, C. T. Ke, P. M. Wu, C. L. Chen, F. C. Hsu, T. W. Huang, J. Y. Luo, D. C. Yan, K. W. Yeh, T. B. Wu, A. M. Chang and M. K. Wu. *Growth and Investigation of Crystals of the New Superconductor α-FeSe from KCl Solutions.* Cryst. Growth Des. 9(7), 32603264 (2009).
7. Georgiy Tsoi, Andrew K. Stemshorn, Yogesh K. Vohra, Phillip M Wu, F. C. Hsu, Y.L. Huang, M.K. Wu, K.W. Yeh, and Samuel T. Weir. *High pressure superconductivity in iron-based layered compounds studied using designer diamonds.* J. Phys.: Condens. Matter 21, 232201 (2009).
8. K. W. Yeh, H. C. Hsu, T. W. Huang, P. M. Wu, Y. L. Huang, T. K. Chen, J. Y. Luo, and M. K. Wu. *Se and Te Doping Study of the FeSe Superconductors.* J. Phys. Soc. Jpn. 77SC, 19-22 (2008).
9. Kuo-Wei Yeh, Tzu-Wen Huang, Yi-lin Huang, Ta-Kun Chen, Fong-Chi Hsu, Phillip M. Wu, Yong-Chi Lee, Yan-Yi Chu, Chi-Lian Chen, Jiu-Yong Luo, Der-Chung Yan and Maw-Kuen Wu. *Tellurium substitution effect on superconductivity of the α-phase iron selenide.* Europhysics Lett. 84, 37002 (2008).
10. Fong-Chi Hsu, Jiu-Yong Luo, Kuo-Wei Yeh, Ta-Kun Chen, Tzu-Wen Huang, Phillip M. Wu, Yong-Chi Lee, Yi-Lin Huang, Yan-Yi Chu, Der-Chung Yan, and Maw-Kuen Wu. *Superconductivity in the PbO-type structure α-FeSe.* Proc. Natl. Acad. Sci. 105, 14262-14264 (2008).
11. Z.L. Fang, P. Wu, N. Kundtz, A.M. Chang, X.Y. Liu, J.K. Furdyna. *Spin dependent resonant tunneling through 6 micron diameter double barrier resonant tunneling diode.* Appl. Phys. Lett. 91, 022101 (2007).
12. Ku Bui Ma, P.M. Wu, Y. Postrekhin, H. Ye, T. Johansen, Wei-Kan Chu. *Drag torque on slowly rotating high temperature superconductor in non-axisymmetric magnetic field.* Magnetics, IEEE Transactions, Volume: 37 Issue: 4 Part: 1, July, 2874-2876 (2001).

Presentations

- Seminar. *Tunable Conductance Anomalies in Asymmetric Quantum Point Contacts.* Institute of Physics, Lund University, Lund, Sweden, April 12, 2010.
- Presentation. *Tunable Conductance Anomaly in Asymmetrically Gated Quantum Point Contacts.* APS March Meeting, Portland, Oregon, 2010.
- Physics Student Seminar. *Semiconductor Quantum Dots.* Dept. of Physics, Duke University, Durham, NC, July 8, 2005.

- Invited Speaker. *Taiwan and I.* Inaugural Taiwan Tech Trek, 2005.

Honors

- Fritz London Graduate Fellowship. Dept. of Physics, Duke University, 2009.